Doklady Physics, Vol. 48, No. 6, 2003, pp. 261–263. Translated from Doklady Akademii Nauk, Vol. 390, No. 4, 2003, pp. 465–467.

PHYSICS

Simulation of a Significant Increase in the Transconductance of MOS Transistors Due to Sectioning of the Channel

V. A. Gergel', Academician Yu. V. Gulyaev, A. P. Zelenyĭ, and M. N. Yakupov

Received January 31, 2003

In study [1], we showed that the transconductance and speed of field-effect transistors could be significantly increased by sectioning the channel with low-resistance local inclusions providing an efficient "cooling" of electrons and a corresponding increase in mobility and drift velocity. In qualitative estimates presented in [1] for advantages of the proposed structural modification of the transistor channel, we described the electron drift in the quasihydrodynamic (thermal) model [2], which was simplified by neglecting the thermal relaxation and the thermoelectric current but, nevertheless, revealed the primary features of the so-called overshoot effect [3].

In [1], we assumed that the mean electric field was constant and analyzed only the desired maximum-to-minimum electric-field ratio sufficient for an efficient cooling of carriers in the low-resistance inclusions. However, as is known [4], the electric field in the MOS-transistor channel in the near-saturation regimes is substantially inhomogeneous and increases from the source to the drain. The mean electric field must be similarly inhomogeneous in the proposed structure sectioned by low-resistance inclusions.

The purpose of this study is to develop a mathematical model, which includes the indicated spatial inhomogeneity in the mean field, for adequate calculation of the current–voltage (*I–V*) characteristics of the transistor. In addition, in order to illustrate the advantages of the proposed sectioned structure including an increase in the mean velocity of carriers in the transistor channel and its high transconductance, we carry out corresponding test calculations of *I–V* characteristics.

Figure 1 shows the hypothetical transistor structure under consideration, whose channel is divided into n sections by specific low-resistance regions obtained by the corresponding local doping. The level of local doping and, correspondingly, the conductivity in these regions are assumed to be so high that a voltage drop across these regions is negligible and electrons leaving them can be considered as completely cooled (down to the equilibrium temperature). In this case, using the classical concept of drift [4]

$$IL = C\int_0^{V_D} \mu(V_G - \varphi)d\varphi \qquad (1)$$

and the ultra-quasihydrodynamic dependence [2] of mobility on potential

$$\mu \equiv \mu(\varphi) = \frac{\mu_0}{\sqrt{1 + \dfrac{\varphi}{\varphi_0}}}, \qquad (2)$$

where $\varphi_0 = \dfrac{5}{2}T_0 \approx 0.065$ V in the simplest case, we can write the relation

$$\frac{Il_i}{\mu_0 C_0} = \sqrt{\varphi_0}\int_{V_{i-1}}^{V_i} \frac{V_G - \varphi}{\sqrt{\varphi_0 + \varphi - V_{i-1}}}d\varphi \qquad (3)$$

for any high-resistance section of the channel. Here, I is the current density per unit channel width; C_0 and μ_0 are

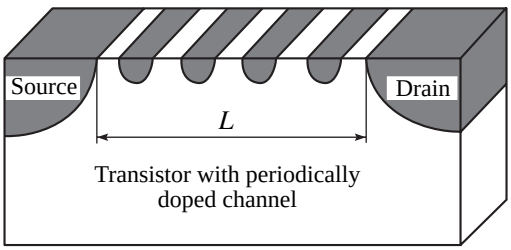

Fig. 1. Schematic representation of the subgate region of the sectioned-channel MOS transistor.

Institute of Radio Engineering and Electronics, Russian Academy of Sciences, ul. Mokhovaya 18, Moscow, 103907 Russia

1028-3358/03/4806-0261$24.00

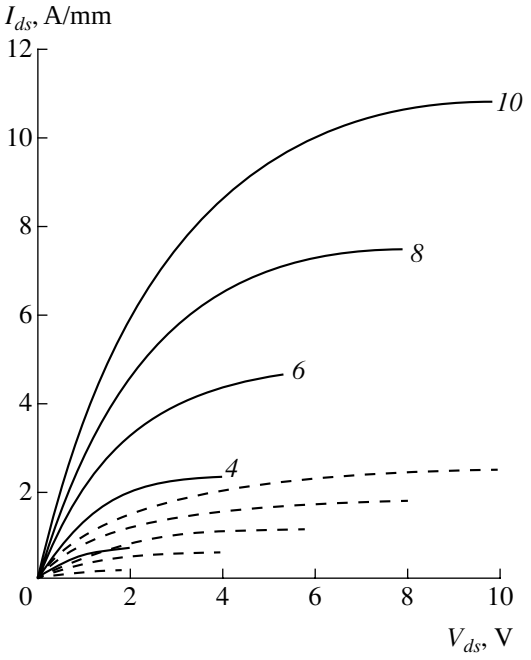

Fig. 2. Current–voltage characteristics of the (solid lines) sectioned and (dashed lines) ordinary transistors. Numbers near the curves are the gate voltage V_G = (2.4–10) V.

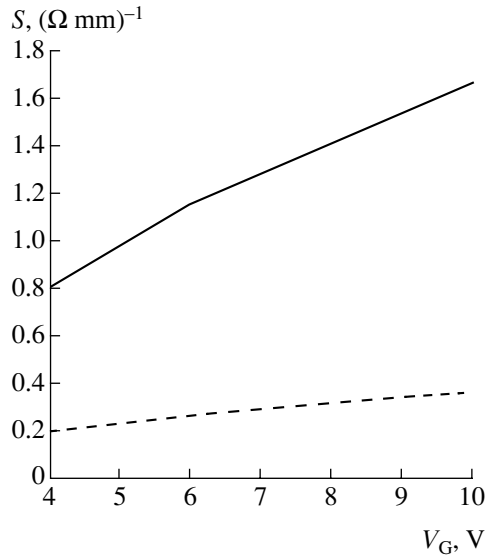

Fig. 3. Highest transconductance $\frac{\partial I}{\partial V_G}$ vs. the gate voltage V_G.

the specific oxide capacitance and the original (low-field) mobility, respectively; V_G is the gate voltage measured from the threshold voltage; l_i is the length of the ith high-resistance section; and V_{i-1} and V_i are the potentials at its boundaries, $i = \{1, 2, \ldots, n\}$. A solution of this set of n equations must satisfy the following two boundary conditions: (i) $V_0 = 0$; i.e., the potential at the beginning of the first section is equal to the source potential, and (ii) $V_n = V_D$; i.e., the drain potential is equal to the potential at the end of the last section.

We developed a simple algorithm for the step-by-step solution of set (3). Namely, for a certain current I, we find V_1 by numerical integration of the first (i = 1) equation. This value appears as a parameter in the second equation, whose solution gives us V_2 and so on until $V_n = V_D$. Similar calculations for the corresponding sequence of currents provide the desired I–V characteristic.

The corresponding test calculation was performed for the typical transistor structure with a channel length of L = 0.95 μm divided into ten high-resistance sections each l_i = 50 nm in length by nine low-resistance inclusions of the same size. We chose a specific capacitance of 3.5×10^{-7} F cm^{-2}, which corresponds to a 10-nm-thick oxide, and an original mobility of μ_0 = 700 cm^2 (V s)$^{-1}$, which is typical for the electron inversion layer in Si (this μ_0 value corresponds to φ_0 = 0.2 V).

For these parameters, Eq. (3) transforms to

$$I \approx 5 \int_{V_{i-1}}^{V_i} \frac{V_G - \varphi}{\sqrt{1 + \dfrac{\varphi - V_{i-1}}{0.2}}} d\varphi, \qquad (4)$$

where $i = \{1, 2, \ldots, n\}$, I is measured in amperes per millimeter, and the voltage and potential are measured in volts.

The numerical solution of set (4) for the characteristic gate voltages V_G = (2–10) V is shown in Fig. 2. For comparison, the dashed lines in Fig. 2 display the characteristics calculated by the equation

$$I \approx \frac{5}{19} \int_{V_0}^{V_D} \frac{V_G - \varphi}{\sqrt{1 + \dfrac{\varphi}{0.2}}} d\varphi \qquad (5)$$

for a standard MOS transistor with a homogeneous channel of the same (0.95 μm) length.

It is seen that currents in the sectioned-channel transistor considerably exceed currents in the ordinary structure. Figure 3 shows the device transconductance $S = \frac{\partial}{\partial V_G} I$ ($V_D = V_G$). As is seen, S for the sectioned-channel structure is much higher than the transconductance of the ordinary device with the homogeneous channel.

Higher transconductance naturally implies higher speed. In our opinion, the above results obviously and conclusively demonstrate the expected advantages of the proposed technological solution. We think that these results will stimulate the search for particular technological solutions for the practical realization of this highly promising idea.

ACKNOWLEDGMENTS

This work was supported by the Russian Foundation for Basic Research, project no. 01-02-16360.

REFERENCES

1. V. A. Gergel' and V. G. Mokerov, Dokl. Akad. Nauk **375**, 609 (2000) [Dokl. Phys. **45**, 647 (2000)].
2. V. A. Gergel', V. G. Mokerov, M. V. Timofeev, and Yu. V. Fedorov, Fiz. Tekh. Poluprovodn. (St. Petersburg) **34**, 239 (2000) [Semiconductors **34**, 233 (2000)].
3. T. Enoki, S. Sugitani, and Y. Yamane, IEEE Trans. Electron Devices **37**, 935 (1990).
4. S. M. Sze, *Physics of Semiconductor Devices* (Wiley, New York, 1981; Mir, Moscow, 1984), Vol. 2.

Translated by V. Bukhanov

Doklady Physics, Vol. 48, No. 6, 2003, pp. 264–268. Translated from Doklady Akademii Nauk, Vol. 390, No. 5, 2003, pp. 605–609.

PHYSICS

Anomalous Diffusion with Time- and Coordinate-Dependent Memory

Ya. L. Kobelev*, L. Ya. Kobelev, and Yu. L. Klimontovich†*****

Presented by Academician V.P. Skripov September 11, 2002

Received December 26, 2002

INTRODUCTION

Anomalous diffusion, i.e., diffusion for which the mean squared displacement of a particle is proportional to a fractional power of time ($q\langle x\rangle q \sim t^{\beta}$, where β is a fractional number), has been actively studied in recent years. It is observed in aerosols, gels, spin glasses, certain unordered systems, aperiodic crystals, electron–ion plasma, in systems described by the statistical physics of open systems [1], etc. Anomalous diffusion (or fractal relaxation) was described theoretically by using fractal geometry [2] in numerous works (see review [3]). The authors of these works used equations with fractional derivatives in time [4], coordinates [5] (see also equations with distributed fractional order [6]), or in time and coordinate simultaneously [7]. In this case, one-coordinate-dimensional anomalous diffusion in the absence of external forces is described by the equation [7]

$$\frac{\partial^{\alpha}}{\partial t^{\alpha}} n(x, t) = D_0 \frac{\partial^{2\gamma}}{\partial x^{2\gamma}} n(x, t), \quad 0 \le \alpha < 1, \quad 0 \le \gamma < 1. \tag{1}$$

Here, Riemann–Liouville left fractional derivatives [8, 9] are used and

$$\frac{\partial^{\alpha}}{\partial t^{\alpha}} n(x, t) \equiv_{+} D^{\alpha}_{0, t} n(x, t) = \frac{1}{\Gamma(1-\alpha)} \frac{d}{dt} \int_0^t \frac{n(\tau, x) d\tau}{(t-\tau)^{\alpha}},$$
$$\frac{\partial^{\gamma}}{\partial x^{\gamma}} n(x, t) \equiv_{+} D^{\alpha}_{0, x} n(x, t) = \frac{1}{\Gamma(1-\gamma)} \frac{d}{dx} \int_0^x \frac{n(t, x_1) dx_1}{(x-x_1)^{\gamma}}. \tag{2}$$

† Deceased.

* *Institute of Metal Physics, Ural Division, Russian Academy of Sciences, ul. S. Kovalevskoĭ 18, Yekaterinburg, 620219 Russia*
e-mail: yakov@imp.uran.ru
** *Ural State University, pr. Lenina 51, Yekaterinburg, 620083 Russia*
e-mail: leonid.kobelev@usu.ru
*** *Moscow State University, Vorob'evy gory, Moscow, 119899 Russia*

Equation (1) and its exact solution were analyzed in [7], where the fractional number α associated with the fractal dimension of the space where diffusion occurs was supposed to be constant. Equations with fractional derivatives describe non-Markov processes with constant memory. In particular, certain gels and aerosols, spin glasses, viscoelastic glasses and polymers, electron–ion plasma, aperiodic crystals, turbulence, economic systems, certain nonlinear-dynamic systems, etc., are among systems with memory. However, memory (both temporal memory and memory about trajectories passed by a system) in some physical systems can vary in time and coordinates. Available experimental data indicate that the fractal dimension of physical objects depends on the parameters of the environment (temperature, pressure, etc.) and internal characteristics of the system (elasticity, strength, etc.). In particular, the dependence of the fractal dimension of a growing polycrystalline film on its growth time was determined in [10], the dependence of the fractal dimension for zirconium oxide on the external shock pressure was found in [11], and numerous examples of the fractal properties of materials were given in [12]. Diffusion processes are important for all listed examples (and many other systems). Therefore, it is of interest to analyze, as a first step, diffusion in a model fractal medium, where fractal dimension depends slightly on time and coordinates. Such a model can be used to describe diffusion in numerous applications (in particular, diffusion in a growing polycrystal in a medium with oscillating temperature, diffusion over the surface of a solid with fractal dimension varying from one its region to another, etc.). In addition, this model attracts independent attention (a number of interesting problems of heat transfer are beyond the scope of this study). Dynamic processes in systems with time- and coordinate-dependent memory cannot be described in terms of Riemann–Liouville fractional derivatives (2) that do not reproduce variations in memory. For this reason, it is necessary to develop a new mathematical technique generalizing fractional derivatives and Riemann–Liouville integrals for the dynamics of multifractal objects (i.e., objects whose fractal dimension

1028-3358/03/4806-0264$24.00

depends on time and coordinates). One of us (L.Ya.K.) introduced such a technique in [13–15].

GENERALIZED FRACTIONAL DERIVATIVES AND RIEMANN–LIOUVILLE INTEGRALS

To describe diffusion in a medium with coordinate- and time-dependent multifractal dimension (or in a physical system with such fractal properties), one must use Riemann–Liouville fractional derivatives that were introduced in [13] and used in a number of works (see, e.g., [14]). These derivatives are defined as (for left derivatives; for more detail, see [13])

$$\frac{\partial^{1+\varepsilon_t}}{\partial t^{1+\varepsilon_t}} f \equiv D_{+,t}^{d_t} f$$

$$= \left(\frac{d}{dt}\right)^n \int_a^t dt' \frac{f(t')}{\Gamma(n-d_t(t'))(t-t')^{d_t(t')-n+1}}, \qquad (3)$$

$$\frac{\partial^{1+\varepsilon_x}}{\partial x^{1+\varepsilon_t}} f \equiv D_{+,x}^{d_x} f$$

$$= (-1)^n \left(\frac{d}{dx}\right)^n \int_a^x dx' \frac{f(x')}{\Gamma(n-d_x(x'))(x-x')^{d_x(x')-n+1}}.$$

Here, Γ is the Euler gamma function; $n = \{d\} + 1$, where $\{d\}$ is the integer part of d for $d \geq 0$ (i.e., $(n-1) \leq d < n$) and $n = 0$ for $d < n$; $d_t = 1 + \varepsilon(t)$; and $d_x = 1 + \varepsilon(x)$. The integral operators defined above for fractional exponents d_t and d_x depending on coordinates and time can be expressed in terms of ordinary derivatives and integrals [13] for $|\varepsilon| \ll 1$. In this case, generalized Riemann–Liouville fractional derivatives satisfy the approximate relations (we present here only relations for derivatives)

$$D^{1+\varepsilon_t} n(x,t) = (1+\varepsilon_t)\frac{\partial}{\partial t} n(x,t) + \frac{\partial \varepsilon_t}{\partial t} n(x,t),$$
$$D^{1+\varepsilon_x} n(x,t) = (1+\varepsilon_x)\frac{\partial}{\partial x} n(x,t) + \frac{\partial \varepsilon_x}{\partial x} n(x,t). \qquad (4)$$

These relations make it possible to describe the dynamics of a system including the effect of changes in the fractal dimension (if they are much smaller than unity) on the behavior of the physical system by means of ordinary differential and integral equations. To determine the fractal dimension d_α, the equations corresponding to the problems under consideration were obtained in [13].

ANOMALOUS-DIFFUSION EQUATION

The equation for anomalous diffusion in a medium with varying fractal dimensions $d_t(t, x)$ and $d_x(t, x)$ has the form (in the absence of external forces)

$$D_{+,t}^{d_t(t,x)} n(x,t) \equiv \frac{\partial^{1+\varepsilon_t(t,x)}}{\partial t^{1+\varepsilon_t(t,x)}} n(x,t)$$
$$= \frac{\partial^{(1+\varepsilon_x(t,x))}}{\partial x^{(1+\varepsilon_x(t,x))}} \left[D_{x,t} \frac{\partial^{(1+\varepsilon_x(t,x))}}{\partial x^{(1+\varepsilon_x(t,x))}} n(x,t) \right]. \qquad (5)$$

When the diffusion coefficient is constant [$D(x, t) = D_0$], it can be separated from the fractional derivative similarly to the case of constant fractal dimension. In contrast to equations describing constant-memory anomalous diffusion, which was recently studied in detail, Eq. (5) includes slow variations in memory both in time and in coordinates. Since weak memory and its variations occur near normal diffusion, Eq. (5) describes almost normal diffusion characterizing by weak varying memory in contrast to normal diffusion. Only the $|\varepsilon| \ll 1$ case, which corresponds to weak memory, will be analyzed below for this equation. The equation for anomalous diffusion with constant fractal dimension $\alpha \neq 1$, $\gamma \neq 1$, and slightly varying memory has the form

$$\frac{\partial^{\alpha+\varepsilon_t(t,x)}}{\partial t^{\alpha+\varepsilon_t(t,x)}} n(x,t) = D_0 \frac{\partial^{(\gamma+\varepsilon_x(t,x))}}{\partial^{(\gamma+\varepsilon_x(t,x))}} \left[\frac{\partial^{(\gamma+\varepsilon_x(t,x))}}{\partial^{(\gamma+\varepsilon_x(t,x))}} n(x,t) \right].$$

The equation for diffusion with $\alpha \neq 1$, $\gamma \neq 1$, and weak memory is not analyzed in this work. There are considerable mathematical difficulties in its solution even for the $\varepsilon \ll 1$ case. However, its solutions can be found in the analytical form by means of Fox functions for particular cases.

WEAK-MEMORY APPROXIMATION

Using relations (4) and the approximate expression for Eq. (5), generalized fractional derivatives (3) for $|\varepsilon| \ll 1$ can be expressed in terms of ordinary derivatives as

$$(1+\varepsilon_t)\frac{\partial n}{\partial t} + \frac{\partial \varepsilon}{\partial t} n$$
$$= D_0 \left[(1+2\varepsilon_x)\frac{\partial^2 n}{\partial x^2} + 3\frac{\partial \varepsilon}{\partial x}\frac{\partial n}{\partial x} + \frac{\partial^2 \varepsilon}{\partial x^2} n(x,t) \right], \qquad (6)$$

where ε^2 terms are omitted. Since fractal additions to unity are small, the right- and left-hand sides of Eq. (6)

can be divided by $1 + \varepsilon_x$. In this case, we obtain

$$\frac{\partial n}{\partial t} = D(x,t)\frac{\partial^2 n}{\partial x^2} + 3D_0\frac{\partial \varepsilon_x}{\partial x}\frac{\partial n}{\partial x} + \left(D_0\frac{\partial^2 \varepsilon_x}{\partial x^2} - \frac{\partial \varepsilon_t}{\partial t}\right)n, \quad (7)$$

$$D(x,t) = D_0(1 + 2\varepsilon_x - \varepsilon_t).$$

Let us represent Eq. (7) in the following form corresponding to the description of diffusion in hydrodynamic systems:

$$\frac{\partial n}{\partial t} = \frac{\partial}{\partial x}\left[D(x,t)\frac{\partial}{\partial x}n - Fn\right] + An, \quad (8)$$

where

$$F(x) = -D_0\left(\frac{\partial \varepsilon_x}{\partial x} + \frac{\partial \varepsilon_t}{\partial x}\right), \quad A = -\left(D_0\frac{\partial^2 \varepsilon_t}{\partial^2 x} + \frac{\partial \varepsilon_t}{\partial t}\right). \quad (9)$$

Equation (8) differs from Eq. (1) in three properties. First, the diffusion coefficient depends on time and coordinates due to the effect of a fractal medium with memory depending on time and coordinates. Second, the "force"

$$F = -D_0\left(\frac{\partial \varepsilon_x}{\partial x} + \frac{\partial \varepsilon_t}{\partial x}\right)$$

appears due to the coordinate dependence of fractal dimensions (such forces were first considered in [13–15]). Third, there is a derivative-free term that depends only on the fractal time dimension, is proportional to n, and characterizes, depending on the coefficient sign, the retardation or enhancement of diffusion. Therefore, even weak memory, which is taken into account by generalized Riemann–Liouville fractional derivatives and presents the characteristics of a fractal medium, transforms constant-coefficient diffusion to varying-coefficient diffusion. Moreover, this memory is responsible for a force with which the fractional medium acts on a diffusing particle. This force appears only if the diffusing particle has memory depending on coordinates; i.e., it "remembers" its trajectories.

Those terms in Eq. (8) that involve fractional additions (F and A) to the time and space dimensions are small. Therefore, this equation can be solved approximately by changing the function n to n_0, which satisfies Eq. (1), in terms involving ε (or in some of these terms). In particular, if such a change is made only in the term involving A, we arrive at the following equation of diffusion in the external field $F(x)$ induced by the fractal structure of the medium with the source An_0:

$$\frac{\partial n}{\partial t} - \frac{\partial}{\partial x}\left[D(x,t)\frac{\partial}{\partial x}n - Fn\right] = A(x,t)n_0. \quad (10)$$

The external force leads, depending on its sign, either to retardation or to enhancement of particle diffusion. Owing to the term involving $A(x, t)$, the energy of the diffusing particle decreases depending both on time and coordinates [due to $\varepsilon_t(t, \mathbf{r})$ dependence]. The roughest approximation for Eq. (10) has the form

$$\frac{\partial n}{\partial t} - D_0\frac{\partial^2 n}{\partial x^2} = \frac{\partial}{\partial x}\left[(D(x,t) - D_0)\frac{\partial}{\partial x}n_0 - Fn_0\right] + A(x,t)n_0 = B(x,t,n_0), \quad (11)$$

where the exact value n in all terms involving ε_t and ε_x is replaced by the approximate value n_0 satisfying Eq. (1) with $\alpha = \gamma = 1$. In this case, the diffusion equation involves a more complex source $B(x, t, n_0)$, and small fractal corrections to dimensions provide corrections to the Gaussian distribution.

EXAMPLE OF ANOMALOUS DIFFUSION IN A MEDIUM WITH A PERIODIC DEPENDENCE OF MEMORY ON TIME AND COORDINATES

As an example, let us consider the diffusion equation in a model medium, where

$$\varepsilon_t = \alpha_{0t}\cos\omega_t t, \quad \varepsilon_x = \alpha_{0x}\cos\omega_x t. \quad (12)$$

Here, ω_t and ω_x are frequencies characterizing variation in fractal dimensions d_t and d_x. Such a medium corresponds, e.g., to the growth of a polycrystalline film with surface irregularities described by clusters with coordinate-dependent fractal dimension in a varying temperature mode (i.e., the Lagrangian density of clusters depends on time). In this case, if α_t and α_x are small, fractal dimension can be represented in the form (when α_t and α_x depend only on time and coordinates, respectively)

$$\alpha_t = d_t = 1 + \varepsilon_t(t), \quad \varepsilon_t(t) = \varepsilon_{0t}\sin\omega_t t, \quad |\varepsilon_t| \ll 1;$$
$$\gamma_x = d_x = 1 + \varepsilon_x(x), \quad \varepsilon_x(x) = \varepsilon_{0x}\sin\omega_x x, \quad |\varepsilon_x| \ll 1.$$

Since ε_t and ε_x are small, a solution of Eq. (11) can be sought in the form $n = n_0 + n_1$, where n_0 is the solution of diffusion equation (1) with $\alpha = \gamma = 1$ and $n_1 \ll n_0$ is proportional to ε_t or ε_x. Then,

$$n_0 = \frac{\exp\dfrac{-x^2}{D_0 t}}{\sqrt{D_0 t}}, \quad (13)$$

$$n_1 = \int dp\,dp^0 \exp^{-ip^0 t + ipx} B(p, p^0), \quad (14)$$

$$B(p, p^0) = \int \exp^{-ipx + ip^0 t} B(x, t, n_0(x))\,dx\,dt. \quad (15)$$

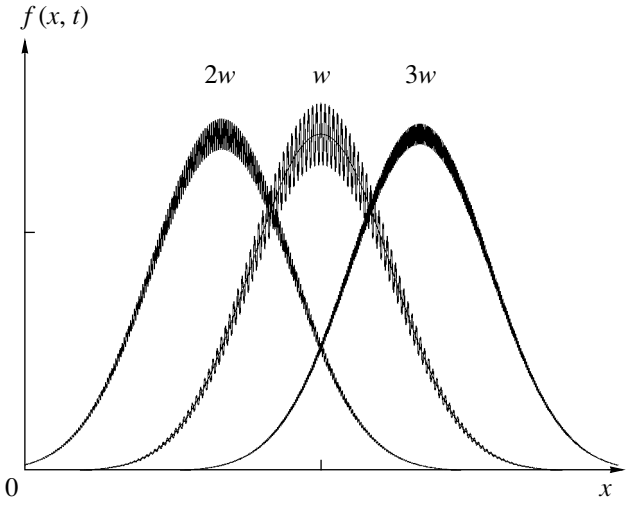

Fig. 1. Qualitative pattern of a Gaussian distribution including corrections to weak varying memory approximated by a periodic function of coordinates and time at time t. For convenience, plots are shifted with respect to each other.

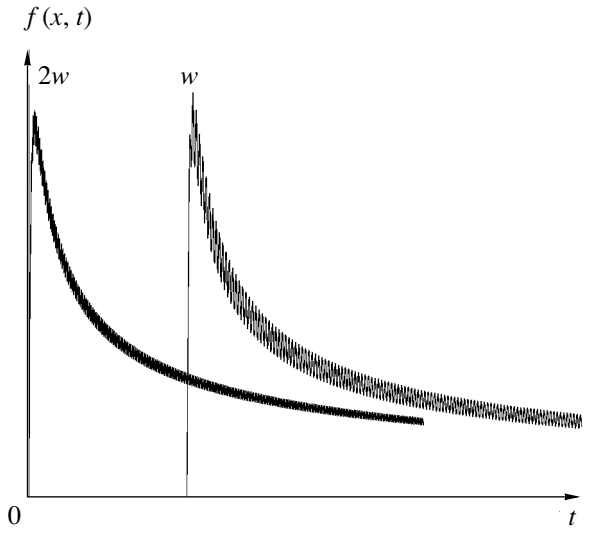

Fig. 2. Same as in Fig. 1, but at the point x.

Solution (14) includes terms that involve ε_t and ε_x and depend periodically on ω_t and ω_x. Figures 1 and 2 show qualitative plots illustrating the weak-memory effect depending periodically on time and coordinates on the Gaussian distribution describing diffusion in the non-Markov fractal medium for various ω_t, ω_x, ε_t, and ε_x values. As frequencies ω_t and ω_x increase, individual maxima and minima in the figures superpose, looking like flicker noise. We emphasize that slightly time- and coordinate-dependent memory for fractal media with $d = d_0 + \varepsilon(t)$ for $d_0 \neq 1$ does not lead to new qualitative effects occurring for $d_0 = 1$ (excluding the appearance of Levy distributions instead of Gaussian distributions, which also appear in constant-memory systems). As follows from the equations determining the fractal dimensions, which are not considered here, when the Lagrangian density is proportional to expression (12), ε_{0t} and ε_{0x} are proportional to ω_t^{-1} and ω_x^{-1}, respectively.

CONCLUSIONS

The basic differences of anomalous diffusion in a fractal medium with weak memory depending on time and coordinate from normal diffusion are as follows.

(i) Appearance of an analogue of an external force caused by coordinate-dependent memory. The appearance of this force, which was found for the first time, can be responsible for observable effects (e.g., additional motion of magnetic domain walls, change in the electric parameters of solid electrolytes, motion of ions in biological structures, etc.). Since fractal structures are widespread in biological objects, which are often described in statistical physics, the inclusion of forces of new (multifractal) origin is of considerable interest.

(ii) Appearance of a shift of the Gaussian-distribution maximum.

(iii) Time- and coordinate-dependent changes in wings and maxima of the Gaussian distribution [or Levy distributions for $d_0 = \alpha \neq 1 + \varepsilon(t, x)$ or $d_0 = \gamma \neq 1 + \varepsilon(t, x)$].

(iv) The example analyzed above shows that weak memory depending periodically on time or coordinates for high frequencies ω_t and ω_x is an imitation of external noise (including flicker noise) that arises as an addition to ordinary noise, particularly in the cases where frequencies ω_t and ω_x are incommensurable.

ACKNOWLEDGMENTS

This work was supported in part by INTAS (grant no. 00-0847), the Russian Foundation for Basic Research (project no. 00-02-16285), and the US Civilian Research and Development Foundation for the Independent States of the Former Soviet Union (grant no. REC-005).

REFERENCES

1. Yu. L. Klimontovich, *Statistical Physics of Open Systems* (Yanus, Moscow, 1995; Kluwer, Dordrecht, 1995), Vol. 1.
2. B. B. Mandelbrot, *The Fractal Geometry of Nature* (Freeman, New York, 1982).
3. R. Metzler and J. Klafter, Phys. Rep. **339**, 1 (2000).
4. W. G. Gloecke and T. F. Nonnemacher, J. Stat. Phys. **71** (34), 741 (1993).
5. V. V. Yanovsky, A. V. Chechkin, D. Schertzer, and A. V. Tur, Physica A (Amsterdam) **282**, 13 (2000).

6. A. V. Chechkin, R. Gorenflo, and I. M. Sokolov, Phys. Rev. E **66** (4), 046129 (2002).
7. V. L. Kobelev, E. P. Romanov, L. Ya. Kobelev, and Ya. L. Kobelev, Dokl. Akad. Nauk **361**, 755 (1998) [Dokl. Phys. **43**, 487 (1998)].
8. S. G. Samko, A. A. Kilbas, and O. I. Marichev, *Fractional Integrals and Derivatives, Theory and Applications* (Nauka i Tekhnika, Minsk, 1987; Gordon and Breach, Amsterdam, 1993).
9. I. M. Gelfand and G. E. Shilov, *Generalized Functions* (Academic, New York, 1964).
10. V. Ya. Shur, S. A. Negashev, E. L. Rumyantsev, *et al.*, Ferroelectrics **169**, 63 (1995).
11. P. V. Korolev and S. N. Kul'kov, Perspekt. Mater., No. 3, 21 (1997).
12. V. S. Ivanova, A. S. Balankin, I. Zh. Bunin, and A. A. Oksogoev, *Synergetics and Fractals in Materiology* (Nauka, Moscow, 1994).
13. L. Ya. Kobelev, *Fractal Theory of Time and Space*, Available from VINITI, No. 189-B99 (Moscow, 1999).
14. Ya. L. Kobelev, L. Ya. Kobelev, and E. P. Romanov, Dokl. Akad. Nauk **372**, 177 (2000) [Dokl. Phys. **45**, 439 (2000)].
15. L. Ya. Kobelev, in *Proceedings of 24th International Workshop on High Energy Physics and Field Theory, 27–29 June, Protvino, 2001*, p. 126 (http://dbserv.ihep.su/~pubs).

Translated by R. Tyapaev

Doklady Physics, Vol. 48, No. 6, 2003, pp. 269–273. Translated from Doklady Akademii Nauk, Vol. 390, No. 5, 2003, pp. 610–614.

PHYSICS

Excitation Cross Sections for the Strongly Perturbed $^1D_2$ Atomic Series of Barium

Yu. M. Smirnov

Presented by Academician F.V. Bunkin December 26, 2002

Received January 15, 2003

1. As the theory of the structure of atomic electron shells is developed, perturbations of atomic states are attracting increasing interest. This interest is primarily focused on the precise calculation of the positions of energy levels. The behavior of radiative lifetimes in perturbed series including high lying levels was also recently analyzed in the framework of multichannel quantum-defect theory (see, e.g., [1]). The corresponding results agree satisfactorily with experimental data.

However, similar calculations of cross sections for the excitation of atoms by an electron impact are virtually absent. This remark refers to excitation cross sections for spectral series, because perturbation (configuration mixing) was taken into account by Peterkop (see, e.g., [2] and discussion in [3]) and other authors in calculations of cross sections for individual low-lying levels. As a rule, only excitations of low-lying states are studied experimentally. Therefore, it is difficult to observe perturbation in the behavior of cross sections. This does not refer to experiments with the use of the method of extended crossing beams. In these experiments, the behavior of cross sections was studied up to $n \sim 20$ or higher [4]. The following three basic manifestations of perturbation were formulated in [4]: (i) deviation of the cross section magnitudes in a spectral series from the regular behavior, (ii) significant change in the shape of the optical excitation functions, (iii) significant change in the branching character.

Experimental investigations of perturbation in the behavior of excitation cross section are of considerable interest, the more so since corresponding theoretical investigations are sparse. It is known that the role of perturbations increases as a rule with the atomic mass of an element. For this reason, these investigations are particularly urgent for heavy atoms. In this paper, the experimental results for the perturbation effect on the behavior of excitation cross sections for $^1D_2$ atomic levels of barium are reported.

Moscow Power Engineering Institute (Technical University), ul. Krasnokazarmennaya 14, Moscow, 111250 Russia
e-mail: SmirnovYM@mpei.ru

2. The technique and procedure of experiments with extended crossing beams were discussed in detail in [5]. It is not difficult to form a barium atomic beam with the parameters necessary for an experiment. When a crucible with metallic barium is heated up to a temperature of 1100 K, the concentration of atoms in the crossing area of the atomic and electron beam reaches 6.6×10^{10} cm^{-3}. When intense resonance lines were detected, the atomic concentration was reduced to 1.5×10^9 cm^{-3}. As a result, reabsorption was reduced to negligible values.

Since the $6s^2\ ^1S_0$ ground atomic level of barium is a singlet separated from the nearest excited level by more than 9000 cm^{-1}, the role of thermal excitation in evaporation is extremely small. Therefore, the excitation of the barium atom in this experiment occurs from the only original level, $6s^2\ ^1S_0$. Other experimental conditions were not specific for barium and were presented in detail in previous works [4, 5]. Special attention was focused on the maintenance of stable experimental conditions, because this is one of most important factors of the correctness of analysis and comparison of the results.

3. In the emission spectrum excited in collisions of a 30-eV monoenergetic electron beam with barium atoms, 380 spectral lines were observed in the range 202–852 nm. Among them, 280 lines were attributed to the barium atom, 52 lines to a single-charged ion, and 47 lines were not identified. A considerable fraction of the last lines are undoubtedly attributed to transitions from high-lying $^1F_3^0$ levels with $n > 9$, for which reference data on the level positions are not available.

Among the results, information about the excitation of the $^1D_2$ levels is exceptional. The radiative lifetimes τ of these levels were measured by the method of pulse-modulated laser spectroscopy for the principal quantum numbers n = 8–17 [6] and 12–30 [7]. The results of these works are shown in Fig. 1, where deviations from the monotonic behavior are observed for the levels under consideration. These deviations are most pronounced in the data presented in [7]. We emphasize that a deviation from the regular behavior at n = 14 was

1028-3358/03/4806-0269$24.00

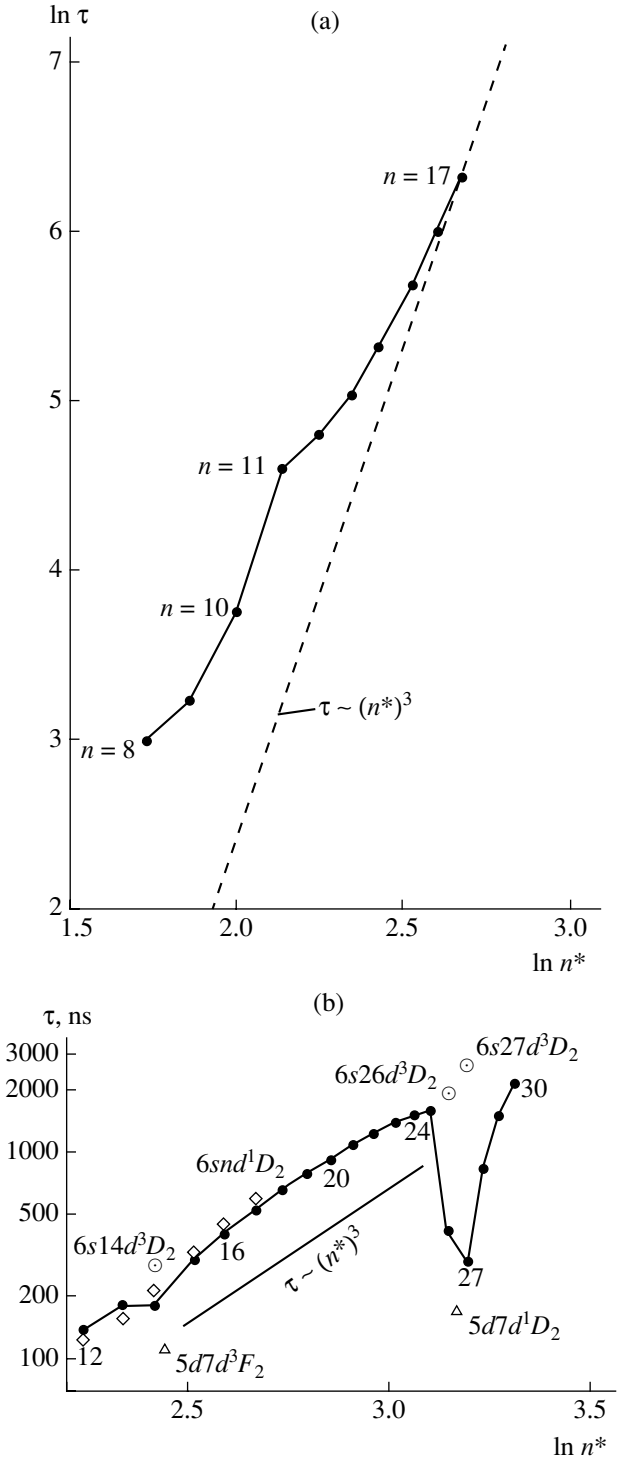

Fig. 1. Radiative lifetimes of the nd^1D_2 atomic levels of barium vs. the effective quantum number according to the data from (a) [6] and (b) [7]; triplet perturbing levels of the 6*snd* (n = 14, 26, 27) configuration are shown by ⊙ and of the 5*d*7*d* configuration are shown by △.

observed in [7] but was absent in the data obtained in [6]. The theoretical dependence $\tau = f(n)$ without perturbation (i.e., for hydrogen-like atoms or in the single-electron approximation) is given by $\tau \sim n^3$. For many-electron atoms, the effective quantum number n^* is used instead of the principal quantum number n. As was shown in [8], the behavior of radiative lifetimes strongly correlates with excitation cross sections in perturbed series.

Table 1 presents the measured excitation cross sections for BaI and necessary spectroscopic information. These data are the wavelength λ, transition and internal quantum number J, energies of lower E_{low} and upper E_{up} levels, excitation cross sections Q_{30} and Q_{max} for electron energy and at the maximum of optical excitation function, and the position of the maximum $E(Q_{max})$. The optical excitation functions in Table 1 are numbered according to the numbering of lines in Fig. 2. Data for lines that are absent in available sources and are classified in this work are given in Table 1 in parentheses. Most levels in Table 1 are attributed to the 6*snl* single-electron excitation configurations. However, there are also double-electron excitation levels attributed to the 5*dn*'*l*' configuration. Since the barium spectrum is very dense, some spectral lines overlap. In these cases, the contributions of lines to the total cross section are determined by separation based on all available data on the transition probabilities, oscillator strength, and branching ratios. Cross sections obtained by the separation procedure are marked by asterisks in Table 1.

When perturbations are absent, the cross sections q for excitation of energy levels in the single-electron approximation depend on n^* as $q \sim (n^*)^{-3}$. There is no theoretical prediction for cross sections Q for excitation of spectral lines (line emission cross sections). However, as was shown in many experiments, it has the following form in unperturbed series:

$$Q = A_i n^{-\alpha_i}, \quad (1)$$

where the constants A_i and α_i are individual for each spectral series. The function $Q = f(n)$ is most clearly represented as a plot in double logarithmic coordinates, because an exponential function is a straight line in these coordinates. Such functions for perturbed and unperturbed atomic series of calcium were presented in [4]. Figure 3 shows the function $Q = f(n)$ for the $6p^1P_1^0$–nd^1D_2 atomic series of barium. Significant irregularities are observed in excitation cross sections at n = 7, 11, 14, 24–27. The n = 25 line was not detected. The positions of these irregularities agree with those found in [6, 7]. Deviation from the monotonic power behavior is most pronounced at n = 14, in agreement with [7]. As was mentioned above, this deviation was not observed in [6].

As was known, perturbing and perturbed levels have the same parity [9]. For the barium-atom series under consideration, perturbing levels for $n > 12$, which are characterized by the 6*snd* and 5*d*7*d* configurations, are shown in Fig. 1b. Assumed perturbing levels for the

Table 1. Excitation cross sections for a barium atom

λ, nm	Transition	J	E_{low}, cm^{-1}	E_{up}, cm^{-1}	Q_{30}, 10^{-18} cm^2	Q_{max}, 10^{-18} cm^2	$E(Q_{max})$, eV	OEF
358.810	$5d^3D$–$5d7p^1D^0$	2–2	9215	37077	0.72	0.77	14	17
(377.485	$6p^3P^0$–$10d^1D$	2–2	13514	39998)	0.47	0.50	20	5
(387.183	$6p^3P^0$–$9d^1D$	2–2	13514	39334)	0.195	0.22	20	4
389.265	$5d^1D$–$5d7p^1D^0$	2–2	11395	37077	9.06	9.64	14	17
(396.701	$6p^3P^0$–$5d6d^1D$	1–2	12636	37837)	0.125	–	–	–
417.937	$6p^3P^0$–$7d^1D$	2–2	13514	37434	1.47	1.81	16	2
420.197	$6p^1P^0$–$27d^1D$	1–2	18060	41851	0.079	–	–	–
420.596	$6p^1P^0$–$26d^1D$	1–2	18060	41829	0.105	–	–	–
421.249	$6p^1P^0$–$24d^1D$	1–2	18060	41792	0.145	–	–	–
421.681	$6p^1P^0$–$23d^1D$	1–2	18060	41768	0.16	–	–	–
422.182	$6p^1P^0$–$22d^1D$	1–2	18060	41740	0.20	–	–	–
422.769	$6p^1P^0$–$21d^1D$	1–2	18060	41707	0.25	–	–	–
423.462	$6p^1P^0$–$20d^1D$	1–2	18060	41668	0.32	–	–	–
424.291	$6p^1P^0$–$19d^1D$	1–2	18060	41622	0.48*	0.53	20	14
425.288	$6p^1P^0$–$18d^1D$	1–2	18060	41567	0.71	0.77	20	13
426.506	$6p^1P^0$–$17d^1D$	1–2	18060	41499	1.01*	1.08	20	12
428.011	$6p^1P^0$–$16d^1D$	1–2	18060	41417	1.22	1.30	20	11
429.890	$6p^1P^0$–$15d^1D$	1–2	18060	41315	1.37	1.43	20	10
432.738	$6p^1P^0$–$14d^1D$	1–2	18060	41162	0.36	0.39	20	9
435.656	$6p^1P^0$–$13d^1D$	1–2	18060	41007	2.50	2.66	20	8
439.995	$6p^1P^0$–$12d^1D$	1–2	18060	40781	3.69	4.34	20	7
440.254	$6p^3P^0$–$6p^2\,^1D$	1–2	12636	35344	0.69	0.81	13; 19	15
445.839	$6p^1P^0$–$11d^1D$	1–2	18060	40483	3.85	4.42	20	6
451.066	$6p^1P^0$–$5d8s^1D$	1–2	18060	40223	0.60	–	–	–
455.700	$6p^1P^0$–$10d^1D$	1–2	18060	39998	10.0	10.6	20	5
457.964	$6p^3P^0$–$6p^2\,^1D$	2–2	13514	35344	5.30	6.22	13; 19	15
469.911	$6p^1P^0$–$9d^1D$	1–2	18060	39334	14.0*	15.8	20	4
487.765	$6p^1P^0$–$8d^1D$	1–2	18060	38556	24.6	28.9	18	3
492.935	$6p^3P^0$–$5d7s^1D$	2–2	13514	33795	0.13	–	–	–
505.498	$6p^1P^0$–$5d6d^1D$	1–2	18060	37837	0.29	–	–	–
515.994	$6p^1P^0$–$7d^1D$	1–2	18060	37434	18.7	23.1	16	2
568.018	$6p^3P^0$–$6d^1D$	1–2	12636	30236	5.12*	5.88	16	1
(578.868	$5d6p^3F^0$–$9d^1D$	2–2	22064	39334)	0.62	0.70	20	4
597.850	$6p^3P^0$–$6d^1D$	2–2	13514	30236	1.54	1.77	16	1
(610.086	$5d6p^3F^0$–$9d^1D$	3–2	22947	39334)	0.76	0.85	20	4
635.320	$6p^1P^0$–$5d7s^1D$	1–2	18060	33795	0.30	–	–	–
(645.743	$5d6p^1D^0$–$8d^1D$	2–2	23074	38556)	1.47	1.73	18	3
671.403	$5d6p^3F^0$–$5d6d^1D$	3–2	22947	37837	0.68	–	–	–
677.185	$5d6p^1D^0$–$5d6d^1D$	2–2	23074	37837	0.91	–	–	–
696.163	$5d6p^1D^0$–$7d^1D$	2–2	23074	37434	1.77	2.18	16	2
712.033	$5d^3D$–$5d6p^1D^0$	1–2	9033	23074	4.71	6.11	10	16
713.316	$5d^2\,^1D$–$5d7p^1D^0$	2–2	23062	37077	0.95	1.01	14	17
751.340	$5d6p^3D^0$–$5d6d^1D$	2–2	24531	37837	0.81	–	–	–
752.820	$5d6p^3F^0$–$6p^2\,^1D$	2–2	22064	35344	1.28	1.50	13; 19	15
821.024	$6p^1P^0$–$6d^1D$	1–2	18060	30236	71.6	82.3	16	1
852.196	$5d6p^3F^0$–$5d7s^1D$	2–2	22064	33795	3.82	–	–	–

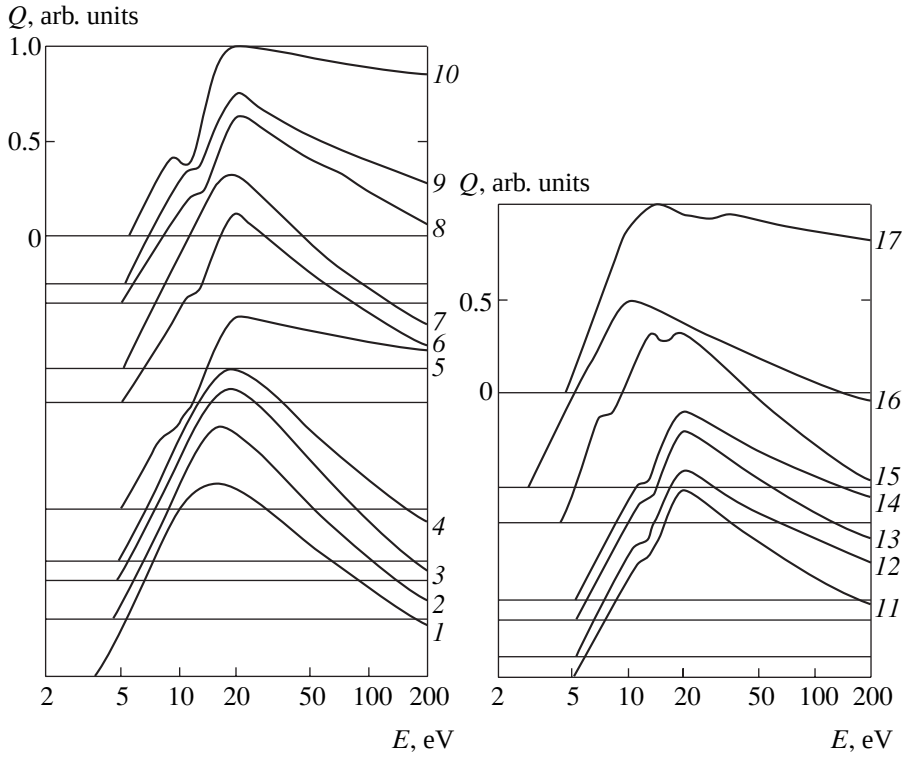

Fig. 2. Optical excitation functions of the $6p\,^1P_1^0$–$nd\,^1D_2$ spectral series of BaI.

$6snd\,^1D_2$ levels with $n < 12$ were indicated in [6]. These levels are the $5d8s\,^1D_2$ level with $E = 40223$ cm^{-1} for the $n = 10$, 11 levels and the $5d6d\,^1D_2$ level with $E = 37837$ cm^{-1} for the $n = 8$ level. We note that intervals between perturbed and perturbing levels are large and reach 225, 260, and 719 cm^{-1}, respectively.

At the same time, any data on the perturbation of the radiative lifetime of the $7d\,^1D_2$ level were absent in [6, 7], because $n < 8$ levels were not investigated. However, perturbation of this level was observed in [10], where cross sections for transitions from the $nd\,^1D_2$ levels for $n = 6$–9 were measured. Table 2 presents cross sections obtained for an electron energy of 30 eV in this work and in [10]. Results differ by about 10% or less, and the difference reaches almost 36% only for the headline lying in the IR spectrum. The general behavior of the function $Q = f(n)$ is virtually the same, with a pronounced minimum at $n = 7$ compared to $n = 6$ and 8. The perturbing level for the $n = 7$ level is apparently the above-mentioned $5d6d\,^1D_2$ level spaced from the level under consideration by 403 cm^{-1}, i.e., closer than to the $n = 8$ level.

Excitation cross sections are measured for a number of transitions involving doubly excited levels, as well as for the transitions in the perturbed $6p\,^1P_1^0$–$nd\,^1D_2$ series. However, these data are sparse and cannot be analyzed and generalized. At the same time, these data can be of interest for further theoretical analysis of cross sections, because many doubly excited levels are responsible for perturbations in the spectral series of single-electron excitation.

The optical excitation functions shown in Fig. 2 noticeably change their shapes for $n = 10$, 11 and 14, 15

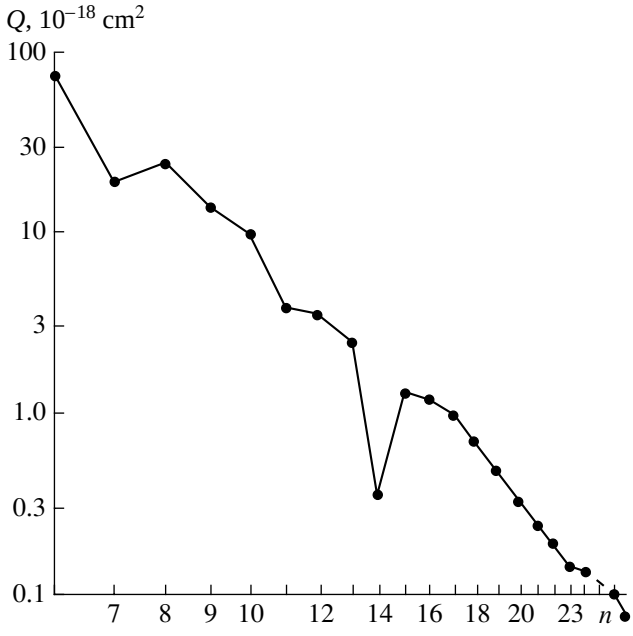

Fig. 3. $Q = f(n)$ for $6p\,^1P_1^0$–$nd\,^1D_2$ spectral series of BaI.

Table 2. Excitation cross sections for the $6p^1P_1^0$–nd^1D^2 atomic series of barium for an electron energy of 30 eV

n	E_{up}, cm^{-1}	λ, nm	Q_{30}, 10^{-18} cm^2	
			this work	[10]
6	30236	821.024	71.6	110
7	37434	515.994	18.7	20
8	38556	487.765	24.6	25
9	39334	469.911	14.0*	16

as compared to the optical excitation functions for unperturbed lines of the series. Similar changes were previously observed in the $^1D_2$ atomic series of calcium [4], where perturbation was manifested at $n = 8$. However, this effect is not analyzed theoretically, as far as I know.

4. Significant perturbation was observed in excitation cross sections in the $6p^1P_1^0$–nd^1D_2 atomic spectral series of barium. The most probable perturbing levels are attributed to the 6*snd*, 5*d*8*s*, 5*d*6*d*, and 5*d*7*d* even configurations.

REFERENCES

1. C. J. Dai, Phys. Rev. A **52** (6), 4416 (1995).
2. R. K. Peterkop, Opt. Spektrosk. **58** (1), 14 (1985) [Opt. Spectrosc. **58**, 7 (1985)].
3. L. L. Shimon, Opt. Spektrosk. **54** (5), 772 (1983) [Opt. Spectrosc. **54**, 458 (1983)].
4. A. N. Kuchenev and Yu. M. Smirnov, Phys. Scr. **51** (5), 578 (1995).
5. Yu. M. Smirnov, J. Phys. II **4** (1), 23 (1994).
6. D. Kaiser, P. Kulina, A. E. Livingston, *et al.*, Z. Phys. A: At. Nucl. **285** (2), 111 (1978).
7. K. Bhatia, P. Grafström, C. Levinson, *et al.*, Z. Phys. A: At. Nucl. **303** (2), 1 (1981).
8. A. N. Kuchenev and Yu. M. Smirnov, Zh. Prikl. Spektrosk. **53** (4), 666 (1990).
9. I. I. Sobelman, *Atomic Spectra and Radiative Transitions* (Fizmatgiz, Moscow, 1963; Springer-Verlag, Berlin, 1979).
10. I. S. Aleksakhin, I. P. Zapesochnyi, I. I. Garga, and V. P. Starodub, Opt. Spektrosk. **38** (2), 228 (1975) [Opt. Spectrosc. **38**, 126 (1975)].

Translated by R. Tyapaev

Doklady Physics, Vol. 48, No. 6, 2003, pp. 274–276. Translated from Doklady Akademii Nauk, Vol. 390, No. 5, 2003, pp. 615–617.

PHYSICS

The Effect of Octupole Transitions on the Intensity of X-ray–Photoelectron Spectra under Photoionization

M. B. Trzhaskovskaya*, Corresponding Member of the RAS V. I. Nefedov, V. G. Yarzhemsky**, and R. Szargan*****

Received February 7, 2003

In contrast to widely propagated concepts, nondipole transitions, in particular dipole–quadrupole and quadrupole transitions, significantly contribute to both the intensity distribution and angular distribution of photoelectrons under photoionization. As was shown in recent studies [1–11], this takes place even at relatively low photoelectron energies 0.5–1 keV. At present, only one paper [7] is known in which its authors declared that (under certain experimental conditions) there exists a possibility to observe an effect of octupole transitions on ionization of the 2*p*-shell of a neon atom. This effect can manifest itself in the case of determining parameters of dipole–quadrupole transitions for photoelectron energies lower than 1 keV. It is worth noting that the experiment of [7] was carried out with linearly polarized radiation.

The goal of the present study is to clarify the effect of octupole transitions on the intensity of the resulting spectra under usual experimental conditions and in the case of both unpolarized and polarized exciting radiation. Solving this problem is important from the theoretical standpoint, as well as for the practical application of X-ray–photoelectron quantitative analysis of solid surfaces in the case of determining sensitivity factors.

Under excitation of photoelectron spectra by unpolarized radiation, the photoelectron angular distribution has the form [6]

$$\frac{d\sigma_i}{d\Omega} = \frac{\sigma_i}{4\pi}[1 - 0.5\beta_i P_2(\cos\theta) + (\delta_i + 0.5\gamma_i \sin^2\theta)\cos\theta]. \quad (1)$$

Here, σ_i is the photoionization cross section for the *i*th atomic shell, $P_2(\cos\theta)$ is the second Legendre polynomial, and θ is the angle between the photon propagation vector and the direction of the photoelectron emission. In formula (2), terms on the order of $O(k^1, r^1)$ are taken into account, where k is the photon energy and r is the radius of an atomic shell being ionized. The parameter β describes (in the dipole approximation) the photon angular distribution. The two additional parameters γ and δ describe the $E1$–$E2$ and $E1$–$M1$ interactions. Denotations E and M correspond to the electric and magnetic interactions, respectively, whereas a number following E or M indicates multiple order. For example, $E1$–$E2$ implies the electric dipole-quadrupole interaction that predominantly contributes to the parameters γ and δ.

The formula for the photoelectron angular distribution in the octupole approximation for linearly polarized exciting radiation is given in [7], while the formula for the excitation by unpolarized radiation,

$$\frac{d\sigma_i}{d\Omega} = \frac{\sigma_i}{4\pi}[1 - 0.5(\beta + \Delta\beta_{\text{unpol}})P_2(\cos\theta) + (\delta_i + 0.5\gamma_i \sin^2\theta)\cos\theta + \xi P_4(\cos\theta)] \quad (2)$$

is obtained for the first time in the present paper. Here, in contrast to Eq. (1), two additional terms, $\Delta\beta_{\text{unpol}}$ and ξ, appear. The notation for the parameters corresponds to that used in [7] for linearly polarized exciting radiation.

The parameter $\Delta\beta_{\text{unpol}}$ involves the terms $M1$–$M1$, $E1$–$M2$, $M1$–$E2$, $E2$–$E2$, and $E1$–$E3$, as well as the $(kr)^2$-order correction to the $E1$–$E1$ terms. The parameter ξ is associated with the $E2$–$E2$ and $E1$–$E3$ interactions.

In the case of linearly polarized exciting radiation, it is necessary to introduce into formula (1) (see [7]) four additional parameters, namely, $\Delta\beta_{\text{pol}}$, η, μ, and ξ. The interactions corresponding to these parameters are also

* *Petersburg Nuclear Physics Institute, Russian Academy of Sciences, Gatchina, St. Petersburg, 188350 Russia*

** *Kurnakov Institute of General and Inorganic Chemistry, Russian Academy of Sciences, Leninskiĭ pr. 31, Moscow, 119991 Russia*
e-mail: vgvar@igic.ras.ru

*** *Leipzig University, Leipzig, Germany*

1028-3358/03/4806-0274$24.00 © 2003 MAIK "Nauka/Interperiodica"

Table 1. Nondipole parameters for 1*s* shells. The first and second lines in the table relate to E_{kin} = 5 and 10 keV, respectively

Atom	γ	$\eta \times 10^2$	$\mu \times 10^2$	$\xi \times 10^2$	$\Delta\beta_{unpol} \times 10^2$	$\Delta\beta_{pol} \times 10^2$
Li	1.640	2.70	3.77	−6.48	−9.90	−1.82
	2.312	5.42	7.56	−13.0	−19.8	−3.65
Be	1.627	2.65	3.70	−6.36	−9.70	−1.76
	2.302	5.37	7.46	−12.9	−19.6	−3.60
B	1.613	2.61	3.64	−6.25	−9.51	−1.71
	2.292	5.32	7.41	−12.7	−19.4	−3.54
C	1.600	2.56	3.58	−6.15	−9.34	−1.70
	2.280	5.27	7.34	−12.6	−19.2	−3.49
N	1.589	2.53	3.54	−6.07	−9.21	−1.63
	2.268	5.21	7.26	−12.5	−19.0	−3.42
O	1.579	2.50	3.49	−6.00	−9.07	−1.58
	2.256	5.16	7.19	−12.4	−18.8	−3.36
F	1.567	2.47	3.45	−5.92	−8.90	−1.52
	2.147	5.12	7.14	−12.3	−18.6	−3.31
Ne	1.554	2.43	3.39	−5.82	−8.72	−1.46
	2.237	5.08	7.08	−12.2	−18.4	−3.24

given in [7]. The quantities $\Delta\beta_{pol}$ and $\Delta\beta_{unpol}$ differ for the excitation of spectra by polarized or unpolarized radiation, whereas the values of ξ are the same. The parameters are related as

$$\eta + \mu + \xi = 0. \tag{3}$$

For the "magic" angles $\cos^2\theta = \frac{1}{3}$ and $\cos^2\underline{\theta} = \frac{1}{3}$ (θ is the angle between the directions of an emitted photoelectron and the polarization vector of the exciting linearly polarized radiation), in accordance with formula (2) of [7], we have for linearly polarized radiation ($\phi = 0$)

$$\frac{d\sigma_i}{d\Omega} = \frac{d\sigma_i}{4\pi}(1 + 0.272\gamma + 0.861\delta + 1.778\mu + 0.778\eta). \tag{4}$$

At the same time, in accordance with formula (2) of the present paper, for unpolarized exciting radiation, we have

$$\frac{d\sigma_i}{d\Omega} = \frac{\sigma_i}{4\pi}(1 + 0.192\gamma + 0.577\delta - 0.389\xi). \tag{5}$$

Relativistic calculations of the parameters β, $\Delta\beta$, γ, δ, η, μ, and ξ (see [1] for details) were performed with allowance for the Dirac–Fock–Slater potential with the coefficient C = 1 taken for the exchange term. The vacancy arising after the photoelectron had been emit-

Table 2. Nondipole parameters for 2*s* and 2*p* shells (E_{kin} = 500 eV)

Atom	Shell	$\gamma \times 10$	$\delta \times 100$	$\eta \times 10^4$	$\mu \times 10^4$	$\xi \times 10^3$	$\Delta\beta_{unpol} \times 10^3$	$\Delta\beta_{pol} \times 10^4$
Li	2*s*	4.68		21.8	30.5	−5.23	−7.88	−13.4
Be	2*s*	4.29		18.4	25.7	−4.41	−6.59	−10.7
B	2*s*	3.9		15.2	21.3	−3.66	−5.37	−7.97
	$2p_{1/2}$	2.62		1.85	42.5	−4.44	−12.7	−21.8
C	2*s*	3.49		12.1	17.0	−2.91	−4.16	−5.26
	$2p_{1/2}$	2.88	5.84	3.92	40.7	−4.62	−12.3	−19.2
N	2*s*	3.03		9.14	12.7	−2.19	−3.04	−3.00
	$2p_{1/2}$	3.10	4.37	5.30	38.9	−4.42	−11.3	−18.3
	$2p_{3/2}$	3.11	4.37	12.4	31.8	−4.42	−9.17	−18.3
O	2*s*	2.57		6.52	9.12	−1.56	−2.07	−1.13
	$2p_{1/2}$	3.21	3.81	6.02	36.4	−4.25	−10.5	−16.7
	$2p_{3/2}$	3.22	3.80	12.5	30.0	−4.25	−8.54	−16.7
F	2*s*	2.12		4.19	5.86	−1.01	−1.21	−0.419
	$2p_{1/2}$	3.26	3.40	6.19	34.1	−4.03	−9.75	−15.2
	$2p_{3/2}$	3.27	3.39	12.3	28.1	−4.04	−7.93	−15.2
Ne	2*s*	1.67		2.24	3.14	−0.538	−0.523	−0.15
	$2p_{1/2}$	3.25	3.09	5.89	31.8	−3.77	−9.04	−13.8
	$2p_{3/2}$	3.25	3.09	11.8	26.0	−3.78	−7.28	−13.8

ted was taken into account in the approximation of frozen orbitals. In this case, experimental values for electron binding energies in atoms were used.

Quantitative calculations of nondipole parameters were carried out for atoms from Li to Ne. The 1*s* shells (excitation by Al(K_α) line and by the Mg(K_α) line, as well as at photoelectron kinetic energies of 5 and 10 keV) and 2*s* and 2*p* shells (E_{kin} = 0.5 keV and E_{kin} = 1 keV) were analyzed. In Tables 1 and 2, data are given for 2*s* and 2*p* shells (E_{kin} = 0.5 keV) and for the 1*s* shell (E_{kin} = 5 and 10 keV).

The values of δ for *s* shells are omitted due to their smallness. In the nonrelativistic approximation, $\delta = 0$. The contribution of octupole transitions to the total intensity of the photoionization spectrum was calculated for the "magic" angles. In all cases, these contributions for 1*s* shells (excitation by the Al(K_α) line and by the Mg(K_α) line), as well as for 2*s* and 2*p* shells (E_{kin} = 0.5 and 1 keV), are virtually lower than 1%. In other words, we may ignore these contributions when performing quantitative X-ray–photoelectron analysis within the range of the indicated excitation energies.

The situation is noticeably transformed in the case of 1*s* shells at kinetic energies of 5 and 10 keV. For magic angles, when passing from Li to Ne and in the case of unpolarized exciting radiation, the contribution of octupole transitions decreases from 1.9 to 1.0% (E_{kin} = 5 keV) and from 3.4 to 1.6% (E_{kin} = 10 keV). In the case of linearly polarized radiation, these values change from 6.0 to 5.6% and from 10.6 to 8.1%, respectively. Evidently, these significant contributions of octupole transitions should be taken into account at the photoelectron energies under consideration, especially in the case of linearly polarized exciting radiation.

ACKNOWLEDGMENTS

This work was supported by the Russian Foundation for Basic Research, project no. 02-03-32693, and by the Alexander von Humboldt Foundation.

REFERENCES

1. M. B. Trzhaskovskaya, V. I. Nefedov, and V. G. Yarzhemsky, At. Data Nucl. Data Tables **77**, 97 (2001).
2. M. B. Trzhaskovskaya, V. K. Nikulin, V. I. Nefedov, and V. G. Yarzhemsky, J. Phys. B **34**, 221 (2001).
3. V. I. Nefedov, V. G. Yarzhemsky, I. S. Nefedova, *et al.*, J. Electron. Spectrosc. Relat. Phenom. **107**, 123 (2000).
4. V. I. Nefedov and I. S. Nefedova, J. Electron. Spectrosc. Relat. Phenom. **113**, 3 (2000).
5. V. I. Nefedov, V. G. Yarzhemsky, R. Hesse, *et al.*, J. Electron. Spectrosc. Relat. Phenom. **125**, 153 (2002).
6. J. W. Cooper, Phys. Rev. A **47**, 1841 (1993).
7. A. Derevianko, O. Hemmers, S. Oblad, *et al.*, Phys. Rev. Lett. **84**, 2116 (2000).
8. V. I. Nefedov and I. S. Nefedova, Poverkhnost **4**, 50 (2000).
9. V. I. Nefedov, V. G. Yarzhemsky, I. S. Nefedova, *et al.*, Poverkhnost **6**, 10 (2000).
10. V. I. Nefedov, I. S. Nefedova, V. G. Yarzhemsky, *et al.*, Dokl. Akad. Nauk **385**, 515 (2002) [Dokl. Phys. **47**, 583 (2002)].
11. V. I. Nefedov, V. G. Yarzhemsky, I. S. Nefedova, *et al.*, Dokl. Akad. Nauk **367**, 324 (1999) [Dokl. Phys. **44**, 423 (1999)].

Translated by G. Merzon

Doklady Physics, Vol. 48, No. 6, 2003, pp. 277–281. Translated from Doklady Akademii Nauk, Vol. 390, No. 6, 2003, pp. 750–754.

PHYSICS

"Static" Mössbauer Spectra of the Magnetic Hyperfine Structure of Superparamagnetic Particles

Corresponding Member of the RAS A. M. Afanas'ev* and M. A. Chuev**

Received February 14, 2003

Mössbauer absorption spectra of magnetic materials are usually analyzed with the inclusion of group lines (subspectra) formed due to hyperfine interaction in a static hyperfine magnetic field on a nucleus and lines attributed to the quadrupole interaction in the presence of the electric-field gradient on the nucleus. In particular, for the ^{57}Fe isotope most extensively used in Mössbauer spectroscopy, the hyperfine magnetic field splits the levels of the ground state of the nucleus with spin $I_g = \frac{1}{2}$ into two sublevels with different spin projections m_g onto the hyperfine-field direction. The excited 14.4-keV state with spin $I_e = \frac{3}{2}$ is split into four sublevels with different spin projections m_e in accordance with the energies of the Zeeman interaction between magnetic moments of the nucleus and the hyperfine magnetic field $\mathbf{H}_{hf}$:

$$\hat{H}^{(g,e)} = -g_{g,e}\mu_N \mathbf{H}_{hf}\hat{\mathbf{I}}^{(g,e)}. \quad (1)$$

Here, μ_N is the nuclear magneton and $g_{g,e}$ are the nuclear g factors and $\hat{\mathbf{I}}^{(g,e)}$ are the nuclear spins of the ground and excited nuclear states, respectively. Figure 1 shows the splitting scheme of nuclear energy levels.

Transitions can occur between split nuclear sublevels in the excited and ground states. These transitions are observed in experimental absorption spectra as a certain set of lines, whose positions and intensities are completely determined by Hamiltonian (1) and the multipole order of the corresponding transition from the ground state of the nucleus to the excited state. These transitions in ^{57}Fe nuclei are accompanied by M1 magnetic dipole radiation, which cannot change the nuclear spin projection by more than one unit $\left(m_g = \pm\frac{1}{2} \rightarrow m_e = \mp\frac{3}{2}\right)$. For this reason, the absorption spectrum consists of six lines, a so-called magnetic sextet, rather than of eight lines corresponding to the splitting scheme shown in Fig. 1 [1]. In addition, in polycrystalline samples or magnetic alloys, when the hyperfine field on the nucleus is oriented arbitrarily, the intensities of corresponding spectral lines are related as 3 : 2 : 1 : 1 : 2 : 3 (see Fig. 1).

The majority of Mössbauer spectra of magnetic materials are analyzed with the inclusion of this magnetic sextet. Experimental spectra are approximated by a combination of sextets corresponding to different hyperfine fields. These sextets arise due to the presence

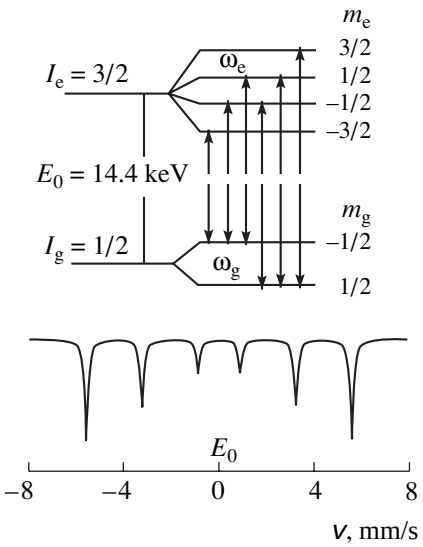

Fig. 1. (Upper) Splitting scheme for the energy levels of the ^{57}Fe nucleus in (e) excited and (g) ground states in the static hyperfine field and (lower) the corresponding Mössbauer absorption spectrum, magnetic sextet.

Institute of Physics and Technology,
Russian Academy of Sciences,
Nakhimovskiĭ pr. 36, Moscow, 117218 Russia
** e-mail: afanasev@ftian.oivta.ru*
*** e-mail: chuev@ftian.oivta.ru*

1028-3358/03/4806-0277$24.00

of different magnetic phases, magnetic sublattices in ferrimagnetic and antiferromagnetic substances, and defects in the crystal structure. If experimental spectra do not fit this scheme, more complex models are involved to describe so-called relaxation effects (e.g., for paramagnets [2], ferrofluids [3], superparamagnetic particles [4], etc.), when the magnitude and direction of the hyperfine field on the nucleus vary randomly in time due to spin–lattice, spin–spin, or other relaxation processes.

As was mentioned above, the ground and excited states of the ^{57}Fe isotope have different spins. In addition, the nuclear g factors of these states differ from each other not only in magnitude but also in sign (g_g = 0.18 and g_e = –0.10). This circumstance is substantial for the phenomena considered below.

The magnetic moment of superparamagnetic particles and, therefore, the hyperfine field on a nucleus rotate about the easiest magnetization axis of the particle. This phenomenon is known in Mössbauer spectroscopy. However, this phenomenon is analyzed under the assumption that the characteristic precession frequency Ω of the magnetic moment of the particle is much higher than the precession frequency of the nuclear spin in the hyperfine field. In this case, the magnetic sextet typical for static spectra is formed [5]. The ratio of the frequency Ω to the precession frequencies of nuclear spins in the hyperfine field can be different in real samples. In these cases, spectra can qualitatively differ from known static hyperfine-structure spectra. In particular, as will be shown below, spectra consisting of three, four, and five lines arise for the ^{57}Fe isotope in addition to the static magnetic sextets. In other words, the hyperfine-structure spectra of ^{57}Fe nuclei can include magnetic triplets, quartets, and quintets. If this fact is disregarded, analysis of hyperfine-structure spectra can face insuperable difficulties even when these anomalies are not pronounced but smeared due to the superposition of partial spectra and relaxation effects.

Let us consider a small particle that can be considered as uniformly magnetized. Such particles are usually magnetically anisotropic. For axial magnetic anisotropy, the energy of such a particle is determined by the known expression

$$E = -KV\cos^2\theta, \tag{2}$$

where K is the magnetic-anisotropy constant, V is the particle volume, and θ is the angle between the magnetic moment of the particle and symmetry axis. For $K > 0$, i.e., when the easiest magnetization axis exists, the anisotropy energy is minimal for $\theta = 0$ and π, when the magnetic moment of the particle is directed along the symmetry axis. Current technologies make it possible to grow systems with very small magnetic particles whose size is equal to about several nanometers (see, e.g., [6–10]). In this case, the quantity $\frac{KV}{k_B}$ (k_B is the Boltzmann constant) is equal to about several hundred degrees Kelvin due to small volume, so that all states with arbitrary directions of the magnetic moment with respect to the anisotropy axis are occupied, even for room temperature.

It is well known that the magnetic moment deviating at a certain angle θ from the easiest magnetization axis precesses about this axis with the frequency [11]

$$\Omega = -\gamma H_{an}. \tag{3}$$

Here, γ is the gyromagnetic ratio and H_{an} is the magnetic anisotropy field determined from the equation

$$H_{an} = -\frac{\partial E}{\partial M_z} = \frac{2KV\cos\theta}{M_0}, \tag{4}$$

where M_z is the magnetic-moment projection of the particle onto the easiest magnetization axis and M_0 is the saturation magnetic moment of the particle. Then, the precession frequency is expressed as

$$\Omega = \Omega_0\cos\theta, \tag{5}$$

where

$$\Omega_0 = -\frac{2\gamma KV}{M_0}. \tag{6}$$

These formulas show that the precession frequency Ω is independent of the particle volume, because the magnetic moment of the particle is proportional to its volume and is determined by the deviation angle θ. It is substantial that the precession frequency Ω is maximal for small angles θ and vanishes for $\theta = \frac{\pi}{2}$. Therefore, the angle range θ, where the frequency Ω is comparable with the precession frequencies of nuclear spins in the hyperfine field always exists.

The hyperfine field on the nucleus follows the magnetic moment, i.e., rotates about the magnetic anisotropy axis:

$$\mathbf{H}_{hf}(t) = H_{hf}\lfloor \mathbf{n}_z\cos\theta + (\mathbf{n}_x\cos(\Omega t) + \mathbf{n}_y\sin(\Omega t))\sin\theta \rfloor, \tag{7}$$

where $\mathbf{n}_x$, $\mathbf{n}_y$, and $\mathbf{n}_z$ are the unit vectors of the x, y, and z axes, respectively. This phenomenon is well known in the Mössbauer spectroscopy of superparamagnetic particles. However, it is taken into account under the assumption that the characteristic frequency Ω is much higher than the precession frequency of nuclear spins. In this case, the time-dependent hyperfine field compo-

nent vanishes after averaging, and the rotation-averaged hyperfine field is given by the expression

$$\bar{\mathbf{H}}_{\mathrm{hf}} = H_{\mathrm{hf}}\cos\theta\mathbf{n}_z. \quad (8)$$

Particular estimates show that only lower energy states with $\theta \ll 1$ are occupied for large particles. At the same time, for superparamagnetic particles, whose sizes are equal to about several nanometers, the frequency Ω_0 is only several times higher than the precession frequency of the nuclear spin in the hyperfine magnetic field. As θ increases, the frequency Ω can become equal to or lower than nuclear-precession frequencies. As will be shown below, the magnetic hyperfine structure of Mössbauer spectra is substantially rearranged when the finiteness of Ω is taken into account.

Hamiltonians of the hyperfine interaction between magnetic moments of the nucleus in the ground and excited states and the hyperfine magnetic field $\mathbf{H}_{\mathrm{hf}}$ rotating about the z axis with the frequency Ω depend on time:

$$\hat{H}^{(\mathrm{g,e})}(t) = -g_{\mathrm{g,e}}\mu_N\mathbf{H}_{\mathrm{hf}}(t)\hat{\mathbf{I}}^{(\mathrm{g,e})}. \quad (9)$$

We note that a quadrupole interaction between the nuclear spin and the electric field gradient on the nucleus also exists. However, it is as a rule significantly smaller than the hyperfine interaction and will be neglected below. In the coordinate system rotating about the z axis with the frequency Ω, Hamiltonians (9) take the form of time-independent operators:

$$\hat{\tilde{H}}^{(\mathrm{g,e})} = (-\Omega + \omega_{\mathrm{g,e}}\cos\theta)\hat{I}_z^{(\mathrm{g,e})} + \omega_{\mathrm{g,e}}\sin\theta\hat{I}_x^{(\mathrm{g,e})}, \quad (10)$$

where $\omega_{\mathrm{g,e}} = -g_{\mathrm{g,e}}\mu_N H_{\mathrm{hf}}$ are the hyperfine-splitting constants for the ground and excited states of the nucleus, respectively. The eigenvalues of operators (10) are obviously determined by the expression

$$\tilde{E}_{\mathrm{g,e}} = \tilde{\lambda}_{\mathrm{g,e}}\tilde{m}_{\mathrm{g,e}}, \quad (11)$$

where

$$\tilde{\lambda}_{\mathrm{g,e}} = \sqrt{(-\Omega + \omega_{\mathrm{g,e}}\cos\theta)^2 + \omega_{\mathrm{g,e}}^2\sin^2\theta}, \quad (12)$$

and $\tilde{m}_{\mathrm{g,e}}$ are the nuclear-spin projection on the quantization axes for which operators $\hat{\tilde{H}}^{(\mathrm{g,e})}$ are diagonal. As is seen in Fig. 2, the quantization axis for the ground state differs from the axis for the excited state.

An analytical expression for the cross section for the absorption of a gamma-ray photon by the nucleus was obtained in [12] for the case where the hyperfine field on the nucleus rotates in the plane perpendicular to the rotation axis. This result is easily generalized to the case of hyperfine field (7) rotating at arbitrary angle θ.

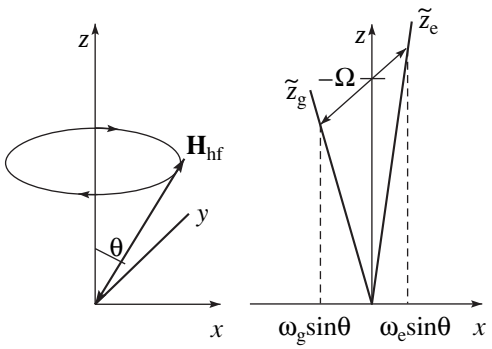

Fig. 2. Rotating hyperfine field in the laboratory coordinate system and the quantization axes for operators (10) for the ground and excited states of the ^{57}Fe nucleus and positive K (negative frequency Ω) in the rotating coordinate system.

In this case, absorption cross section with allowance for averaging over the polarization η of the incident radiation is expressed as

$$\sigma(\omega) = -\frac{\Gamma_0}{2}\mathrm{Im}\sum_{\eta}\sum_{\substack{m_\mathrm{g}m_\mathrm{e}\\ \tilde{m}_\mathrm{g}\tilde{m}_\mathrm{e}}} V^{(\eta)+}_{\tilde{m}_\mathrm{g}\tilde{m}_\mathrm{e}} \times \frac{\langle\tilde{m}_\mathrm{g}|m_\mathrm{g}\rangle\langle m_\mathrm{e}|\tilde{m}_\mathrm{e}\rangle}{\omega - (\tilde{\lambda}_\mathrm{e}\tilde{m}_\mathrm{e} - \tilde{\lambda}_\mathrm{g}\tilde{m}_\mathrm{g}) - \Omega(m_\mathrm{g} - m_\mathrm{e}) + i\Gamma_0/2} V^{(\eta)}_{m_\mathrm{e}m_\mathrm{g}}, \quad (13)$$

where ω is the spectral frequency, Γ_0 is the line width of the excited state of the nucleus, $V^{(\eta)}_{m_\mathrm{e}m_\mathrm{g}}$ are the matrix elements of the interaction operator between a gamma-ray photon and the nucleus, and $m_{\mathrm{g,e}}$ are the nuclear-spin projections onto the z axis.

According to Eq. (13), when the hyperfine field rotates, the absorption spectrum must involve pronounced natural-width lines, whose number is generally equal to $N = (2I_\mathrm{g} + 1)^2(2I_\mathrm{e} + 1)^2$. For the ^{57}Fe isotope, $N = 64$. However, the selection rule for M1 magnetic dipole transitions reduces the number of resolved lines to 24, each of which is doubly degenerate, because $(m_\mathrm{g}, m_\mathrm{e})$ and $(m_\mathrm{g} \pm 1, m_\mathrm{e} \pm 1)$ lines have identical transition energies.

Figure 3 shows the Mössbauer absorption spectra of ^{57}Fe nuclei for the hyperfine field rotating about the easiest magnetization axis at an angle of $\theta = 80°$ for various Ω_0 values corresponding to various magnetic-anisotropy constants K. It is seen that three-, four-, and five-line spectra can be formed instead of the classical six lines of the static (relaxation processes are ignored) hyperfine structure. In other words, the rotation of the magnetic moment can fundamentally rearrange hyperfine-structure spectra.

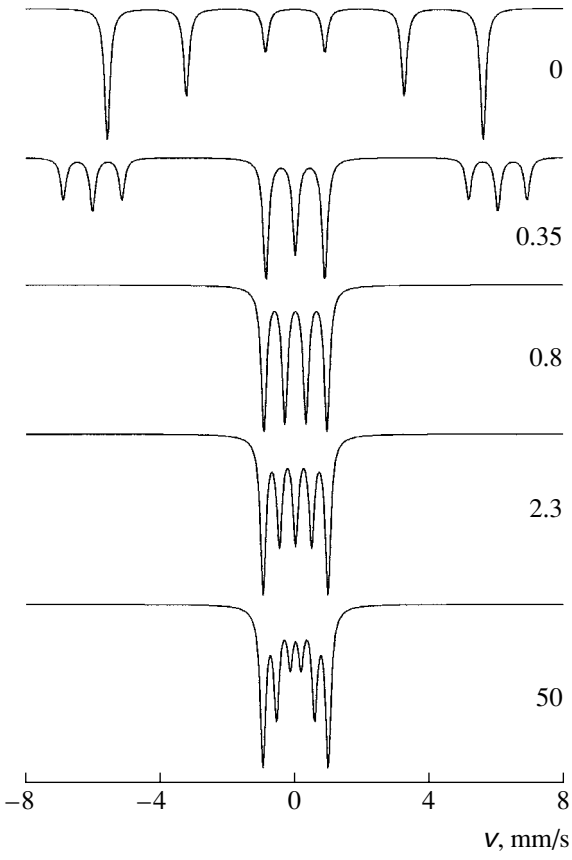

Fig. 3. Mössbauer absorption spectra of ^{57}Fe nuclei in the rotating hyperfine field with the parameters H_{hf} = 330 kOe and θ = 80° and for $\frac{\Omega_0}{2\pi}$ = (from top to bottom) 0, 0.35, 0.8, 2.3, and 50 GHz.

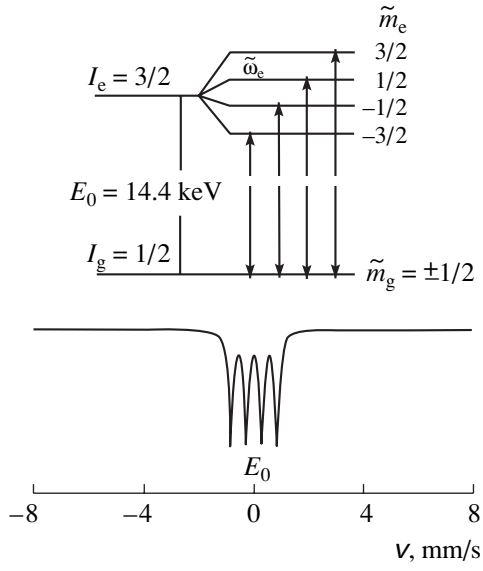

Fig. 4. (Upper) Splitting scheme for energy levels of the ^{57}Fe nucleus in (e) excited and (g) ground states in the rotating hyperfine field with the parameters H_{hf} = 330 kOe, $\Omega_0/2\pi$ = 1 GHz, θ = 81°, and $\tilde{\omega}_g$ = 0 and (lower) the corresponding Mössbauer absorption spectrum, magnetic quartet.

The physical origin of such a fundamental transformation of spectra can be revealed by analyzing the case of high rotation frequencies, when

$$|\Omega| \gg |\omega_{g,e}|. \tag{14}$$

In this case, the spectrum is divided into the central group of six doubly degenerate lines and side groups of lines (satellites). The shape of satellites is not analyzed here, because they are far beyond the velocity range of Mössbauer spectrometers, when condition (14) is satisfied.

The $\tilde{m}_g = m_g$ and $\tilde{m}_e = m_e$ central lines make the basic contribution to the absorption intensity, and it is easy to express the absorption cross section as

$$\sigma(\omega) = -\frac{\Gamma_0}{2}\mathrm{Im}\sum_{\eta}\sum_{m_g m_e}\left|V^{(\eta)}_{m_e m_g}\right|^2 \times \frac{1}{\omega - (\tilde{\omega}_e m_e - \tilde{\omega}_g m_g) + i\Gamma_0/2}. \tag{15}$$

Here, the effective hyperfine-splitting constants $\tilde{\omega}_g$ and $\tilde{\omega}_e$ for the ground and excited nuclear states, respectively, are determined from Eq. (12) by taking into account Eq. (14) in the form

$$\tilde{\omega}_{g,e} = -\tilde{g}_{g,e}\mu_N H_{hf}\cos\theta, \tag{16}$$

where

$$\tilde{g}_{g,e} = g_{g,e}\left(1 - \frac{\omega_{g,e}}{2\Omega}\sin\theta\tan\theta\right) \tag{17}$$

are the renormalized nuclear g factors. According to Eqs. (16) and (17), rotation effectively reduces the hyperfine field proportional to cosθ and qualitatively transforms hyperfine-structure spectra through the renormalization of nuclear g factors (17). In this case, changes in the effective $\tilde{g}$ factors for ground and excited nuclear states are different, because the original nuclear g factors are different. As a result, for the counterclockwise rotation corresponding to the positive constant K, the $\tilde{g}$-factor magnitude for the ground and excited states decreases and increases, respectively. For angles θ close to $\frac{\pi}{2}$, the $\tilde{g}$ factor for the nuclear ground state can even change sign. This circumstance is responsible for the fundamental rearrangement of spectra shown in Fig. 3. In particular, for the angle θ determined by the condition

$$\cos\theta = \frac{\omega_g}{2\Omega}, \tag{18}$$

the effective $\tilde{g}$ factor for the nuclear ground state vanishes, and four lines are observed in the spectrum of the hyperfine magnetic structure. Figure 4 shows the splitting scheme of nuclear energy levels and absorption spectrum for this case.

As the angle θ decreases, the fast-rotation effect on the shape of the hyperfine-structure spectrum weakens. However, the rotation effect is pronounced not only when spectra are of the nonstandard shape shown in Fig. 3 but also when corresponding line shifts are comparable with the line width Γ_0. For $\frac{\Omega_0}{2\pi}$ = 0.5 GHz corresponding to γ-Fe_2O_3 particles of a mean diameter of 7 nm and a characteristic magnetic-anisotropy energy $\frac{kV}{k_B}$ of about 1000 K [9], the rotation effect is estimated to be significant for angles θ > 30°.

We emphasize that spectra cannot be well approximated in the framework of standard static components with the introduction of the distribution of hyperfine fields and relaxation processes disregarding the above-revealed features of hyperfine structure spectra, even if these features are not manifested explicitly due to the superposition of various subspectra under real conditions.

REFERENCES

1. V. I. Gol'danskiĭ and E. F. Makarov, in *Chemical Applications of Mössbauer Spectroscopy* (Academic, New York, 1968).
2. A. M. Afanas'ev, S. S. Yakimov, V. M. Cherepanov, *et al.*, Zh. Éksp. Teor. Fiz. **89**, 182 (1985) [Sov. Phys. JETP **62**, 104 (1985)].
3. A. M. Afanas'ev, P. V. Hendriksen, and S. Mørup, Hyperfine Interact. **88**, 35 (1994).
4. A. M. Afanas'ev and M. A. Chuev, Pis'ma Zh. Éksp. Teor. Fiz. **74** (2), 112 (2001) [JETP Lett. **74**, 107 (2001)].
5. S. Mørup, J. Magn. Magn. Mater **37**, 39 (1983).
6. S. Mørup, Hyperfine Interact. **90**, 171 (1994).
7. I. P. Suzdalev, A. S. Plachinda, V. N. Buravtsev, *et al.*, Chem. Phys. Rep. **17** (7), 1355 (1998).
8. A. J. Hernando, J. Phys. B **11**, 9455 (1999).
9. E. Tronc, A. Ezzir, R. Cherkaoui, *et al.*, J. Magn. Magn. Mater. **221**, 63 (2000).
10. F. Bødker, M. F. Hansen, Ch. B. Koch, *et al.*, Phys. Rev. B **61**, 6826 (2000).
11. A. Abragam and B. Bleaney, *Electron Paramagnetic Resonance of Transition Ions* (Claredon, Oxford, 1970), Vol. 1.
12. A. M. Afanas'ev, M. A. Chuev, and Yu. Hesse, Zh. Éksp. Teor. Fiz. **113** (5), 1799 (1998) [JETP **86**, 983 (1998)].

Translated by R. Tyapaev

Doklady Physics, Vol. 48, No. 6, 2003, pp. 282–284. Translated from Doklady Akademii Nauk, Vol. 390, No. 6, 2003, pp. 755–757.

PHYSICS

Graviton Mass and the Total Relative Mass Density Ω_{tot} in the Universe

Corresponding Member of the RAS S. S. Gershteĭn*, Academician A. A. Logunov, and M. A. Mestvirishvili**

Received February 14, 2003

The experimental data for the angular spectrum of the cosmic microwave background make it possible to numerically determine a number of cosmological parameters [2], including the ratio $\Omega_{tot} = \frac{\rho_{tot}}{\rho_c}$ of the density ρ_{tot} of all types of matter to the critical density $\rho_c = \frac{3H_0^2}{8\pi G}$, where G is the gravitational constant and H_0 is the current Hubble constant [3]. Jaffe *et al.* [1] analyzed the last two experiments BOOMERANG-98 [4] and MAXIMA-1 [5] taking into account the previous experiment COBE DMR [6] and the data obtained from the observation of type-1a supernovae (SN1a) [7, 8] and large-scale structures of the universe [9]. The analysis [1] shows that the average Ω_{tot} value for the combination of various experiments systematically exceeds unity and

$$\Omega_{tot} = 1.11 \pm 0.07 \quad (68\% \text{ c.l.}). \tag{1}$$

This fact seems to be rather intriguing. Actually, according to the most popular theory of the inflationary expansion of the universe at an early stage of its evolution, Ω_{tot} must be equal to unity with a high accuracy (which provides a flat space geometry). For this reason, although

$$\Omega_{tot} = 1.11^{+0.13}_{-0.12} \quad (95\% \text{ c.l.}) \text{ [1]} \tag{2}$$

in a wider interval of experimental errors does not contradict the model of inflationary expansion, it is important that a fundamental consequence of the field relativistic theory of gravity (RTG) [10, 11], where the Euclidean character of the three-dimensional space follows from the equations of the gravitational field, is that the quantity Ω_{tot} must certainly exceed unity.

The RTG implies that the total energy–momentum tensor, which is conserved in the Minkowski space and involves the gravitational field, is a source of the gravitational field. In this sense, the RTG is similar to the current gauge theories of the electroweak interaction and quantum chromodynamics, where conserving currents are sources of vector fields. According to this approach, the gravitational field has to be described by the second-rank symmetric tensor $\varphi^{\mu\nu}$. Owing to this fact and since the gravitational field is universal, theory can be geometrized: the motion of matter under the action of the gravitational field in the Minkowski space looks as if it proceeds in the effective Riemann space with the metric-tensor density $\tilde{g}^{\mu\nu}$ specified by the equality

$$\tilde{g}^{\mu\nu} = \tilde{\gamma}^{\mu\nu} + \tilde{\varphi}^{\mu\nu}; \quad \tilde{g}^{\mu\nu} = \sqrt{-g}g^{\mu\nu}, \quad g = \det(\tilde{g}^{\mu\nu}) = \det(g_{\mu\nu}), \tag{3}$$

where $\tilde{\gamma}^{\mu\nu}$ and $\tilde{\varphi}^{\mu\nu}$ are the metric-tensor density and the gravitational-field density in the Minkowski space, respectively. It should be noted that this field approach necessarily requires a nonzero graviton mass m_g because, otherwise, the metric tensor of the Minkowski space disappears from the equations and only the Riemann space remains. The set of RTG equations for the gravitational field [10, 11] has the form

$$\left(R_\nu^\mu - \frac{1}{2}\delta_\nu^\mu R\right) + \frac{1}{2}\left(\frac{m_g c}{\hbar}\right)^2\left(\delta_\nu^\mu + g^{\mu\alpha}\gamma_{\alpha\nu} - \frac{1}{2}\delta_\nu^\mu g^{\alpha\beta}\gamma_{\alpha\beta}\right) = \frac{8\pi G}{c^2}T_\nu^\mu, \tag{4}$$

$$D_\mu \tilde{g}^{\mu\nu} = 0, \tag{5}$$

where R_ν^μ and R are the corresponding curvatures in the effective Riemann space, T_ν^μ is the energy–momentum tensor for matter in this space, and D_μ is the covariant derivative in the Minkowski space. Equations (4) and (5) are covariant under arbitrary transformations of coordinates, are form-invariant under the Lorentz trans-

Institute for High-Energy Physics, Protvino, Moscow oblast, 142284 Russia

* *e-mail: gershtein@mx.ihep.su*

** *e-mail: logunov@mx.ihep.su*

1028-3358/03/4806-0282$24.00 © 2003 MAIK “Nauka/Interperiodica”

formations, and correctly describe all gravitational effects observed in the solar system.

It is important that Eq. (5) in this scheme appears not as an additional condition but as a consequence of the gravitational-field equations and the conservation law of the total energy–momentum tensor.

Writing the interval in the effective Riemann space for the uniform and isotropic universe in the form

$$ds^2 = c^2U(t)dt^2 - V(t)\left[\frac{dr^2}{1-kr^2} + r^2(d\Theta^2 + \sin^2\Theta d\Phi^2)\right] \quad (6)$$

(where $k = 1, -1, 0$ for a closed, hyperbolic, and flat universe, respectively), we obtain from Eqs. (5)

$$\frac{\partial}{\partial t}\sqrt{\frac{V^3}{U}} = 0, \text{ i.e. } V = \beta U^{1/3}, \quad \beta = \text{const}, \quad (7)$$

$$\frac{\partial}{\partial r}[r^2(1-kr^2)^{1/2}] - 2r(1-kr^2)^{-1/2} = 0. \quad (8)$$

Equation (8) is valid only for $k = 0$. Thus, according to the RTG, the spatial geometry of the universe has to be flat at all stages of its evolution (independently of whether or not inflationary expansion took place).

Passing to the proper time $d\tau = U^{1/2}dt$ and denoting $a^2(\tau) = U^{1/3}$, we can write interval (6) as

$$ds^2 = c^2d\tau^2 - \beta a^2(\tau)[dr^2 + r^2(d\Theta^2 + \sin^2\Theta d\Phi^2)]. \quad (9)$$

For the scale factor $a(\tau)$, Eq. (4) takes the form

$$\left(\frac{1}{a}\frac{da}{a\tau}\right)^2 = \frac{8\pi G}{3}\rho - \frac{\omega}{a^6}\left(1 - \frac{3a^4}{\beta} + 2a^6\right), \quad \omega = \frac{1}{12}\left(\frac{m_g c^2}{\hbar}\right)^2, \quad (10)$$

$$\frac{1}{a}\frac{d^2a}{d\tau^2} = -\frac{4\pi G}{3}\left(\rho + \frac{3P}{c^2}\right) - 2\omega\left(1 - \frac{1}{a^6}\right). \quad (11)$$

The constant β in expressions (9) and (10) has a simple meaning. According to the causality principle, matter in the Minkowski space cannot move beyond the light cone in this space. Therefore, $a^4(\tau) \le \beta$; i.e., $\beta = a_{max}^4$.

Thus, according to the RTG, the universe cannot expand infinitely. Thereby, the currently observed accelerated expansion of the universe cannot be explained by assuming nonzero vacuum energy. This fact seems to be quite natural, because the vacuum energy density must identically vanish in the field interpretation of gravity in the Minkowski space. From the RTG viewpoint, the observed acceleration can be explained by assuming the existence of a special substance, or quintessence [12, 13], which is described by the equation of state

$$P = -(1-\nu)\rho_q \quad \left(0 < \nu < \frac{2}{3}\right), \quad (12)$$

and whose density decreases as $\rho_q \sim \frac{1}{a^{3\nu}}$. (This opportunity was pointed out by Kalashnikov [14].) It follows from Eq. (10) that the maximum expansion of the universe ($\frac{da}{d\tau} = 0$ and $a \gg 1$) is achieved for density $\rho_{min} = \frac{1}{16\pi G}\left(\frac{m_g c^2}{\hbar}\right)^2$. Equation (10) shows that the cosmological singularity is also eliminated according to the RTG. Indeed, since the left-hand side of the equation is positive definite, the matter-density growth as $\rho \sim \frac{1}{a^4}$ for $a \longrightarrow 0$ at the radiation-dominant stage must compensate the negative term on the right-hand side of the equation, which grows as $\frac{\omega}{a^6}$, for a certain minimum value $a_{min} \neq 0$.

Thus, the nonzero graviton mass in the RTG (eliminating both the cosmological singularity and the possibility of the infinite expansion of the universe) is responsible for the cyclic character of its evolution and ensures the flat geometry of the three-dimensional space at all stages of the evolution. However, $\Omega_{tot} > 1$ in this case. Indeed, writing Eq. (10) for the present time ($a \gg 1$) and dividing both sides by the Hubble constant H_0^2, we obtain

$$\Omega_{tot} = 1 + \frac{f^2}{6}, \quad f = \frac{m_g c^2}{\hbar H_0} = \frac{m_g}{m_H^0}, \quad (13)$$

where

$$m_H^0 = \frac{\hbar H_0}{c^2} = h \times 3.8 \times 10^{-66}\ \text{g} \simeq 2.7 \times 10^{-66}\ \text{g} \quad (h = 0.71) \quad (14)$$

can be called the "Hubble mass." From value (2) and formulas (13), it follows that $\frac{f^2}{6} \le 0.24$; i.e.,

$$m_g \le 1.2m_H^0 = 3.2 \times 10^{-66}\ \text{g} \quad (95\%\ \text{c.l.}). \quad (15)$$

Using values (1), we obtain $0.04 \le \frac{f^2}{6} \le 0.18$ and,

therefore, the graviton mass can be equal to

$$m_g = 2.2^{+0.6}_{-0.9} \times 10^{-66} \text{ g} \quad (66\% \text{ c.l.}). \qquad (16)$$

There is a question of whether the closeness of $m_g \simeq m_H^0$ is accidental or fundamental.

ACKNOWLEDGMENTS

We are grateful to V.A. Petrov, N.P. Tkachenko, and N.E. Tyurin for useful discussions. The work of one of us (S.S.G.) was supported by the Russian Foundation for Basic Research, project nos. 01-02-16585 and 00-15-96645.

Remark on proofreading. After this paper was sent for publication, there appeared the preliminary data of the WMAP experiment (arxiv.org/abs/astro-ph/0302207; February 12, 2003), where the value $\Omega_{tot} = 1.02 \pm 0.02$ was presented. These data provide more stringent restrictions on the graviton mass. At the 2σ $\frac{f^2}{6} \le 0.06$; i.e., $m_g \le 0.6 m_H^0 = 1.6 \times 10^{-66}$ g. At the same time, at the 1σ level, $\frac{f^2}{6} = 0.04$ is also admissible; i.e., $m_g = 1.3 \times 10^{-66}$ g in agreement with (16).

REFERENCES

1. A. H. Jaffe, P. A. R. Ade, A. Babbi, *et al.*, Phys. Rev. Lett. **86**, 3475 (2001).
2. G. Jungman, M. Kamionkowski, A. Kosowsky, *et al.*, Phys. Rev. D **54**, 1332 (1996).
3. J. R. Bond, G. Efstathiou, and M. Tegmark, Mon. Not. R. Astron. Soc. **291**, L33 (1997).
4. P. de Bernardis, P. A. R. Ade, J. J. Bock, *et al.*, Nature (London) **404**, 995 (2000).
5. S. Hanamy, P. Ade, A. Babbi, *et al.*, Astrophys. J. **545**, L5 (2000).
6. C. Bennet, A. Banday, K. M. Gorski, *et al.*, Astrophys. J. **464**, L1 (1996).
7. A. G. Riess, A. V. Filipenko, P. Challis, *et al.*, Astron. J. **116**, 1009 (1998).
8. S. Permutter, G. Aldering, G. Goldhaber, *et al.*, Astrophys. J. **517**, 565 (1999).
9. J. R. Bond and A. H. Jaffe, Philos. Trans. R. Soc. London **357**, 57 (1999); A. E. Lange *et al.*, astro-ph/0005004.
10. A. A. Logunov and M. A. Mestvirishvili, *Relativistic Theory of Gravity* (Nauka, Moscow, 1989), Sect. 11.
11. A. A. Logunov, *Theory of Gravitational Field* (Nauka, Moscow, 2001).
12. R. R. Caldwell, R. Dave, and P. J. Steinhardt, Phys. Rev. Lett. **80**, 1582 (1998).
13. J. P. Ostriker and P. J. Steinhardt, Sci. Am. **284** (1), 36 (2001).
14. V. L. Kalashnikov, gr-qc/0109060; gr-qc/0202084.

Translated by V. Bukhanov

Doklady Physics, Vol. 48, No. 6, 2003, pp. 285–289. Translated from Doklady Akademii Nauk, Vol. 390, No. 6, 2003, pp. 758–762.

PHYSICS

Statistical Physics of Dynamic Systems with Variable Memory

Ya. L. Kobelev*, L. Ya. Kobelev, and Yu. L. Klimontovich†*****

Presented by Academician N.A. Vatolin January 14, 2003

Received January 31, 2003

The master equations describing the dynamics of statistical systems are based on averaging of either the Liouville equation for the density distribution function for an N-particle system $D(x_1, \ldots, x_N, t)$, $x = \mathbf{r}, \mathbf{p}$ or the canonical equations for D in the form of classical Poisson brackets and the investigation of the equations for one-, two-, etc., particle distribution functions [Bogoliubov–Kirkwood–Green–Yvon method (see, e.g., [1]), Klimontovich method (see [2]), and Prigogine method (see [3])]. It was recently established that many-particle systems (aerosols, gels, macromolecules, anomalous diffusion, turbulence, partially ordered systems, electron–ion plasma, solids, etc.) have fractal and multifractal properties, whose explanation requires equations with fractional derivatives. Anomalous relaxation and anomalous diffusion (diffusion for which mean squared displacement of a particle is proportional to the time in a fractional power, i.e., $q\langle x\rangle q \sim t^{\beta}$, where β is a fractional number), which is observed in many systems and testifies to the presence of fractal properties in a system, were studied and theoretically described on the basis of fractal geometry in numerous works [4] (see also [2, 5] and references therein). In such a description, equations with Riemann–Liouville fractional derivatives with respect to time [6] and coordinates [5] or with respect to time and coordinates simultaneously [7] are used. The diffusion coefficient is assumed constant. Equations with fractional derivatives and constant fractional order describe non-Markov processes with fixed memory, i.e., systems whose state at a given time depends on the previous behavior of the system: temporal and coordinate memories. Systems with memory that were previously considered in thermodynamics and statistical physics (see [8] and reference therein) did not describe fractal structures and are not considered in this study. In particular, the systems mentioned above are systems with memory. However, memory (both temporal memory and memory on trajectories of a system) in certain physical systems can vary both in time and in coordinates. Available experimental data indicate that the fractal dimension of physical objects depends on both the parameters of the environment (temperature, pressure, etc., [9, 10]) and the internal parameters characterizing the system (elasticity, strength, etc., [11]). All the above examples show that the dynamics of statistical systems must be formulated on the basis of extension of the Liouville equation to fractal and multifractal media. It is interesting to investigate statistical and dynamic systems with fixed and variable memories. Dynamic processes in systems with time- and coordinate-dependent memory cannot be described in terms of Riemann–Liouville fractional derivatives that do not reproduce variations in memory. Therefore, it is necessary to use a new mathematical technique generalizing Riemann–Liouville fractional derivatives and integrals for the dynamics of multifractal objects with the fractal dimension depending on time and coordinates. Such a technique (considered in the following section) was proposed by one of us (L.Ya.K.) in [12]. In this study, the method of multiparticle distribution functions, which was introduced by Bogoliubov, Green, Kirkwood, and Yvon and developed by Klimontovich and Prigogine, is generalized to systems with fixed and variable memories. For this purpose, we use Riemann–Liouville fractional derivatives with a variable order of differentiation and integration. We derive the equations for multiparticle distribution functions in a statistical medium with variable memory and consider the case of small variable memory. For this case, we find fractal forces acting on the particles of the system in the presence of fractal-dimension gradients.

† Deceased.

* *Institute of Metal Physics, Ural Division, Russian Academy of Sciences, ul. S. Kovalevskoĭ 18, Yekaterinburg, 620219 Russia*
e-mail: yakov@imp.uran.ru

** *Ural State University, pr. Lenina 51, Yekaterinburg, 620083 Russia*
e-mail: leonid.kobelev@usu.ru

*** *Moscow State University, Vorob'evy gory, Moscow, 119899 Russia*

1028-3358/03/4806-0285$24.00

FRACTIONAL DERIVATIVES AND INTEGRALS WITH A VARIABLE ORDER OF DIFFERENTIATION AND INTEGRATION

To describe statistical non-Markov systems with fixed memory (in this case, the fractional order of derivatives and integrals is fixed), it is sufficient to use the well-known Riemann–Liouville fractional derivatives and integrals [13, 14]. However, to construct statistical physics for a medium with a multifractal dimension depending on time and coordinates (or in a physical system with such fractal properties), it is insufficient to use only Riemann–Liouville fractional derivatives. In this case, fractional derivatives and integrals with a variable order (generalized Riemann–Liouville fractional derivatives (GFDs), which were introduced by one of us in [12]) should be used. These derivatives are defined by the relationships (we give the definitions for left derivatives; more detailed information is available in [12])

$$\frac{\partial^{1+\varepsilon_t}}{\partial t^{1+\varepsilon_t}} f \equiv D_{+,t}^{d_t} f(t)$$

$$= \frac{d^n}{dt^n}\int_a^t dt' \frac{f(t')}{\Gamma(n-d_t(t'))(t-t')^{d_t(t')-n+1}}, \qquad (1)$$

$$\frac{\partial^{1+\varepsilon_x}}{\partial x^{1+\varepsilon_t}} f \equiv D_{+,x}^{d_x} f(x)$$

$$= \frac{d^n}{dx^n}\int_a^x dx' \frac{f(x')}{\Gamma(n-d_x(x'))(x-x')^{d_x(x')-n+1}},$$

where Γ is the Euler gamma function; $n = \{d\} + 1$, where $\{d\}$ is the integer part of d if $d \geq 0$ [i.e., $(n-1) \leq d < n$]; $n = 0$ if $d < 0$; $d_t = 1 + \varepsilon(t)$; and $d_x = 1 + \varepsilon(x)$. For d = const, definitions (3) coincide with Riemann–Liouville derivatives. For $|\varepsilon| \ll 1$, the integral operators defined above for the fractional exponents d_t and d_x depending on time and coordinates can be represented in terms of ordinary derivatives and integrals [12] for $|\varepsilon| \ll 1$. In this case, generalized fractional derivatives satisfy the approximate relationships (we give only the relationships for derivatives)

$$D^{1+\varepsilon_t} f(x,t) = (1+\varepsilon_t)\frac{\partial}{\partial t} f(x,t) + \frac{\partial \varepsilon_t}{\partial t} f(x,t),$$
$$D^{1+\varepsilon_x} f(x,t) = (1+\varepsilon_x)\frac{\partial}{\partial x} f(x,t) + \frac{\partial \varepsilon_x}{\partial x} f(x,t). \qquad (2)$$

These relationships make it possible to describe the dynamics of the system including the effect of changes in the fractal dimension (if they are much smaller than unity) in terms of ordinary differential and integral equations. To determine the fractal dimension d_α, the equations corresponding to the problems under consideration were derived in [12].

MULTIPARTICLE DISTRIBUTION FUNCTIONS AND EQUATIONS FOR A DISTRIBUTION FUNCTION IN SPACE WITH FIXED AND VARIABLE MEMORIES

Although the theory of multiparticle distribution functions in statistical physics is well known [1, 2], we briefly outline it to clearly reveal the generalizations necessary for the inclusion of fixed and variable memories, as well as to introduce the notation used in the following. The Bogoliubov–Kirkwood–Green–Yvon model is characterized by the following equations for s-particle distribution functions in the N-dimensional phase space of coordinates and momenta x ($x = \mathbf{q}, \mathbf{p}$) after passage to the limit $N = \infty$, $V = \infty$, and $NV^{-1} = v$ = const:

$$\frac{\partial F_s}{\partial t} = [H_s; F_s] + \frac{1}{v}\int_Q \sum_{1 \leq i \leq s} \Phi(|q_i - q_j|); F_{s+1}]dx_{s+1}. \qquad (3)$$

Here, the square brackets denote classical Poisson brackets;

$$H_s = H_s(x_1, \ldots, x_s)$$
$$= \sum_{1 \leq i \leq s} T(p_i) + \sum_{1 \leq i < j \leq s} \Phi(|q_i - q_j|), \quad v = \frac{V}{N}, \qquad (4)$$

where $T(\mathbf{p}_i)$ is the kinetic energy of the ith particle and $\Phi(|q_i - q_j|)$ is the interaction energy between particles;

$$F_s(t, x_1, \ldots, x_s)$$
$$= V^s \int_{\Omega_V} \ldots \int_{\Omega_V} D(x_1, \ldots, x_N, t)dx_{s+1}\ldots dx_N, \qquad (5)$$

$$\frac{\partial D}{\partial t} = \sum_{1 \leq i \leq N} [H(x_i); D] + \sum_{1 \leq i < j \leq N} [\Phi(|q_i - q_j|); D], \qquad (6)$$

where the probability density $D(x_1, \ldots, x_N, t)$ that all N particles have the coordinates $x_1, \ldots, x_N$ at the time t satisfies the normalization condition

$$\int_Q D(x_1, \ldots, x_N, t)dx_1\ldots dx_N = 1. \qquad (7)$$

The above equations completely describe the behavior of a dynamic statistical system in space and time with topological dimensions. In order to apply them to sta-

tistical processes in systems with memory, all derivatives and integrals in Eqs. (1)–(6) should be replaced by fractional derivatives and integrals defined by Eq. (3). In this case, we have

$$\frac{\partial^{d_t(x,t)}F_s}{\partial t^{d_t(x,t)}} = [H_s; F_s] + \frac{1}{v}\int_Q \frac{\left[\sum_{1\le i\le s}\Phi(|q_i - q_j|); F_{s+1}\right]dx_{s+1}}{\Gamma(d_{x_{s+1}}(x_{s+1},t))(x-x_{s+1})^{-d_{x_{s+1}}(x_{s+1},t)-n+1}}, \tag{8}$$

$$F_s(x_1,\ldots,x_s) = \int_Q \frac{dx_{s+1}}{\Gamma(d(x_{s+1},t))(x-x_{s+1})^{-d_{x_{s+1}}(x_{s+1},t)-n+1}}\ldots Dd_{x_{s+2}}\ldots d_{x_N}, \tag{9}$$

$$\frac{\partial^{d_t}D}{\partial t^{d_t}} = \sum_{1\le i\le N}[H_s; D] + \sum_{1\le i<j\le N}[\Phi(|q_i - q_j|); D], \tag{10}$$

$$\int_Q \frac{d_{x_1}}{\Gamma(d_{x_1})(x-x_1)^{-d_{x_1}+1}}\ldots D(x_1,\ldots,x_N,t),dx_2\ldots dx_N = 1. \tag{11}$$

In the Poisson brackets appearing in Eq. (10), all derivatives are replaced by GFDs and, after passage to the limit $Q = \infty$, all x's without indices are taken to be ∞ and the lower limits in the integrals, $a = -\infty$. Equations (8)–(11) completely describe the statistical properties of dynamic systems with both fixed (d = const) and variable memories.

EQUATIONS FOR DETERMINING FRACTAL DIMENSIONS

The fractal dimension $d(x, t)$ depends on the energy density at a given point and meets the equation (this equation was first derived in [12] by using the variational method for the minimum of the fractal dimension considered as an order parameter):

$$a\frac{\partial d(x,t)}{\partial t} = \frac{\partial}{\partial L}\left[D_{\text{diff}}(L,x,t)\frac{\partial D(x,t)}{\partial L}\right] - (a-L)d(x,t) + ad(x,t)^2, \tag{12}$$

where L is the Lagrangian density, a is the L-independent quantity of the energy-density dimension, and D_{diff} is the diffusion coefficient of the fractal dimension in the energy space. For $d = 1 + \varepsilon(x, t)$, where $|\varepsilon| \ll 1$ (in this study, we will consider only this case), neglecting the diffusion of the fractal dimension in the space L, we find the time-independent fractal dimension in the form

$$d(x) \approx 1 - \frac{L(x)}{a}, \quad a = kT. \tag{13}$$

In the simplest case of the time-dependent fractal dimension, d has the form of Eq. (13), where L is replaced by $\int_0^t L(x(t')\omega(t'))dt'$ with the correlation function $\omega(t')$ between energy at various times. For $\omega(t) = \delta(t - t')$, it is only necessary to take into account time functions in L.

VLASOV AND KLIMONTOVICH EQUATIONS FOR SYSTEMS WITH VARIABLE MEMORY

The equation that relates one- and two-particle distribution functions is of most interest. For systems with variable memory, this equation has the form

$$\frac{\partial^{d_t(x,t)}}{\partial t^{d_t(x,t)}} = [H_t; F_t] + \frac{1}{v}\int_Q \frac{\left[\sum_{1\le i\le s}\Phi(|q_i - q_j|); F_2\right]}{\Gamma(d(x_2,t))(x-x_2)^{-d(x_2,t)+1}}dx_2 = 0. \tag{14}$$

For $d = 1$, this equation takes the form

$$\frac{\partial}{\partial t}F_1(\mathbf{q}, \mathbf{p}) - \frac{\mathbf{p}}{m}\frac{\partial}{\partial \mathbf{q}}F_1(\mathbf{q}, \mathbf{p}) - \int \frac{\Phi(|\mathbf{q} - \mathbf{q}_1|)}{\partial \mathbf{q}}F_1(\mathbf{q}_1)d\mathbf{q}_1\frac{\partial}{\partial \mathbf{p}}F_1(\mathbf{q}, \mathbf{p}) = 0, \quad (15)$$

where m is the mass of a particle and $F_1(\mathbf{q}) = \int F_1(\mathbf{q}, \mathbf{p})d\mathbf{p}$, and coincides with the Vlasov equation. For $d \neq 1$, we obtain the equation

$$\frac{\partial^{d_t}}{\partial t^{d_t}}F_1(\mathbf{q}, \mathbf{p}) - \frac{\mathbf{p}}{m}\frac{\partial^{d_\mathbf{q}}}{\partial \mathbf{q}^{d_\mathbf{q}}}F_1(\mathbf{q}, \mathbf{p}) - \int \frac{\partial^{d_\mathbf{q}}\Phi(|\mathbf{q} - \mathbf{q}_1|)}{\partial \mathbf{q}^{d_\mathbf{q}}} \times \frac{F_1(\mathbf{q}_1)}{\Gamma(d_\mathbf{q}(\mathbf{q}_1))(\mathbf{q} - \mathbf{q}_1)^{-d_q(\mathbf{q}_1)+1}} \times d\mathbf{q}_1\frac{\partial^{d_\mathbf{p}}}{\partial \mathbf{p}^{d_\mathbf{p}}}F_1(\mathbf{q}, \mathbf{p}) = 0. \quad (16)$$

What are the differences between Eq. (16) and the Vlasov equation? First, Eq. (16) involves terms proportional to F_1 that lead to a change in energy. Second, the generalized velocity and the mean force acting on a particle change as

$$\mathbf{p}m^{-1} \to \mathbf{p}m^{-1}(1 + \varepsilon_\mathbf{q})$$

and

$$F_{sr} \to m^{-1}\int \frac{\partial[(1 + \varepsilon_\mathbf{q})\Phi]}{\partial \mathbf{q}}F_1(\mathbf{q}_1)d\mathbf{q}_1(1 + \varepsilon_\mathbf{p}),$$

respectively. These changes can considerably modify the spectrum of elementary excitations of the system (even for small fractal corrections proportional to ε) and probably provide new stability conditions for the electron–ion plasma with fractal structures (see [15]).

Now we consider the Klimontovich equation in the fractal space. Unlike the Fokker–Planck equation, the Klimontovich equation takes into account diffusion in both the momentum and coordinate spaces (its solution for d = const was considered in [15]). For systems with variable memory, it has the form

$$\frac{\partial^{d_t}}{\partial t^{d_t}}F_1(\mathbf{q}, \mathbf{p}) - \frac{\mathbf{p}}{m}\frac{\partial^{d_\mathbf{q}}}{\partial \mathbf{q}^{d_\mathbf{q}}}F_1(\mathbf{q}, \mathbf{p}) - \int \frac{\partial^{d_\mathbf{q}}\Phi(|\mathbf{q} - \mathbf{q}_1|)}{\partial \mathbf{q}^{d_\mathbf{q}}}F_1(\mathbf{q}_1)d\mathbf{q}_1\frac{\partial^{d_\mathbf{p}}}{\partial \mathbf{p}^{d_\mathbf{p}}}F_1(\mathbf{q}, \mathbf{p}) = \frac{\partial^{d_\mathbf{p}}}{\partial \mathbf{p}^{d_\mathbf{p}}}\left[D_p(\mathbf{p})\frac{\partial^{d_\mathbf{p}}}{\partial \mathbf{p}^{d_\mathbf{p}}}F_1(\mathbf{q}, \mathbf{p})\right] + \frac{\partial^{d_\mathbf{q}}}{\partial \mathbf{q}^{d_\mathbf{q}}}\left[D_q(\mathbf{q})\frac{\partial^{d_\mathbf{q}}}{\partial \mathbf{q}^{d_\mathbf{q}}}F_1(\mathbf{q}, \mathbf{p})\right], \quad (17)$$

where the $\frac{\partial^{d_\mathbf{q}}}{\partial^{d_\mathbf{q}}}\left[D\frac{\partial^{d_\mathbf{q}}}{\partial^{d_\mathbf{q}}}F_1\right]$ terms on the right-hand side are the products of right fractional derivatives by left fractional derivatives.

EQUATION FOR THE ONE-PARTICLE DISTRIBUTION FUNCTION. THE CASE OF WEAK VARIABLE MEMORY

To describe systems with weak variable memory ($|\varepsilon| \ll 1$), relationships similar to Eq. (2) should be used. In this case, GFDs are represented in terms of ordinary derivatives and integrals according to the following rules (when ε^2 terms are ignored):

$$\int \ldots dx \to \int (1 - \varepsilon_x)\ldots dx, \quad \frac{\partial}{\partial y}F \to \frac{\partial}{\partial y}[(1 + \varepsilon_y)f], \quad y = x, t. \quad (18)$$

In the approximation of the Vlasov master equation, Eq. (17) takes the form

$$(1 + \varepsilon_t(x, t))\frac{\partial}{\partial t}F_1(\mathbf{q}, \mathbf{p}, t) + \frac{\partial \varepsilon}{\partial t}F_1(\mathbf{q}, \mathbf{p}, t) - \frac{\mathbf{p}}{m}\left[(1 + \varepsilon_\mathbf{q}(x, t))\frac{\partial}{\partial \mathbf{q}}F_1(\mathbf{q}, \mathbf{p}, t) + \frac{\partial \varepsilon_\mathbf{q}(x, t)}{\partial \mathbf{q}}F_1(\mathbf{q}, \mathbf{p}, t)\right] - \int \frac{\partial \Phi(|\mathbf{q} - \mathbf{q}_1|)}{\partial \mathbf{q}}F_1(\mathbf{q}_1)d\mathbf{q}_1\left[(1 + \varepsilon_\mathbf{p})\frac{\partial}{\partial \mathbf{p}}F_1(\mathbf{q}, \mathbf{p}, t) + \frac{\partial \varepsilon_\mathbf{p}(x, t)}{\partial \mathbf{p}}F_1(\mathbf{q}, \mathbf{p}, t)\right] = 0. \quad (19)$$

In the approximation of the Klimontovich master equation, using Eq. (18), we find

$$(1+\varepsilon_t(x,t))\frac{\partial}{\partial t}F_1(\mathbf{q},\mathbf{p},t)+\frac{\partial\varepsilon}{\partial t}F_1(\mathbf{q},\mathbf{p},t)-\frac{\mathbf{p}}{m}\left[(1+\varepsilon_{\mathbf{q}}(x,t))\frac{\partial}{\partial\mathbf{q}}F_1(\mathbf{q},\mathbf{p},t)+\frac{\partial\varepsilon_{\mathbf{q}}(x,t)}{\partial\mathbf{q}}F_1(\mathbf{q},\mathbf{p},t)\right]$$
$$-\int\frac{\partial\Phi(|\mathbf{q}-\mathbf{q}_1|)}{\partial\mathbf{q}}F_1(\mathbf{q}_1)d\mathbf{q}_1\left[(1+\varepsilon_{\mathbf{p}})\frac{\partial}{\partial\mathbf{p}}F_1(\mathbf{q},\mathbf{p},t)+\frac{\partial\varepsilon_{\mathbf{p}}(x,t)}{\partial\mathbf{p}}F_1(\mathbf{q},\mathbf{p},t)\right]$$
$$=(1+\varepsilon_{\mathbf{p}})\frac{\partial}{\partial\mathbf{p}}\left[D_p\frac{\partial^{1+\varepsilon_{\mathbf{p}}}}{\partial\mathbf{p}^{1+\varepsilon_{\mathbf{p}}}}F_1(\mathbf{q},\mathbf{p},t)\right]+\frac{\partial\varepsilon_{\mathbf{p}}}{\partial\mathbf{p}}\left[D_p\frac{\partial^{1+\varepsilon_{\mathbf{p}}}}{\partial\mathbf{p}^{1+\varepsilon_{\mathbf{p}}}}F_1(\mathbf{q},\mathbf{p},t)\right]$$
$$+(1+\varepsilon_{\mathbf{q}})\frac{\partial}{\partial\mathbf{q}}\left[D_q\frac{\partial^{1+\varepsilon_{\mathbf{q}}}}{\partial\mathbf{q}^{1+\varepsilon_{\mathbf{q}}}}F_1(\mathbf{q},\mathbf{p},t)\right]+\frac{\partial\varepsilon_{\mathbf{q}}}{\partial\mathbf{q}}\left[D_q\frac{\partial^{1+\varepsilon_{\mathbf{q}}}}{\partial\mathbf{q}^{1+\varepsilon_{\mathbf{q}}}}F_1(\mathbf{q},\mathbf{p},t)\right],\qquad(20)$$

where

$$\frac{\partial^{1+\varepsilon_{\mathbf{x}}}}{\partial\mathbf{x}^{1+\varepsilon_{\mathbf{x}}}}F_1=\frac{\partial}{\partial\mathbf{x}}[(1+\varepsilon_{\mathbf{x}})F_1],\quad\mathbf{x}=\mathbf{q},\mathbf{p}.\qquad(21)$$

When ordinary derivatives in the diffusion terms of the Klimontovich equation are replaced by GFDs, new forces of two types appear. They are proportional to the gradients of the fractal dimension ε in momenta and coordinates (in the latter case, similar forces were obtained in [15]). In addition, terms proportional to F_1 appear (as in the fractal Vlasov equation).

CONCLUSIONS

Thus, the main equations of statistical physics of fractal dynamic systems with variable memory (i.e., systems with variable fractal dimension) were presented. New forces proportional to the gradients of fractal dimension in coordinates and momenta were found. The resulting equations can be widely applied in condensed-matter physics, biophysics, economic sciences, etc., when variable fractal memory (temporal or spatial) is a significant factor (see also [15]).

ACKNOWLEDGMENTS

This work was supported in part by INTAS (grant no. 00-0847), the Russian Foundation for Basic Research (project no. 00-02-16285), and the US Civilian Research and Development Foundation for the Independent States of the Former Soviet Union (grant no. REC-005).

REFERENCES

1. N. N. Bogolyubov, *Dynamic Problems in Statistical Physics* (OGIZ, Moscow, 1946).
2. Yu. L. Klimontovich, *Statistical Physics of Open Systems* (Yanus, Moscow, 1995/1999/2001; Kluwer, Dordrecht, 1995/1999/2001), Vols. 1, 2, 3.
3. I. G. Prigogine, *The End of Certainty* (Free Press, New York, 1997).
4. B. Mandelbrot, *The Fractal Geometry of Nature* (Freeman, New York, 1982).
5. A. V. Chechkin, R. Gorenflo, and I. M. Sokolov, Phys. Rev. E **66**, 046129 (2002).
6. W. G. Gloecke and T. F. Nonnenmacher, J. Stat. Phys. **71** (34), 741 (1993).
7. V. L. Kobelev, E. P. Romanov, L. Ya. Kobelev, and Ya. L. Kobelev, Dokl. Akad. Nauk **361**, 755 (1998) [Dokl. Phys. **43**, 487 (1998)].
8. W. Day, *Thermodynamics of Simple Materials with Fading Memory* (Springer-Verlag, Berlin, 1972; Mir, Moscow, 1974).
9. V. Ya. Shur, S. A. Negashev, *et al.*, Ferroelectrics **169**, 63 (1995).
10. P. V. Korolev and S. N. Kul'kov, Perspekt. Mater., No. 3, 21 (1997).
11. V. S. Ivanova, A. S. Balankin, I. Zh. Bunin, and A. A. Oksogoev, *Synergetics and Fractals in Materials Science* (Nauka, Moscow, 1994).
12. L. Ya. Kobelev, *Fractal Theory of Time and Space*, Available from VINITI, No. 2677-B99 (Moscow, 1999).
13. S. G. Samko, A. A. Kilbas, and O. I. Marichev, *Fractional Integrals and Derivatives, Theory and Applications* (Nauka i Tekhnika, Minsk, 1987; Gordon and Breach, Amsterdam, 1993).
14. I. M. Gelfand and G. E. Shilov, *Generalized Functions* (Academic, New York, 1964).
15. Ya. L. Kobelev, L. Ya. Kobelev, and Yu. L. Klimontovich, Dokl. Akad. Nauk **390** (5) (1993) (in press).

Translated by Yu. Vishnyakov

Doklady Physics, Vol. 48, No. 6, 2003, pp. 290–295. Translated from Doklady Akademii Nauk, Vol. 390, No. 6, 2003, pp. 763–768.

PHYSICS

Order–Disorder Processes in Crystals When Crystallizing Binary Metallic Melts

Academician P. D. Sarkissov, Yu. A. Baĭkov, and V. P. Meshalkin*

Received November 14, 2002

INTRODUCTION

Theoretical grounds of order–disorder processes in crystals with a simple cubic lattice when crystallizing stoichiometric binary metallic melts were studied in [1–5]. These works presented mathematical models of the growth of binary crystals that accompanies the solidification of corresponding metallic melts. These models are based on time-independent master equations describing the structure and growth kinetics of binary metallic crystalline phases. It is noteworthy that, at significant supercooling of the melt–crystal system, there is a point where a disordered crystalline phase is formed at temperatures lower than the corresponding Curie temperature for the binary alloys in question. The above order–disorder effect is studied in connection with the fluctuation crystal-growth theory, where the model of the so-called two-phase transition (TPT) zone was used [6, 7]. The TPT zone separates two contiguous massive areas—a crystalline phase and the binary melt (see Fig. 1). In this model, the probability distribution functions of so-called growth monomers in TPT-zone layers were introduced and studied (see [2–5]). In the model of the concentration image of the TPT zone, these monomers are the analogues of liquid and solid metallic particles within the layers of the real TPT zone or the melt–crystal interface (see Fig. 2). As was noted in [2–5], the topological structure of the concentration image of the TPT zone affects the disordering process: the long-range order parameter η tends to zero in a way different from that for the Bragg–Williams thermodynamic order–disorder transition.

1. DISORDERING OF QUASI-STOICHIOMETRIC BINARY ALLOYS WITH THE SIMPLE CUBIC LATTICE

We consider here only stoichiometric metallic alloys with the simple cubic lattice when the number of particular-type atoms is approximately equal to the number of sites designed for them in the lattice. As was noted in [1–5], at large supercooling of 50%-alloy melts, the disordering temperature T_k for binary crystals can in principle lie within a certain temperature range below the so-called Curie point T_C. As was established in [8], when the distribution coefficients of both components are approximately equal to each other, i.e., $k_A^i = k_B^i$, where $i = 1, 2, \ldots, n$ marks TPT-zone layers (see Fig. 2), a crystalline quasi-stoichiometric binary phase can be formed for arbitrary fluctuations in the concentrations of solid-state particles.

The general composition structure of growth monomers in all layers of the concentration image of the TPT zone near the sharp interface of the binary melt–crystal system can be described by a closed system of six time-independent master equations in six unknowns $X_{\alpha\beta}^{(k)}(0)$ (α, β = A, B) (k = 1, 2), λ and η_1 (see [2–5]). Here, $X_{\alpha\beta}^{(k)}(0)$ are the probability distribution functions of

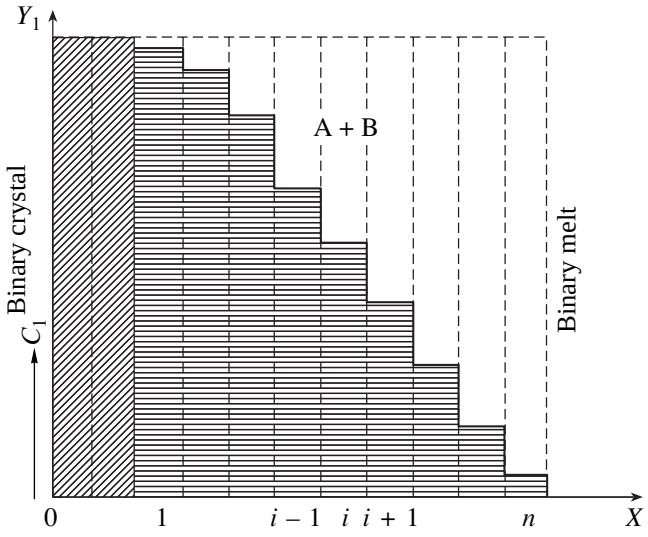

Fig. 1. Concentration image of the TPT zone for A + B binary systems. The shaded part of the column–layers for $i = 1, \ldots, n$ is the concentration C_1 of solid-state particles, and the unshaded part is the concentration $C_2 = 1 - C_1$ of liquid-state particles.

Mendeleyev University of Chemical Technology, Miusskaya pl. 9, Moscow, 125190 Russia

** e-mail: clogist@muctr.edu.ru*

1028-3358/03/4806-0290$24.00

αN^{-1} and βN^{-1} growth monomers in each layer of the TPT zone at the sharp interface of the melt–crystal system, i.e., at the zero-height fractures (see Fig. 2). Here, N is the total number of atoms of all kinds and states in each layer of the TPT zone, k marks a sublattice type to which the given αN^{-1} monomer belongs, α and β mark a particular particle type, and $\lambda \sim 1$ is the so-called roughness parameter of the given interface. Further, $\eta_1 = |(m-1)\ln q|$, where $q = \exp\left[-\frac{\varepsilon_{AA}}{T}\right]$, m appears in the relation $\varepsilon_{AB} = m\xi_{AA}$ and is usually equal to 2 for metals, and ε_{AA} and ε_{AB} are opposite to the energies of interaction between the nearest A–A and A–B particles, respectively. As was noted in [2–5, 8], near the disordering temperature T_k, i.e., at $q = q_k$, the above closed system of six independent equations with six unknowns can be replaced by a linearized system of six homogeneous equations with the six unknowns

$$\Delta x_1 = X^1_{AA}(0) - X^0_{AA}(0), \quad \Delta x_2 = X^1_{AB}(0) - X^0_{AB}(0),$$
$$\Delta x_3 = X^1_{BA}(0) - X^0_{AB}(0), \quad \Delta x_4 = X^1_{BB}(0) - X^0_{AA}(0),$$
$$\Delta x_5 = \lambda - \lambda^0,$$

and $\tilde{\eta}_1$. Here, all functions $X^1_{\alpha\beta}(0)$ and λ depend on q and η, and the functions $X^1_{\alpha\beta}(0)$ and λ^0 are taken in the completely disordered phase, i.e., at $\eta = 0$. Thus, all $X^1_{\alpha\beta}(0)$ (α, β = A, B) specify the distribution of growth monomers near the sharp interface of the binary melt–crystal system in the completely disordered state. This linearized system has the form

$$\begin{gathered}
\alpha_{11}\Delta x_1 + \alpha_{13}\Delta x_3 + \alpha_{14}\Delta x_4 + \alpha_{15}\Delta x_5 + \alpha_{16}\eta_1 = 0,\\
\alpha_{14}\Delta x_1 + \alpha_{13}\Delta x_2 + \alpha_{11}\Delta x_4 + \alpha_{15}\Delta x_5 - \alpha_{16}\eta_1 = 0,\\
\alpha_{31}\Delta x_1 + \alpha_{32}\Delta x_2 + \alpha_{33}\Delta x_3 + \alpha_{34}\Delta x_4\\
+ \alpha_{35}\Delta x_5 + \alpha_{36}\eta_1 = 0,\\
\alpha_{34}\Delta x_1 + \alpha_{33}\Delta x_2 + \alpha_{32}\Delta x_3 + \alpha_{31}\Delta x_4\\
+ \alpha_{35}\Delta x_5 - \alpha_{36}\eta_1 = 0,\\
\alpha_{51}\Delta x_1 + \alpha_{53}\Delta x_3 + \alpha_{54}\Delta x_4 + \alpha_{55}\Delta x_5 + \alpha_{56}\eta_1 = 0,\\
\alpha_{54}\Delta x_1 + \alpha_{53}\Delta x_2 + \alpha_{51}\Delta x_4 + \alpha_{55}\Delta x_5 - \alpha_{56}\eta_1 = 0.
\end{gathered} \tag{1.1}$$

Here, coefficients α_{ij} ($i = 1, 2, 3$; $j = 1, \ldots, 6$) are functions of q, m, N, λ^0, and $R = \frac{\omega_+}{\nu}$, where the transition frequency ω_+ of growth monomers from the binary melt to the crystalline phase in a single layer is supposed to be identical for all layers of the TPT zone and ν is the oscillation frequency of a particle near the site in the real crystalline phase. System (1.1) was obtained by taking into account the symmetry properties of the above system of time-independent master equations under the $\eta \longrightarrow -\eta$ transformation, when the first, third, and fifth equations are transformed to the second, fourth, and sixth ones, respectively, and vice versa; i.e., the whole system is invariant under this transformation. Moreover, under the $\eta \longrightarrow -\eta$ transformation, $\Delta x_1 \rightleftharpoons \Delta x_4$, $\Delta x_2 \rightleftharpoons \Delta x_3$, and $\Delta x_5 = \text{inv}$ due to the following symmetry properties of the functions in question:

$$\begin{gathered}
X^1_{AA}(0)[-\eta] = X^1_{BB}(0)[\eta],\\
X^1_{AA}(0)[\eta] = X^1_{BB}(0)[-\eta],\\
X^1_{AB}(0)[-\eta] = X^1_{BA}(0)[\eta],\\
X^1_{BA}(0)[-\eta] = X^1_{AB}(0)[\eta],\\
\lambda(-\eta) = \lambda(\eta).
\end{gathered} \tag{1.2}$$

These properties follow from equivalence between A and B atoms and between 1 and 2 sublattices in stoichiometric binary alloys with the simple cubic lattice. Hence, Δx_i ($i = 1, \ldots, 5$) near the disordering tempera-

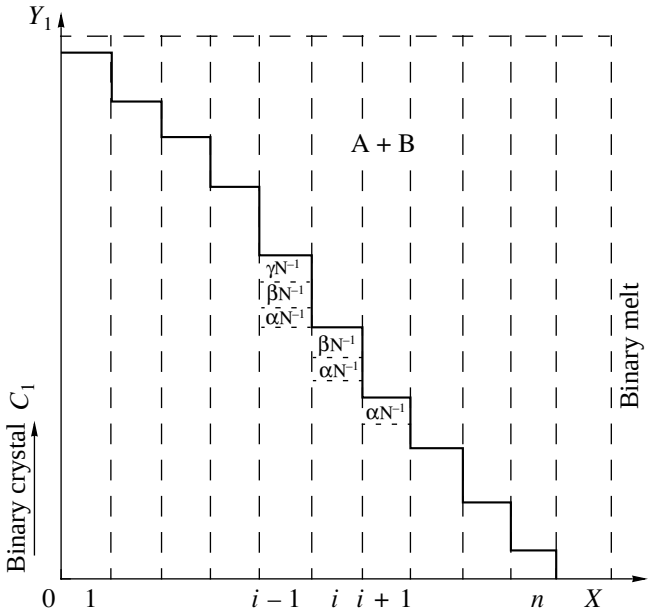

Fig. 2. Concentration image of the TPT zone consisting of n atomic layers, where layer nos. $i-1$; i; and $i+1$ end with the so-called growth monomers αN^{-1}, βN^{-1}, γN^{-1}; αN^{-1}, βN^{-1}; and αN^{-1}, respectively. The abscissa and ordinate axes are the layer number and the concentration of solid-state particles, respectively.

ture T_k can be expanded in the small parameter η up to $\sim\eta^3$ terms, i.e.,

$$\Delta x_1 \simeq a_1\eta + b_1\eta^2 + c_1\eta^3, \quad \Delta x_2 \simeq a_2\eta + b_2\eta^2 + c_2\eta^3,$$
$$\Delta x_4 \simeq -a_1\eta + b_1\eta^2 - c_1\eta^3, \tag{1.3}$$
$$\Delta x_3 \simeq -a_2\eta + b_2\eta^2 - c_2\eta^3, \quad \Delta x_5 \simeq b_3\eta^2,$$

where a_1, b_1, c_1, a_2, b_2, c_2, and b_3 are undefined constants depending on the properties of the system under consideration. The system of homogeneous equations (1.1) linear in small parameters Δx_i ($i = 1, \ldots, 5$) and η_1 has a nontrivial solution under the condition

$$\det = \|\alpha_{ij}\| = \begin{vmatrix} \alpha_{11} & 0 & \alpha_{13} & \alpha_{14} & \alpha_{15} & \alpha_{16} \\ \alpha_{14} & \alpha_{13} & 0 & \alpha_{11} & \alpha_{15} & -\alpha_{16} \\ \alpha_{31} & \alpha_{32} & \alpha_{33} & \alpha_{34} & \alpha_{35} & \alpha_{36} \\ \alpha_{34} & \alpha_{33} & \alpha_{32} & \alpha_{31} & \alpha_{35} & -\alpha_{36} \\ \alpha_{51} & 0 & \alpha_{53} & \alpha_{54} & \alpha_{55} & \alpha_{56} \\ \alpha_{54} & \alpha_{53} & 0 & \alpha_{51} & \alpha_{55} & -\alpha_{56} \end{vmatrix} = 2I \cdot \det = 0, \tag{1.4}$$

where

$$I = \begin{vmatrix} (\alpha_{11} + \alpha_{14}) & \alpha_{13} & \alpha_{15} \\ (\alpha_{31} + \alpha_{34}) & (\alpha_{32} + \alpha_{33}) & \alpha_{35} \\ (\alpha_{51} + \alpha_{54}) & \alpha_{53} & \alpha_{55} \end{vmatrix},$$

$$\det = (\alpha_{14} - \alpha_{11})[\alpha_{36}\alpha_{53} + \alpha_{56}(\alpha_{32} - \alpha_{33})] + (\alpha_{31} - \alpha_{34})(\alpha_{16}\alpha_{53} - \alpha_{13}\alpha_{56}) + (\alpha_{51} - \alpha_{54})[\alpha_{13}\alpha_{36} + \alpha_{16}(\alpha_{32} - \alpha_{33})].$$

Expanding the functions $X^1_{\alpha\beta}(0)[q, \eta]$ ($\alpha, \beta = A, B$), $\lambda(q, \eta)$, which appear in the system of six time-independent master equations presented in [2–4], in the small parameter η up to $\sim\eta^3$ terms and taking into account the symmetry and invariance of Eqs. (1.2) and (1.3), we arrive at a system of three homogeneous equations in the long-range order parameter η. In each of these equations, all η^2 terms disappear, because $\Delta x_1 \rightleftharpoons \Delta x_4$, $\Delta x_2 \rightleftharpoons \Delta x_3$, and $\lambda(-\eta) = \lambda(\eta)$ under the $\eta \longrightarrow -\eta$ transformation. Thus, instead of system (1.1), we obtain the system

$$A_1\eta + K_1\eta^3 = 0, \quad A_2\eta + K_2\eta^3 = 0, \quad A_3\eta + K_3\eta^3 = 0.$$

Here,

$$A_1 = (\alpha_{11} - \alpha_{14})a_1^p - \alpha_{13}\alpha_2^p + \alpha_{16},$$
$$A_2 = (\alpha_{31} - \alpha_{34})\alpha_1^p + (\alpha_{32} - \alpha_{33})\alpha_2^p + \alpha_{36}, \tag{1.5}$$
$$A_3 = (\alpha_{51} - \alpha_{54})\alpha_1^p - \alpha_{53}\alpha_2^p + \alpha_{56},$$

where

$$a_1^p = \frac{a_1}{|(m-1)\ln q|}, \quad a_2^p = \frac{a_2}{|(m-1)\ln q|}.$$

In the general case, the coefficients K_i ($i = 1, 2, 3$) are determined from the initial system of time-independent master equations presented in [2–4], and their explicit form is of no importance here. Furthermore, a_1 and a_2 can be expressed in terms of the coefficients α_{ij} of system (1.1) and unknown ratios

$$\frac{A_1}{A_3} = \frac{K_1}{K_3} = \Omega_1$$

and

$$\frac{A_2}{A_3} = \frac{K_2}{K_3} = \Omega_2.$$

A solution of Eqs. (1.5) that is different from the trivial solution $\eta = 0$ can be obtained from the equations

$$f_1 = A_1 + K_1\eta^2 = 0,$$
$$f_2 = A_2 + K_2\eta^2 = 0, \quad f_3 = A_3 + K_3\eta^2 = 0. \tag{1.6}$$

Excluding the η variable from Eqs. (1.6) by calculating the resultants $R_1[f_1, f_3]$ and $R_2[f_2, f_3]$ and equating the resultants to zero, we arrive at the following equations in the unknowns α_1^p and α_2^p:

$$R_1[f_1, f_3] = [\alpha_{11} - \alpha_{14} - \Omega_1(\alpha_{51} - \alpha_{54})]\alpha_1^p + (\Omega_1\alpha_{53} - \alpha_{13})\alpha_2^p - \Omega_1\alpha_{56} + \alpha_{16} = 0,$$
$$R_2[f_2, f_3] = [\alpha_{31} - \alpha_{34} - \Omega_2(\alpha_{51} - \alpha_{54})]\alpha_1^p + (\Omega_2\alpha_{53} + \alpha_{32} - \alpha_{33})\alpha_2^p - \Omega_2\alpha_{56} + \alpha_{36} = 0, \tag{1.7}$$

whose solution has the form

$$a_1^p = \frac{\Delta_1(\Omega_1, \Omega_2)}{\Delta(\Omega_1, \Omega_2)}, \quad a_2^p = \frac{\Delta_2(\Omega_1, \Omega_2)}{\Delta(\Omega_1, \Omega_2)},$$

where

$$\Delta_1(\Omega_1, \Omega_2) = [\alpha_{56}(\alpha_{32} - \alpha_{33}) + \alpha_{36}\alpha_{53}]\Omega_1 - (\alpha_{16}\alpha_{53} - \alpha_{13}\alpha_{56})\Omega_2 - \alpha_{13}\alpha_{36} - \alpha_{16}(\alpha_{32} - \alpha_{33}),$$
$$\Delta_2(\Omega_1, \Omega_2) = \alpha_{16}(\alpha_{31} - \alpha_{34}) - \alpha_{36}(\alpha_{11} - \alpha_{14}) + [\alpha_{36}(\alpha_{51} - \alpha_{54}) - \alpha_{56}(\alpha_{31} - \alpha_{34})]\Omega_1 - [\alpha_{16}(\alpha_{51} - \alpha_{54}) - \alpha_{56}(\alpha_{11} - \alpha_{14})]\Omega_2, \quad (1.8)$$

$$\Delta(\Omega_1, \Omega_2) = (\alpha_{11} - \alpha_{14})(\alpha_{32} - \alpha_{33}) + \alpha_{13}(\alpha_{31} - \alpha_{34}) - [\alpha_{53}(\alpha_{31} - \alpha_{34}) + (\alpha_{32} - \alpha_{33})(\alpha_{51} - \alpha_{54})]\Omega_1 - [\alpha_{13}(\alpha_{51} - \alpha_{54}) - \alpha_{53}(\alpha_{11} - \alpha_{14})]\Omega_2.$$

Hence, the coefficients A_1, A_2, and A_3 have the form

$$A_1 = -\frac{\det \cdot \Omega_1}{\Delta(\Omega_1, \Omega_2)}, \quad A_2 = -\frac{\det \cdot \Omega_2}{\Delta(\Omega_1, \Omega_2)}, \quad A_3 = -\frac{\det}{\Delta(\Omega_1, \Omega_2)}.$$

Multiplying the first, second, and third of Eqs. (1.5) by

$$[\alpha_{53}(\alpha_{32} - \alpha_{34}) + (\alpha_{32} - \alpha_{33})(\alpha_{51} - \alpha_{54})],$$
$$[\alpha_{13}(\alpha_{51} - \alpha_{54}) - \alpha_{53}(\alpha_{11} - \alpha_{14})],$$

and

$$[\alpha_{31}(\alpha_{34} - \alpha_{31}) + (\alpha_{11} - \alpha_{14})(\alpha_{33} - \alpha_{32})],$$

respectively, and summarizing the results, we obtain

$$\det \cdot \eta + M\eta^3 = 0, \quad (1.9)$$

where

$$M = 2I\{K_1[\alpha_{53}(\alpha_{31} - \alpha_{34}) + (\alpha_{32} - \alpha_{33})(\alpha_{51} - \alpha_{54})] + K_2[\alpha_{13}(\alpha_{51} - \alpha_{54}) - \alpha_{53}(\alpha_{11} - \alpha_{14})] + K_3[\alpha_{13}(\alpha_{34} - \alpha_{31}) + (\alpha_{11} - \alpha_{14})(\alpha_{33} - \alpha_{32})]\}.$$

In addition to the trivial solution $\eta = 0$, Eq. (1.9) has the solution $\eta = \sqrt{-\frac{\det}{M}}$. Values q_k at which det = 0 determine the disordering temperature of binary crystals, which have the simple cubic lattice and are crystallized from 50%-alloy melts.

2. ORDER–DISORDER PROCESS IN BINARY METALLIC CRYSTALS IN THE QUASI-BRAGG–WILLIAMS APPROXIMATION

When expansions (1.3) are valid, the linearized homogeneous system (1.1) can be used instead of the Taylor series of all time-independent master equations in the η parameter up to η^3 terms. In this approach and in view of the symmetry properties (1.2), system (1.5) is an analogue of such a virtual approximate system. In this approximation, the coefficients K_1, K_2, and K_3 in Eqs. (1.5) can be written in the form

$$K_1 \simeq (\alpha_{11} - \alpha_{14})c_1^p - \alpha_{16}c_2^p,$$
$$K_2 \simeq (\alpha_{31} - \alpha_{34})c_1^p + (\alpha_{32} - \alpha_{33})c_2^p,$$
$$K_3 \simeq (\alpha_{51} - \alpha_{54})c_1^p - \alpha_{53}c_2^p, \quad (2.1)$$

where

$$c_1^p = \frac{c_1}{|(m-1)\ln q|}, \quad c_2^p = \frac{c_2}{|(m-1)\ln q|}.$$

Taking into account that $R = \frac{\omega_+}{\nu} \ll 1$ for many practical cases [8], we obtain the following estimates of the coefficients α_{ij} appearing in Eqs. (1.1):

$$\alpha_{11} \simeq -\frac{2q^{m+2}}{N}\kappa, \quad \alpha_{13} \simeq -\frac{8R}{N}\kappa, \quad \alpha_{14} \simeq \frac{2q^{m+2}}{N}\kappa,$$
$$\alpha_{15} \simeq \frac{R(1+2\kappa)}{N}, \quad \alpha_{16} \simeq \frac{4Rq^{\frac{1}{2}(m+1)}}{N}\kappa,$$
$$\alpha_{31} \simeq -\frac{2q^{m+2}}{N}\kappa, \quad \alpha_{32} \simeq \frac{4R}{N}\kappa, \quad \alpha_{33} \simeq \frac{8R^2q^{-1}}{N}\kappa \simeq 0,$$
$$\alpha_{34} \simeq \frac{4R}{N}\kappa, \quad \alpha_{35} \simeq -\frac{R(1+2\kappa)}{N}, \quad (2.2)$$
$$\alpha_{36} \simeq \frac{2Rq^{\frac{1}{2}(m+1)}}{N}\kappa, \quad \alpha_{51} \simeq -\frac{4q^{m+2}}{N}\kappa,$$
$$\alpha_{53} \simeq \frac{4q^{\frac{1}{2}(3m+1)}}{N}\kappa, \quad \alpha_{54} \simeq \frac{4q^{\frac{1}{2}(m+3)}}{N}\kappa, \quad \alpha_{55} \simeq \frac{q^{\frac{1}{2}(3m+1)}}{N},$$
$$\alpha_{56} \simeq \frac{q^{\frac{1}{2}(3m+1)}}{N}\kappa,$$

where $\kappa = \frac{q^{2m+1}}{R} - 1$, which are accurate up to $\sim\frac{1}{N}$

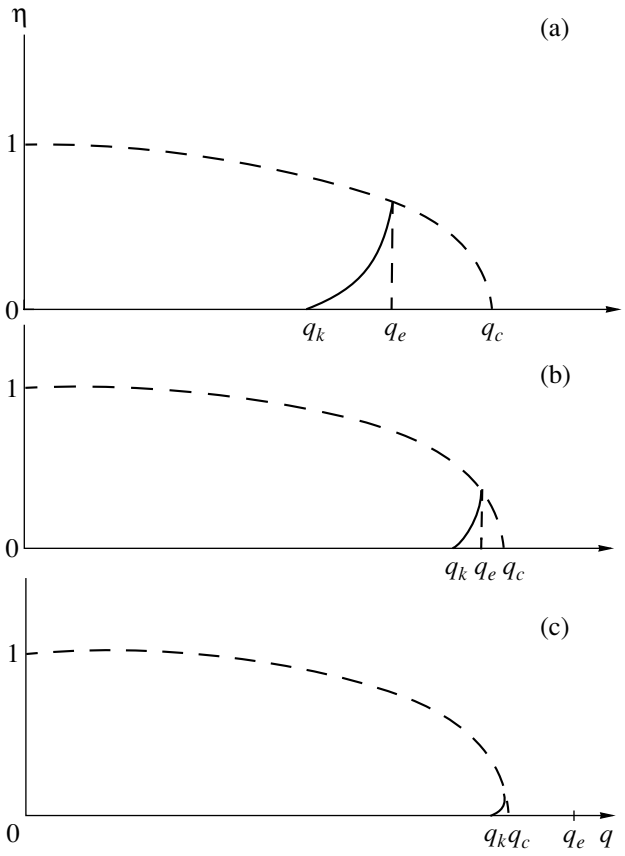

Fig. 3. Qualitative dependence of the long-range order parameter on $q = \exp\left[-\frac{\varepsilon_{AA}}{T}\right]$ in the case of the topological-form effect of the TPT zone on the disordering process for (a) $q_k < q_e < q_c$, (b) $q_k < q_e \leq q_c$, and (c) $q_k < q_c < q_e$. The dashed and solid lines are the thermodynamic-ordering and kinetic-disordering curves, respectively.

terms. In this case, Eq. (1.9) is transformed to the equation

$$\frac{2\kappa}{N}q^{m+1}\left(1+q^{\frac{1}{2}(m+1)}\right)(1-q^m)\eta - [6K_2 - K_1(3+2q^{m-1})]\eta^3 = 0. \quad (2.3)$$

In the approximation given by Eqs. (2.1) and (2.2) and in the general case where $c_1^p \neq c_2^p$, the coefficient of the η^3 term in Eq. (2.3) has the form

$$6K_2 - K_1(3+2q^{m-1}) = \frac{8R\kappa}{N}[(\kappa-2)c_1^p - 2q^{m-1}c_2^p].$$

In addition to the trivial solution $\eta = 0$, Eq. (2.3) has the solution

$$\eta = \sqrt{\text{const}}\sqrt{1+\frac{\kappa}{2}\left(1-q^{m-1}\frac{c_2^p}{c_1^p}\right)},$$

where

$$\text{const} = -\frac{q^{m+1}(1-q^m)\left(1+q^{\frac{1}{2}(m+1)}\right)}{8Rc_1^p\left(1+q^{m-1}\frac{c_1^p}{c_2^p}\right)}.$$

Since the coefficients c_1^p and c_2^p are commensurate due to the physical nature of series (1.3) and in view of the inequality $q^{m-1}\left|\frac{c_1^p}{c_2^p}\right| < 1$, it is obvious that $c_1^p < 0$ for real systems. The long-range order parameter η tends to zero; i.e., the disordering process is possible only for q_k values that are the roots of the equation

$$1+\frac{\kappa}{2}\left(1-q^{m-1}\frac{c_2^p}{c_1^p}\right) = 0.$$

Considering that $R \sim q^{2m+1} \ll 1$ in real physical systems (see [2–4]) and neglecting the $Rq^{m-1}\frac{c_1^p}{c_2^p} \sim 0$ term, we estimate the root of Eq. (2.4) as $q_k \simeq \left(2\frac{c_1^p}{c_2^p}R\right)^{\frac{1}{3m}}$. As is seen from this solution, the disordering process in stoichiometric binary crystals, which are grown from 50%-alloy melts and have the simple cubic lattice, is realized only under the condition $\operatorname{sgn}c_1^p = \operatorname{sgn}c_2^p$; i.e., when both quantities c_1^p and c_2^p appearing in series (1.3) are negative. Since $q_k = \left(2\frac{c_1^p}{c_2^p}R\right)^{\frac{1}{3m}}$ is a first-order root, the long-range order parameter η tends to zero as $\sqrt{q-q_k} \sim \sqrt{T-T_k}$, i.e., similarly to the Bragg–Williams thermodynamic order–disorder transition. Thus, in the presence of the concentration image of the TPT zone and under conditions (2.1), the disordering process in quasi-stoichiometric binary crystals with the simple cubic lattice is realized in the so-called quasi-Bragg–Williams approximation. In this case, the topological structure of the concentration image of the TPT zone (its steplike form) is not manifested in the disordering process in question. In the general order–disorder phenomenon analyzed in [2–5], where conditions (2.1) were not taken into account, the long-range order parameter η tended to zero as $(T-T_k)^{5/2}$ (see Fig. 3).

The $\eta(q)$ dependence obtained in the quasi-Bragg–Williams approximation is shown in Fig. 4, where three possible cases of ratios between the parameters q_k, q_e, and q_c are presented. These parameters are related to

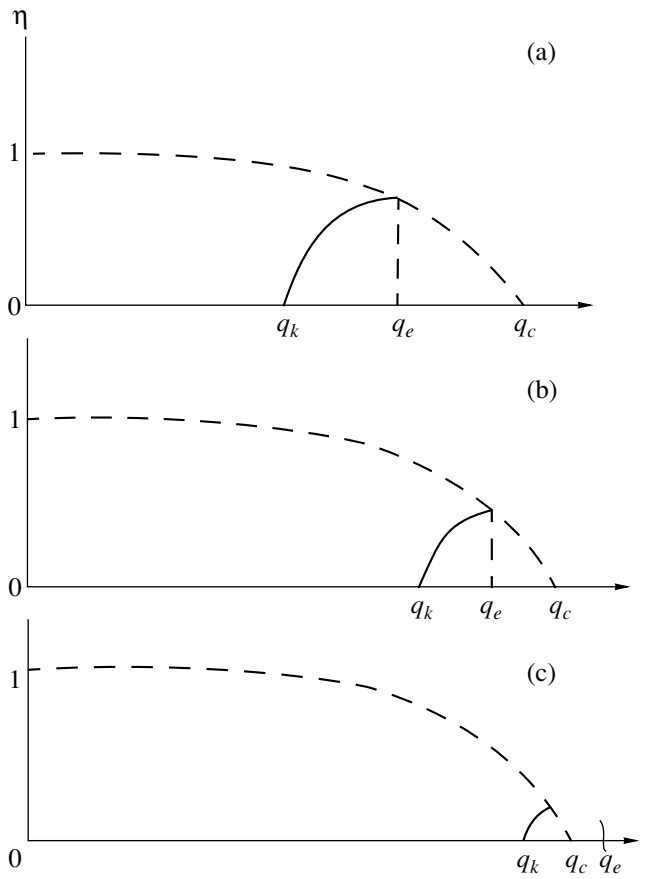

Fig. 4. Same as in Fig. 3, but for the quasi-Bragg–Williams approximation, where q is proportional to the temperature of the TPT zone.

the disordering temperature T_k, kinetic equilibrium temperature T_e, and Curie temperature T_C by the formulas

$$q_k = \exp\left[-\frac{\varepsilon_{AA}}{T_k}\right], \quad q_e = \exp\left[-\frac{\varepsilon_{AA}}{T_e}\right],$$

and

$$q_c = \exp\left[-\frac{\varepsilon_{AA}}{T_C}\right],$$

respectively. Therefore, the three cases shown in Fig. 4 are as follows: (a) $T_k < T_e < T_C$, (b) $T_k < T_e \leqslant T_C$, and (c) $T_k < T_C < T_e$. The kinetic equilibrium temperature T_e is determined from the condition $V = 0$, where V is the average rate of TPT-zone crystallization (see [2–4]). As is seen in Figs. 3 and 4, the kinetic equilibrium temperature T_e is determined by the point where the thermodynamic curve crosses the kinetic curve, because the disordering process begins just at the instant of the onset of crystal growth.

CONCLUSIONS

The long-range order parameter in the disordering process considered above was shown to tend to zero as $\eta \sim \sqrt{T - T_k}$ when the melt temperature T approaches the disordering temperature T_k. This behavior is similar to the thermodynamic order–disorder transition in the Bragg–Williams approximation. For this reason, this case was called the quasi-Bragg–Williams approximation. The above analysis demonstrated that the fluctuation crystallization mechanism developed in [9–13] is immaterial for the disordering process of quasi-stoichiometric binary crystals with the simple cubic lattice.

REFERENCES

1. Yu. D. Ĉistyakov and Yu. A. Baĭkov, in *Advances in Epitaxy and Endotaxy* (Akad. Kiado, Budapest, 1976), pp. 257–263.
2. Yu. A. Baĭkov, Yu. V. Zelenev, W. Haubenreisser, and H. Pfeiffer, Phys. Status Solidi A **61** (1), 435 (1980).
3. Yu. D. Chistyakov, Yu. A. Baĭkov, H. G. Schneider, and V. Ruth, Cryst. Res. Technol. **20** (8), 1007 (1985).
4. Yu. D. Chistyakov, Yu. A. Baĭkov, H. G. Schneider, and V. Ruth, Cryst. Res. Technol. **20** (9), 1149 (1985).
5. Yu. A. Baĭkov and V. P. Meshalkin, in *Collection of Scientific Works* (Sputnik, Moscow, 1999), pp. 94–103.
6. Yu. D. Chistyakov, Yu. A. Baĭkov, H. G. Schneider, and V. Ruth, Cryst. Res. Technol. **18** (6), 711 (1983).
7. Yu. V. Zelenev, Yu. A. Baĭkov, and A. P. Molotkov, Krist. Tech. **14** (4), 389 (1979).
8. Yu. A. Baĭkov, Doctoral Dissertation in Physics and Mathematics (Moscow, 1995), p. 372.
9. Yu. A. Baĭkov and Yu. D. Chistyakov, Cryst. Res. Technol. **25** (2), 171 (1990).
10. Yu. A. Baĭkov and Yu. D. Chistyakov, Izv. Akad. Nauk SSSR, Met., No. 3, 62 (1991).
11. Yu. A. Baĭkov and V. P. Meshalkin, Neorg. Mater. **35** (9), 1061 (1999).
12. P. D. Sarkissov, Yu. A. Baĭkov, and V. P. Meshalkin, in *Collection of Works of Russian-Israel Conference on Optimization of Composition, Structure, and Properties of Metals, Oxides, Composites, Nano- and Amorphous Materials, Moscow–Yekaterinburg, June 30–July 9, 2002*, p. 172.
13. P. D. Sarkissov, V. P. Meshalkin, and Yu. A. Baĭkov, in *Collection of Works of Russian-Israel Conference on Optimization of Composition, Structure, and Properties of Metals, Oxides, Composites, Nano- and Amorphous Materials, Moscow–Yekaterinburg, June 30–July 9 2002*, p. 184.

Translated by Yu. Baĭkov

Doklady Physics, Vol. 48, No. 6, 2003, pp. 296–302. Translated from Doklady Akademii Nauk, Vol. 390, No. 4, 2003, pp. 468–474.

TECHNICAL PHYSICS

Robust Nonlinear Filtration of Noisy-Image Sequences

V. F. Kravchenko[1], V. I. Ponomarev[2,*], Corresponding Member of the RAS V. I. Pustovoĭt[3], and J. C. Sánchez-García[2,]**

Received December 21, 2002

1. Nonlinear filtration methods are extensively used in remote sounding, processing of medical information such as electroencephalograms, cardiograms, or tomograms. These methods suppress the effect of noise of various physical natures [1–3].

In this work, we proposed a new approach based on the joint use of rank statistics and M-estimates (generalized maximum-likelihood estimates) [4]. This approach enables one to use the advantages of each method of nonlinear filtration and to develop a new class of robust algorithms of filtering both individual images and sequences of exposures (video and tomographic). This provides a significant improvement in the quality of filtering images and sequences of video exposures, including the suppression of various types of noise, reconstruction of small details of images, and on-line realization of filtration procedures. The latter is particularly important and realized through algorithms based on the digital processing of signals with the use of a TMS320C6701 digital signal processor [5]. This experimentally corroborates the possibility of on-line filtering of various sequences of video images in the presence of various types of noise.

2. It is known that nonparametric estimates are based on calculations of ranks and rank statistics [4, 6]. A hypothesis of a shift in one of two samples $x_1, x_2, \ldots, x_m$ and $y_1, y_2, \ldots, y_n$ with the same probability distribution is generally verified by the Fisher–Jets–Terry–Hefding criterion. It has the form [4]

$$S_N = \frac{1}{m}\sum_{i=1}^{m} a_N(R_i),$$

where

$$a_N(i) = N \int\limits_{\left[\frac{i-1}{N}, \frac{i}{N}\right]} J(u)du$$

is a positive affine transformation for ranks R_i of the sample formed from two original samples. For a Gaussian distribution $[J(u) = \Phi^{-1}(u)]$, this criterion is equivalent to the van der Waerden test. For a logistic distribution, the solution is determined by the Hodges–Lehmann estimate $\left[J(u) = u - \frac{1}{2}\right]$, and the criterion transforms to the Wilkokson test. Finally, a double exponential distribution determines the sign criterion: $J(u) = -1$ for $u < \frac{1}{2}$, $J(u) = 1$ for $u > \frac{1}{2}$, and the median algorithm for estimating a shift [2, 4]. When there is no prior information about the probability distribution of data and moments, the sign criterion is the most powerful asymptotic rank criterion. When the probability distribution is symmetric, the Wilkokson test is such a criterion. Other R-estimates can be obtained similarly by using various functions $J(t)$. Two estimates additionally presented below are used to construct new nonlinear filters. The Ansari–Bradley–Siegel–Tukey function $J(t) = \left|t - \frac{1}{2}\right| - \frac{1}{4}$ [4] determines the general-criterion coefficients $a_i = \dfrac{2i - \frac{3}{2}N - 1}{2N}$ and corresponding R-estimate in the form

$$\theta_A = \text{med}\left\{\begin{array}{ll} X_{(i)}, & i \le \dfrac{N}{2} \\ \dfrac{1}{2}(X_{(i)} + X_{(j)}), & i > \dfrac{N}{2} \end{array}\right\}. \qquad (1)$$

The Mood function $J(t) = \left(t - \frac{1}{2}\right)^2 - \frac{1}{2}$ specifies

[1] *Institute of Radio Engineering and Electronics, Russian Academy of Sciences, ul. Mokhovaya 18, Moscow, 103907 Russia*

[2] *Instituto Politécnico Nacional, Mexico city, 04430 México*

* *e-mail: vponomar@ipn.mx*

** *e-mail: jcsanche@prodigy.net.mx*

[3] *Scientific and Technological Centre of Unique Instrumentation, Russian Academy of Sciences, ul. Butlerova 15, Moscow, 117342 Russia*

1028-3358/03/4806-0296$24.00

the general-criterion coefficients

$$a_i = \frac{i^2 - i - \frac{1}{3}}{N^3} - \frac{2i - \frac{1}{3}N - 1}{2N^2}$$

and corresponding R-estimate in the form

$$\theta_M = \text{med}\left\{\begin{array}{ll} \frac{1}{2}(X_{(i)} + X_{(j)}), & i \le 3 \\ X_{(i)}, & i > 3 \end{array}\right\} \quad (2)$$

$$\text{for } i = 1, 2, \ldots, N.$$

3. The maximum-likelihood (ML) estimate modified by Huber is determined by the so-called M-estimate following from the generalized maximum-likelihood equation [2, 4, 7]

$$\sum_{i=1}^{n} \psi(X_i - \theta) = 0. \quad (3)$$

Here, $\psi(X, \theta) = \frac{\partial}{\partial\theta}\rho(X, \theta)$ with $\rho(X) = \ln(f(X))$, where $f(x)$ is the probability density of the sample of outcomes. In contrast to the classical maximum-likelihood estimate θ, a robust estimate is obtained under certain restrictions on the function $\psi(X)$. In particular, these are restrictions on the function amplitude, which leads to the Huber M-estimate for the simplest case, when the normal distribution has long tails:

$$\tilde{\psi}_r(X) = \min(r, \max(X, -r)) = [X]_{-r}^{r}$$

with the interval $(-r, r)$ determined by prior data. As was shown in [4], the truncated median

$$\tilde{\psi}_{m(r)}(X) = \begin{cases} \text{sgn}(X), & |X| \le r \\ 0, & X > r \end{cases}$$

is the most robust variant of the reduced M-estimate.

We also use other influence functions, such as three-interval Hampel, sine Andrews, Tukey, and Bernoulli functions. Our approach is based on the joint application of rank statistics and M-estimates and uses rank procedures rather than the arithmetic smoothing used in M-estimates. As was shown in [6, 8], the simplest RM-estimates associated with rank median and Wilkokson procedures are written as

$$\theta_{mM} = \text{med}\{X_i\tilde{\psi}(X_i - \text{med}\{\mathbf{X}\}), i = 1, 2, \ldots, n\}, \quad (4)$$

$$\theta_{WM} = \underset{i \le j}{\text{med}}\{0.5[X_i\tilde{\psi}(X_i - \text{med}\{\mathbf{X}\}) + X_j\tilde{\psi}(X_j - \text{med}\{\mathbf{X}\})], i = 1, 2, \ldots, n\}. \quad (5)$$

Using estimates given by Eqs. (1) and (2), we similarly arrive at the following new RM-estimates:

$$\theta_{AM} = \text{med}\left\{\begin{array}{l} X_i\tilde{\psi}(X_i - \text{med}\{\mathbf{X}\}), \quad i \le \frac{N}{2} \\ \frac{1}{2}[X_i\tilde{\psi}(X_i - \text{med}\{\mathbf{X}\}) \\ + X_j\tilde{\psi}(X_j - \text{med}\{\mathbf{X}\})], \quad i > \frac{N}{2} \end{array}\right\}, \quad (6)$$

$$\theta_{MM} = \text{med}\left\{\begin{array}{l} \frac{1}{2}[X_i\tilde{\psi}(X_i - \text{med}\{\mathbf{X}\}) \\ + X_j\tilde{\psi}(X_j - \text{med}\{\mathbf{X}\})], \quad i \le 3 \\ X_i\tilde{\psi}(X_i - \text{med}\{\mathbf{X}\}), \quad i > 3 \end{array}\right\}. \quad (7)$$

4. To estimate various kinds of noise, we use the results [7, 8]

$$u(x, y) = n_{\text{imp}}(e(x, y)), \quad (8)$$

where $e(x, y)$ is the proper image, $u(x, y)$ is the noisy image, and

$$n_{\text{imp}}(e(x, y)) = \begin{cases} \text{random-amplitude outlier} \\ \text{with probability } P_i \\ e(x, y) \quad \text{otherwise} \end{cases}$$

is the functional determining the impulsive-noise effect.

When an image is contaminated with multiplicative and impulsive noise, the model has the form

$$u(x, y) = n_{\text{imp}}(\varepsilon_{\text{mul}}(x, y) \cdot e(x, y)), \quad (9)$$

where $\varepsilon_{\text{mul}}(x, y)$ is multiplicative noise.

Our aim is to develop robust RM-estimates that are based on the above approach and make it possible to remove impulsive and multiplicative noise and to reconstruct small details of the image. This approach was applied to develop a class of filtration algorithms, some of which were presented in our previous papers [7, 9].

The robust properties of the standard *K*NN filtration algorithm (*K* nearest neighboring readings) are improved by using the MM*K*NN filter (maximum-likelihood median filter of *K* nearest neighboring readings)

$$\hat{e}^{(q)}_{\text{MM}K\text{NN}}(i, j) = \text{med}\{g^{(q)}(i + m, j + n)\}, \quad (10)$$

or the WM*K*NN filter (maximum-likelihood Wilkokson

filter of K nearest neighboring readings)

$$\hat{e}^{(q)}_{\mathrm{WM}K\mathrm{NN}}(i, j) = \mathrm{med}\left\{\frac{g^{(q)}(i+m, j+n) + g^{(q)}(i+m_1, j+n_1)}{2}\right\}. \quad (11)$$

Here, $g^{(q)}(i+m, j+n)$ and $g^{(q)}(i+m_1, j+n_1)$ are sets of K_c pixels that are weighted with the $\tilde{\psi}(X)$ function and are close to the values at the preceding step $\hat{e}^{(q-1)}_{\mathrm{MM}K\mathrm{NN}}(i, j)$ and $\hat{e}^{(q-1)}_{\mathrm{WM}K\mathrm{NN}}(i, j)$ for filters (10) and (11), respectively]. In addition, $m, n = -L, ..., L$; $\hat{e}^{(0)}_{\mathrm{MM}K\mathrm{NN}}(i, j) = \hat{e}^{(0)}_{\mathrm{WM}K\mathrm{NN}}(i, j) = u(i, j)$; $(2L+1)^2$ is the size of the filtration window; q is the current iteration number; $\hat{e}^{(q)}_{\mathrm{MM}K\mathrm{NN}}$ and $\hat{e}^{(q)}_{\mathrm{WM}K\mathrm{NN}}$ are the estimates at the qth iteration; and $K_c(i, j)$ is the current number of nearest neighboring pixels. This number presents the local activity of data and the presence of outliers in the filtration window and is determined as

$$K_c(i, j) = K_{\min} + aS(u(i, j)) \le K_{\max}.$$

Here,

$$S(u(i, j)) = [\mathrm{med}\{|u(i, j) - u(i+m, j+n)|\}/\mathrm{MADM}] + [0.5\mathrm{MADM}/\mathrm{med}\{u(i+k, j+l)\}],$$

the parameter a controls the sensitivity of the filtration algorithm to local variations in data in order to determine the boundaries of objects, the maximum number $K_{\max}$ of elements neighboring the central element characterizes the smoothing of boundaries and conservation of small details of the image, and $K_{\min}$ is the minimum number of neighboring pixels for suppressing noise in regions where sharp changes in the image are absent. In the last formula, *MADM* is the median of the absolute deviations from the median [9].

Using RM-estimates (6) and (7), we obtain new algorithms: AM*K*NN (Ansari–Bradley–Siegel–Tukey maximum-likelihood filter of K nearest neighboring readings)

$$\hat{e}^{(q)}_{\mathrm{AM}K\mathrm{NN}} = \mathrm{med}\left\{\begin{array}{c} g^{(q)}(i+m, j+n), \quad i \le \frac{N}{2} \\ \frac{1}{2}[g^{(q)}(i+m, j+n) \\ +g^{(q)}(i+m_1, j+n_1)], \ i > \frac{N}{2} \end{array}\right\} \quad (12)$$

and MoM*K*NN (Mood maximum-likelihood filter of K nearest neighboring readings)

$$\hat{e}^{(q)}_{\mathrm{MoM}K\mathrm{NN}} = \mathrm{med}\left\{\begin{array}{c} \frac{1}{2}[g^{(q)}(i+m, j+m) \\ +g^{(q)}(i+m_1, j+n_1)], \ i \ge 3 \\ g^{(q)}(i+m, j+m), \quad i > 3 \end{array}\right\}. \quad (13)$$

Here, $g^{(q)}(i+m, j+n)$ and $g^{(q)}(i+m_1, j+n_1)$ mean the same as in the above filters specified by Eqs. (10) and (11). To suppress multiplicative noise, another robust filter was proposed [8]. It recovers the details of an image by using the above estimates $\hat{e}_{\mathrm{MM}K\mathrm{NN}}$, $\hat{e}_{\mathrm{WM}K\mathrm{NN}}$, $\hat{e}_{\mathrm{AM}K\mathrm{NN}}$, and $\hat{e}_{\mathrm{MoM}K\mathrm{NN}}$ in the form

$$\hat{e}_{\mathrm{M}}(i, j) = \frac{\sum_{m=-L}^{L}\sum_{n=-L}^{L} u(i, j)\tilde{\psi}'\{u(i+m, j+n) - \hat{e}^{(0)}(i, j)\}}{\sum_{k=-L}^{L}\sum_{l=-L}^{L} \tilde{\psi}'\{u(i+m, j+n) - \hat{e}^{(0)}(i, j)\}}, \quad (14)$$

where

$$\tilde{\psi}'\{u(i+m, j+n) - \hat{e}^{(0)}(i, j)\} = \left\{\begin{array}{l} 1, \ u(i+m, j+n) - \hat{e}^{(0)}(i, j) \le b\ \mathrm{med}\{u(i, j)\} \\ 0 \text{ otherwise} \end{array}\right\},$$

when using the simplest function ψ, which is replaced with other functions: truncated median, Hampel, sine Andrews, Tukey, or Bernoulli function. Here, $\mathrm{med}\{u(i, j)\}$ is the median of the samples of pixels within the filtration window; b controls the suppression of multiplicative noise; $m, n = -L, \ldots, L$, $2(L+1)$ determines the size of the filtration window; and the initial iteration is $\hat{e}^{(0)}(i, j) = \hat{e}_{\mathrm{MM}K\mathrm{NN}}(i, j)$ or $\hat{e}^{(0)}(i, j) = \hat{e}_{\mathrm{WM}K\mathrm{NN}}(i, j)$ depending on the type of the preceding filter. To conserve small details in the image, we apply the following adaptive scheme, similar to that realized in the Lee local statistical filter [9]:

$$\hat{e}(i, j) = \hat{e}_{\substack{\mathrm{MM}K\mathrm{NN} \\ \mathrm{WM}K\mathrm{NN}}}(i, j)Q(i, j) + (1 - Q(i, j))\hat{e}_{\mathrm{M}}(i, j), \quad (15)$$

$$Q(i, j) = 1 - \left(c\frac{\hat{e}_{\mathrm{M}}(i, j)}{\mathrm{med}\{|\hat{e}_{\mathrm{M}}(i, j) - u(i+m, j+n)|\}}\right)^2,$$

where $Q(i, j)$ is the robust estimate of the local activity of the sample and c controls the reconstruction of small details of the image.

Table 1. Results of the filtration of various images contaminated with 20% impulsive noise

Algorithm	Barbara		Boat		Goldhill		Lena		Peppers	
	PSNR	*MAE*	*PSNR*	*MAE*	*PSNR*	*MAE*	*PSNR*	*MAE*	*PSNR*	*MAE*
5×5 median	21.62	14.32	20.80	14.51	22.41	14.46	23.09	10.95	22.83	11.24
WM 5×5	22.83	11.04	21.99	10.56	24.07	10.36	24.33	8.12	24.29	8.04
LUM 5×5	22.26	12.50	21.91	12.08	23.10	12.07	23.26	10.62	23.65	11.37
FIRMH 5×5	21.44	12.81	21.28	12.35	22.21	12.39	22.37	10.61	21.96	11.17
ROM 3×3	**23.84**	10.96	23.40	10.55	24.82	10.57	25.20	9.11	25.04	9.62
MMEM 3×3	22.93	12.09	22.92	11.36	24.16	11.09	24.52	9.46	24.40	9.67
TSM 3×3	21.77	13.86	21.47	13.13	23.11	12.43	23.56	10.80	22.96	11.38
ACWM 3×3	23.67	11.08	23.26	10.57	24.84	10.43	25.56	8.75	25.18	9.21
MM*K*NN, simple	23.13	11.26	22.19	11.95	24.80	10.28	24.90	8.54	24.74	8.83
MM*K*NN, truncated	23.49	**10.79**	22.89	10.04	25.33	**9.93**	**25.68**	**7.55**	25.97	**7.52**
MM*K*NN, Hampel	23.47	10.83	**23.60**	**9.75**	**25.35**	10.01	25.54	7.65	**26.20**	7.68
WM*K*NN, simple	23.42	10.86	22.99	10.19	25.22	10.00	25.63	7.62	25.90	7.59
WM*K*NN, truncated	23.45	10.81	23.02	10.15	25.29	9.97	25.66	7.60	25.92	7.55
WM*K*NN, Hampel	23.38	10.85	22.84	10.26	25.19	10.00	25.45	7.67	25.60	7.63

Therefore, the resulting cascade RM filter is determined by two filters: the MM*K*NN (WM*K*NN or new filters AM*K*NN and MoM*K*NN) filter specified by Eqs. (10)–(12) or (13), which suppresses noise with the conservation of small details of the image, and the *M* filter given by Eqs. (14) and (15), which suppresses multiplicative noise.

5. The above filtration algorithms are realized by using a Texas Instruments TMS320C6701 floating-point processor for detecting and processing signals [5, 8].

Comparison was made with the following criteria: (i) the peak signal-to-noise ratio

$$PSNR = 10\log\left[\frac{(255)^2}{MSE}\right],$$

measured in decibels, where

$$MSE = \langle |e(x, y) - \hat{e}(x, y)|^2 \rangle$$

is the mean square error, and (ii) the mean absolute error

$$MAE = \frac{1}{MN}\sum_{i=0}^{M-1}\sum_{j=0}^{N-1}|e(i, j) - \hat{e}(i, j)|$$

determining the quality of the reconstruction of small details in the image [2].

To compare the qualitative characteristics, we also simulate the following filters: (i) standard median, (ii) general weighted median (WM) [2], (iii) lower–middle–upper (LUM) [2], (iv) median hybrid (FIRMH) [2], (v) rank ordered mean (ROM) [2], (vi) minimum–maximum mean (MMEM) [10], (vii) three-state median (TSM) [11], (viii) stack [2], and (ix) adaptive center-weighted (ACWM) [12].

The developed filters were applied to process the well-known and extensively used Barbara, Boat, Goldhill, Lena, Peppers, etc., images as test images. For the *PSNR* and *MAE* criteria of the signal-to-noise ratio, Table 1 presents some simulation results for various probabilities of impulsive noise (in the absence of multiplicative noise). The results of the processing of various images show that the proposed filters are preferable for the reconstruction of small details (*MAE* values). Moreover, the *PSNR* criterion for new filters is often better than that for known filters [2, 9–12]. The filters used for comparison with proposed filters were chosen and realized according to [2, 9–12]. The characteristics of these standard filters are better than those of other known algorithms. We note that the ROM filter requires a training stage and therefore cannot be realized in the on-line regime.

The properties of the cascade RM filter specified by Eqs. (10), (14), and (15) are tested on the Lena test image contaminated by multiplicative noise with rms deviations 0.05, 0.1, and 0.25 and impulsive noise with various intensities. This filter is compared with the following filters developed to process images in the pres-

Table 2. Peak signal-to-noise ratio criterion in decibels for various filters

Exposure no.	Filter				MM*K*NN-filter			WM*K*NN-filter		
	WM	TSM	ACWM	MMEM	simple	truncated	Hampel	simple	truncated	Hampel
1	23.53	27.90	29.52	27.68	32.54	33.04	33.75	32.84	**36.63**	35.11
2	27.49	28.21	29.85	27.78	34.59	35.21	36.63	35.05	**44.25**	40.33
3	29.01	28.34	29.82	28.16	36.22	37.06	39.03	36.67	37.66	**40.09**
4	30.04	28.79	29.95	27.73	36.26	38.51	42.75	37.15	40.11	47.24
5	26.58	27.96	29.59	27.72	34.06	35.19	35.94	34.43	**40.17**	39.44
6	27.58	28.08	29.78	27.77	35.81	36.97	38.75	36.38	46.53	**53.95**
7	32.41	28.12	29.66	28.54	39.95	**45.90**	42.09	41.80	34.34	36.70
8	32.36	28.17	29.82	28.16	37.49	39.67	**42.64**	38.48	39.52	40.63
9	30.65	28.48	30.10	28.17	40.75	**44.12**	42.50	41.97	35.23	36.74
10	30.22	29.08	29.91	28.29	40.01	**43.18**	42.45	41.52	38.18	40.18

Table 3. Mean absolute error for various filters

Exposure no.	Filter				MM*K*NN-filter			WM*K*NN-filter		
	WM	TSM	ACWM	MMEM	simple	truncated	Hampel	simple	truncated	Hampel
1	8.16	8.26	7.24	6.63	5.24	5.17	5.26	**5.11**	5.64	5.73
2	8.17	8.18	7.21	6.49	4.99	4.97	5.05	**4.86**	5.34	5.44
3	8.00	8.18	7.26	6.41	4.78	4.80	4.82	**4.69**	5.21	5.29
4	7.73	8.01	7.22	6.38	4.47	4.56	4.60	**4.40**	4.90	5.05
5	7.96	8.23	7.26	6.41	4.79	4.77	4.84	**4.68**	5.18	5.27
6	8.08	8.25	7.37	6.68	4.88	4.83	4.91	**4.77**	5.25	5.36
7	7.81	8.08	7.27	6.16	4.44	4.46	4.45	**4.35**	4.89	4.98
8	7.60	8.02	7.20	6.01	4.18	4.20	4.22	**4.10**	4.58	4.68
9	7.37	7.96	7.19	6.09	4.18	4.24	4.19	**4.12**	4.66	4.79
10	7.48	7.66	7.07	5.88	4.01	4.02	4.06	**3.92**	4.33	4.49

ence of such noises: normalized least squares NLMS-L 3×3, ROM 3×3, and vector median rational hybrid VMRH 3×3. The developed RM filter specified by Eqs. (10), (14), and (15) was realized for various influence functions ψ. The results show that the ROM and VMRH filters better suppress noise and reconstruct small details when the intensity of impulsive noise is less than 5% or the intensity of multiplicative noise is less than 0.05. For other cases, the proposed filters provide a significant gain for processing.

6. The MM*K*NN and WM*K*NN algorithms proposed above were applied to process image sequences, including a video sequence of positron emission tomography (PET) with a rate of ten exposures per second. Each exposure had a size of 256×256 pixels and 256 intensity grades. The PET sequence contaminated with 20% impulsive noise was also processed by the WM 3×3, MMEM 3×3, TSM 3×3, and ACWM 3×3 filters, which were realized. The *PSNR* values presented in Table 2 show that the MM*K*NN and WM*K*NN filters suppress noise better than other filters. Table 3 presents similar results for another criterion corresponding to the quality of reconstructing small details in the image. In this case, the proposed filters have better criterion values than all other filters. In the last experiment, the Carphone and Miss America video sequences, which are often used in applications and have sizes 176×144 pixels, were contaminated with 20% impulsive noise and filtered. The results of their processing by various filters (Table 4) show that the

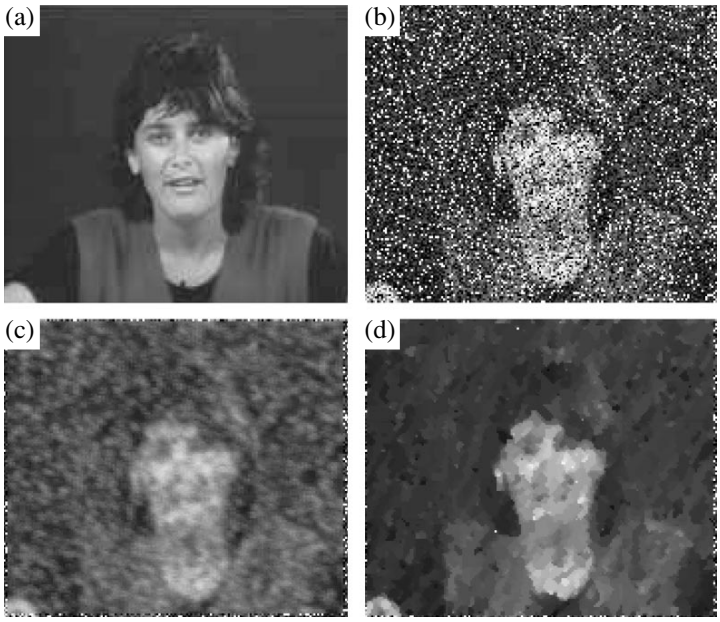

Fig. 1. Suppression of multiplicative and impulsive noise in the Miss America video sequence: (a) original image, (b) noisy image, (c) Frost filter, and (d) cascade Hampel filter.

MM*K*NN and WM*K*NN algorithms are preferable according to the *PSNR* and *MAE* criteria. The MM*K*NN, WM*K*NN, AM*K*NN, and MoM*K*NN filters can process 176×144-pixel sequences, improving their quality by suppressing noise and reconstructing small details at nearly the rate of a standard film, which is important for computer visualization. The Miss America video sequence contaminated with multiplicative and impulsive noise (Fig. 1) was processed by the Frost filter (Fig. 1c) and proposed cascade RM filter specified by Eqs. (10), (14), and (15) with the Hampel influence function (Fig. 1d). The visual results of processing show that the proposed filter ensures virtually on-line processing with better suppression of noise and reconstruction of small details.

Experimental investigations of new robust filtration algorithms provide the following conclusions.

(i) The proposed RM robust filters combine the properties of rank and M-estimates and can therefore efficiently suppress noise of various physical natures and reconstruct small details of images.

Table 4. Characteristics of the processing of noisy video sequences by various filters

Algorithm	Carphone			Miss America		
	PSNR	*MAE*	time	*PSNR*	*MAE*	time
WM	23.84	9.81	0.008	35.53	5.76	0.008
TSM	21.53	13.25	0.029	27.89	8.74	0.0219
ACWM	24.35	9.79	0.092	29.28	7.86	0.092
MMEM	23.61	11.11	0.016	28.11	7.056	0.016
LMMSE	24.16	10.05	0.030	30.72	7.158	0.0299
MM*K*NN, simple	24.59	9.27	0.042	33.087	5.993	0.045
MM*K*NN, truncated	24.77	9.084	**0.024**	36.99	4.293	**0.026**
MM*K*NN, Hampel	24.76	9.107	0.027	39.70	4.239	0.0292
WM*K*NN, simple	**24.78**	**9.084**	0.028	37.17	**4.136**	0.0307
WM*K*NN, truncated	24.08	9.47	0.055	**40.68**	4.663	0.0605
WM*K*NN, Hampel	24.02	9.47	0.031	35.58	4.806	0.0326

(ii) The cascade RM filter suppresses noise and reconstructs small details better than do other known filters.

(iii) The application of new algorithms to the filtration of video sequences of various types of images shows that these sequences can be processed on-line by a digital signal processor.

REFERENCES

1. A. A. Goncharenko, V. F. Kravchenko, and V. I. Ponomarev, *Remote Sounding of Heterogeneous Media* (Mashinostroenie, Moscow, 1991).
2. J. Astola and P. Kuosmanen, *Fundamentals of Nonlinear Digital Filtering* (CRC Press, New York, 1997).
3. A. Murat, *Digital Video Processing* (Prentice Hall, Upper Saddle River, NJ, 1995).
4. F. R. Hampel, E. M. Ronchetti, P. J. Rouseew, and W. A. Stahel, *Robust Statistics. The Approach Based on Influence Function* (Wiley, New York, 1986).
5. F. J. Gallegos-Funes, V. I. Ponomaryov, V. F. Kravchenko, and L. Nino-de-Rivera, Telecommun. Radio Eng. **56** (1), 67 (2001).
6. V. F. Kravchenko, V. I. Pustovoĭt, V. I. Ponomarev, and A. B. Pogrebyak, Dokl. Akad. Nauk **371**, 611 (2000) [Dokl. Phys. **45**, 149 (2000)].
7. V. F. Kravchenko, V. I. Ponomarev, V. I. Pustovoĭt, and L. Nino-de-Rivera, Dokl. Akad. Nauk **376**, 629 (2001) [Dokl. Phys. **46**, 97 (2001)].
8. V. F. Kravchenko, V. I. Ponomarev, and V. I. Pustovoĭt, Dokl. Akad. Nauk **380**, 189 (2001) [Dokl. Phys. **46**, 642 (2001)].
9. F. J. Gallegos-Funes, V. I. Ponomaryov, S. Sadovnychiy, and L. Nino-de-Rivera, Electron. Lett. **8** (15), 786 (2002).
10. H. Wei-Yu and L. Ja-Chen, Electron. Lett. **33** (2), 124 (1997).
11. T. Chen, K. Ma, and L. Chen, IEEE Trans. Image Process. **8** (12), 1834 (1999).
12. T. Chen and H. R. Wu, IEEE Trans. Signal Process. Lett. **8** (1), 1 (2001).

Translated by R. Tyapaev

Doklady Physics, Vol. 48, No. 6, 2003, pp. 303–305. Translated from Doklady Akademii Nauk, Vol. 390, No. 4, 2003, pp. 475–477.

TECHNICAL PHYSICS

Relaxation of Temperature Deformations in Carbon Fibers

O. V. Startsev*, D. A. Khristoforov*, A. B. Klyushnichenko*, A. F. Rumyantsev, G. M. Gunyaev**, and A. E. Raskutin****

Presented by Academician I.N. Frindlyander September 20, 2002

Received October 14, 2002

It is known that the best mechanical properties of polymer composite materials for constructional purposes are achieved by using carbon fibers to reinforce thermoplastic and thermosetting matrices [1]. It is commonly accepted that carbon fibers, in contrast to oriented aramide fibers, hold stable properties under extremely difficult operation conditions (mechanical loadings, moisture and corrosive media, radiation, elevated temperatures, thermal cycling, etc.) [1–3]. Nevertheless, instability is inherent in carbon fibers. Carbon fibers are produced by means of the thermal treatment of oriented polymer fibers [1, 3]. To ensure high elastic modulus, additional tensile stresses are applied in the process of thermal treatment. The structure and properties of such fibers are formed and stabilized in a field of mechanical stresses. Therefore, the heating of carbon fibers and related polymer composite materials is usually accompanied by shrinkage rather than by an increase in linear dimensions in the reinforcement direction [4–7].

It is structural nonequilibrium resulting from the production method that is responsible for the negative coefficient of linear thermal expansion (CLTE) of carbon fibers. It is usually assumed [2, 4] that the temperature deformations of carbon fibers are reversible, because fibers can retain the level of built-in nonequilibrium upon heating and cooling. However, this is not corroborated experimentally due to the insufficient sensitivity of measuring instruments (linear dilatometers) when investigating fibers with a low CLTE [4–7]. Therefore, reliable information concerning temperature deformations in carbon fibers after several thermal cycles is of particular interest.

For this reason, we precisely measured the thermal expansion of carbon fibers by using a specially designed linear dilatometer [8]. This instrument can continuously measure the length of a sample that is heated and cooled with a rate of about 1 K/min. The method used to monitor the absolute expansion makes it possible to reliably measure the CLTE of carbon fibers (consisting of bundles or bands) with an accuracy of 0.5×10^{-7} K^{-1}. In our experiments, variations in the length of the sample in five heating–cooling cycles between room temperature and 350–400°C were measured.

Typical examples of measurements are shown in Figs. 1 and 2. For comparison, the thermal strains of T-300JB, LZhU-35, and LU-24P carbon fibers, as well as unidirectional carbon plastics made of these fibers and a VS-2526 epoxy binder, are also shown [1]. Depending on the fiber type, production method, elastic modulus, and other factors, the thermal strains of fibers and carbon plastics are different in absolute value on the first heating to 350–400°C but have common negative sign.

The temperature strains of each fiber shown in Fig. 1 were measured in five heating–cooling cycles

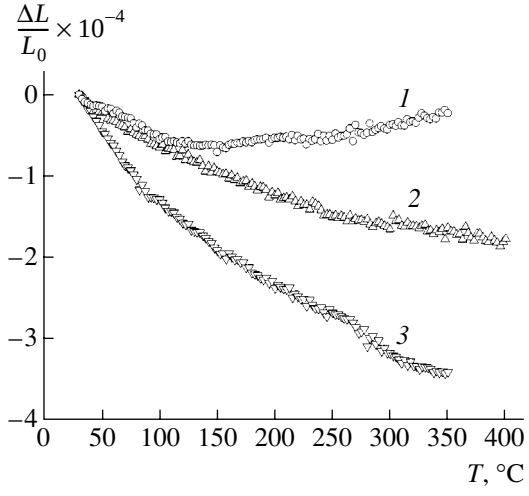

Fig. 1. Temperature dependence of the thermal strain of (*1*) T-300JB, (*2*) LZhU-35, and (*3*) LU-24P carbon fibers.

* *Research Institute of Ecological Monitoring, Altaĭ State University, pr. Lenina 61, Barnaul, 656099 Russia*
e-mail: starstev@phys.dcn-asu.ru, khristoforov.564@phys.dcn-asu.ru, klyushnichenko.564@phys.dcn-asu.ru

** *All-Russia Institute of Aviation Materials, ul. Radio 17, Moscow, 107005 Russia*
e-mail: admin@viam.ru

1028-3358/03/4806-0303$24.00

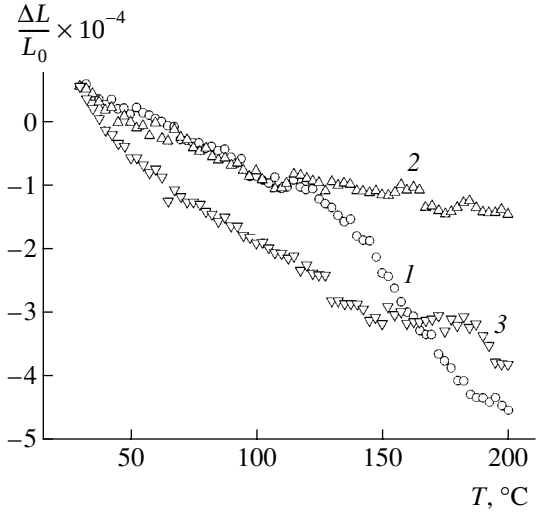

Fig. 2. Temperature dependence of the thermal strain of carbon plastics made of the VS-2526 binder and (*1*) T-300JB, (*2*) LZhU-35, and (*3*) LU-24P carbon fibers.

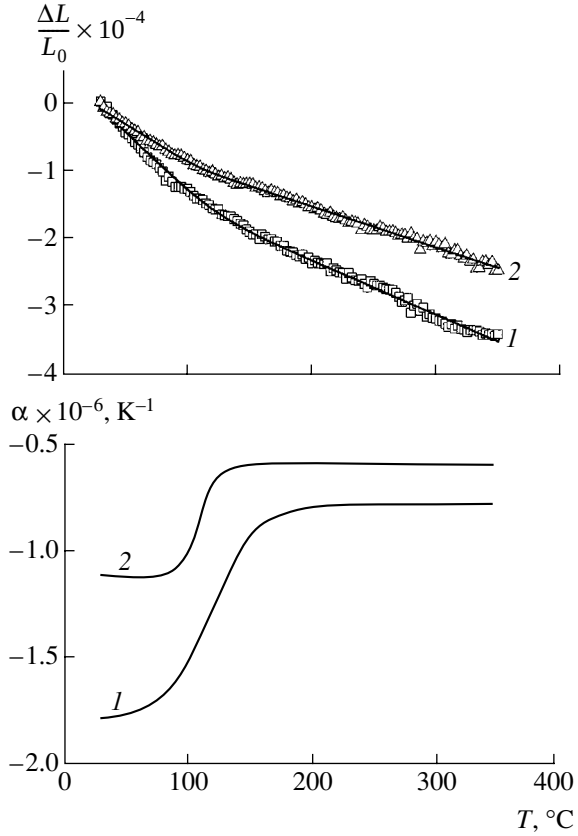

Fig. 3. Temperature dependences of the thermal strain and the coefficient of linear thermal expansion for the LU-24P carbon fiber in the (*1*) first and (*2*) fifth thermal cycling.

from room temperature to 350–400°C. As a result, we experimentally proved the instability of thermal expansion after several heatings. In all cases, with increasing number of thermal cycles, negative thermal strains decreased and the effect obviously exceeded possible experimental error. The effect is illustrated in Fig. 3, where the temperature dependences of the thermal strain and the CLTE of the LU-24P carbon fiber in the first and fifth cycles are shown.

Some quantitative results describing the effect of heatings on the thermal extension of fibers are listed in the table. It should be noted that the effect of decreasing temperature strains varies in the temperature range under investigation. For example, for the LU-24P fiber at a temperature of 50°C, the CLTE rises by 40%, whereas at 250°C, by 20%. In specific cases, e.g., for T-300JB fiber at 250°C, the CLTE changes its sign with an increase in the number of cycles but nevertheless increases. At the same time, the thermal gravimetric measurements showed that the sample masses remain unchanged after thermal cycling. Therefore, the results obtained are unrelated to the processes of thermal oxidation of fibers but corroborate the assumption that structural nonequilibrium relaxes in the process of thermal cycling.

Since only a few measurements were carried out, it is impossible to quantitatively estimate the effect. Therefore, additional measurements with variable amplitude and number of thermal cycles are of current interest. This is illustrated by the following final example. To estimate the serviceability of KMU-4l carbon-plastic specimens made of the LU-P fiber and ENFB binder under outer-space conditions, they were exposed for a long time in the open state on the surface of the Mir orbital space station. Detailed information on this experiment is available in [9, 10]. It was shown that,

Coefficients of linear thermal expansion on successive heatings of carbon fibers at temperatures 50 and 250°C

Fiber	CLTE, 10^{-7} K^{-1}									
	T = 50°C					T = 250°C				
	1	2	3	4	5	1	2	3	4	5
T-300JB	−6.1	−4.3	−4.2	−3.6	−3.2	1.0	2.5	2.9	4.3	4.6
LZhU-35	−7.5	−6.8	−6.6	−6.5	−6.0	−3.5	−3.0	−2.5	−2.2	−2.0
LU-24P	−18	−15	−14	−12	−11	−7.8	−6.6	−6.5	−5.6	−5.6

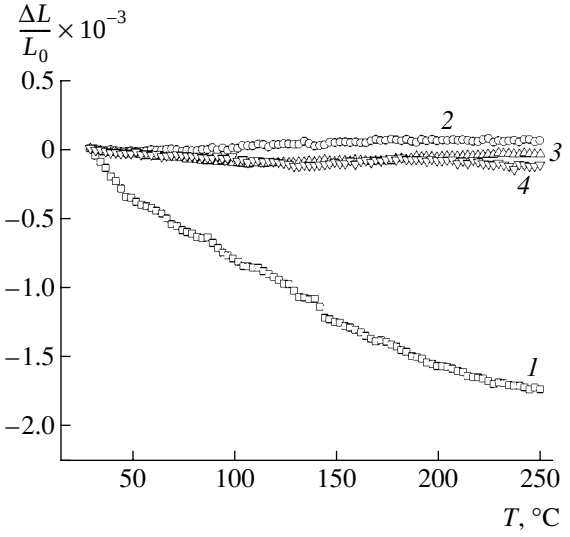

Fig. 4. Temperature dependences of the thermal strain of the KMU-4L carbon plastic (*1*) in its initial state and after exposure in the outer space for (*2*) 839, (*3*) 1024, and (*4*) 1218 days.

among all factors acting in near-Earth orbit, thermal cycling, where temperature varied between +125 and –100°C every 1.5 h, and a vacuum of about 10^{-4} Pa provided the most significant effect.

Figure 4 shows the temperature dependences of the thermal strain of the KMU-4l carbon plastic in the initial state and after exposure in outer space for 839, 1024, and 1218 days. It turned out that great number of thermal cycles (13000–19000) even for such a small amplitude causes significant relaxation of the carbon fiber. After thermal cycling in outer space, the specimens virtually lost the capability to be shortened with an increase in temperature. As was shown in [9, 10], the character of deformations in the KMU-4l carbon plastic in this example changed due to the modification of the properties of the fiber rather than the binder.

Thus, the above results prove that present high-modulus carbon fibers can reduce both the level of their structural nonequilibrium and their negative temperature strains in thermal cycling. This effect is of great importance in the forecasting of size stability of carbon-plastic elements designed to operate at variable temperatures.

REFERENCES

1. T. G. Sorina and G. M. Gunyaev, in *Polymer Matrix Composites*, Ed. by R.E. Shalin (Chapman & Hall, London, 1995), pp. 132–198.
2. G. E. Mostovoĭ, L. P. Kobets, and V. I. Frolov, Mekh. Kompoz. Mater., No. 1, 27 (1979).
3. L. I. Kalnin, Mekh. Kompoz. Mater., No. 3, 397 (1979).
4. K. E. Perepelkin and A. B. Geller, Mekh. Kompoz. Mater., No. 2, 350 (1980).
5. V. I. Vyshvanyuk, V. T. Alymov, and Z. N. Vishnevskiĭ, Mekh. Kompoz. Mater., No. 6, 1102 (1982).
6. M. R. Gurvich, O. V. Sbitnev, A. V. Sukhanov, and V. A. Lapotkin, Mekh. Kompoz. Mater., No. 1, 32 (1990).
7. A. V. Sukhanov, V. A. Lapotkin, V. Ya. Artemchuk, and L. A. Sobol', Mekh. Kompoz. Mater., No. 4, 599 (1990).
8. D. A. Khristoforov, A. B. Klyushnichenko, V. O. Startsev, *et al.*, in *Proceedings of II International Conference on Experimental Methods in Physics of Heterogeneous Condensed Media* (Altai Univ., Barnaul, 2001), Vol. 2, p. 186.
9. O. V. Startsev and E. F. Nikishin, Mekh. Kompoz. Mater., No. 4, 457 (1993).
10. O. V. Startsev, V. V. Issoupov, and E. F. Nikishin, Polym. Compos. **19** (1), 311 (1998).

Translated by Yu. Vishnyakov

Doklady Physics, Vol. 48, No. 6, 2003, pp. 306–308. Translated from Doklady Akademii Nauk, Vol. 390, No. 5, 2003, pp. 618–621.

TECHNICAL PHYSICS

Effect of Moisture on the Anisotropy of the Dynamic Shear Modulus of Glass-Reinforced Plastics

D. V. Filistovich[1], O. V. Startsev[1,*], A. A. Kuznetsov[1], A. S. Krotov[1], L. I. Anikhovskaya[2], and L. A. Dement'eva[2]

Presented by Academician I.N. Fridlyander September 20, 2002

Received October 14, 2002

INTRODUCTION

The application of polymer composites as construction materials in the aviation industry requires the comprehensive investigation of their mechanical properties. Moreover, variations in these properties under various external factors (heat and moisture actions, thermal cycling, irradiation, atmospheric aging, etc.) must be predicted. Variation in the anisotropy of the mechanical properties of sheet polymer composites is among the less studied aspects of external actions on these materials. In this paper, we study the moisture action on the anisotropy of the dynamic shear modulus of sheet glass-reinforced plastics used in aviation.

EXPERIMENT

We investigated samples of the KMKS-1.80.T-10 sheet glass-reinforced plastic based on adhesive prepregs [1, 2]. The material was developed at VIAM for the aviation industry.

To investigate the effect of moisture on the anisotropy of the mechanical properties of the material, we used 80×10-mm samples cut from a sheet of the glass-reinforced plastic at the angles 0°, 45°, 60°, and 90° to the principal reinforcement direction. All samples were divided into three identical sets and subjected to preliminary drying in an exsiccator at a temperature of 60 ± 2°C to stabilize their mass. Then, samples of the second and third sets were exposed to a humid environment with a relative humidity of 98 ± 2% at the same temperature until their moisture content reached its limiting value (2.5%). Then, the third-set samples were dried repeatedly. Moisture sorption and desorption in laminated plastics with allowance for both the effects of the cutting edge and nonequilibrium processes were simulated in detail in [1].

Original (preliminarily dried), moistened, and repeatedly dried samples were investigated by the method of dynamic mechanical analysis [3] with an automatic inverse torsion pendulum [4]. As a result, we obtained their dynamic shear modulus G' and mechanical-loss tangent $\tan\delta$ as functions of temperature.

RESULTS AND DISCUSSION

The dynamic mechanical analysis revealed a considerable plasticizing moisture action on the epoxy matrix of the material under investigation. For samples cut along the principal reinforcement direction, Figs. 1 and 2 show the temperature dependences of the dynamic shear modulus and mechanical-loss tangent,

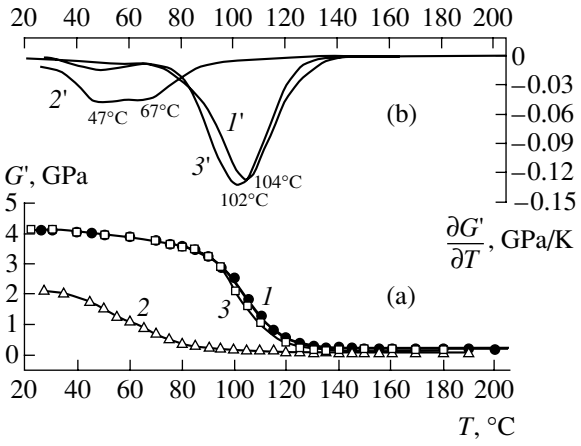

Fig. 1. Temperature dependence of (a) the dynamic shear modulus and (b) its temperature derivative for samples of the glass-reinforced plastic with 0° cutting angle (*1*) in the original state, (*2*) for a moisture content of 2.5%, and (*3*) after repeated drying. Temperatures at the minima are shown near the lines.

[1] *Altaĭ State University, pr. Lenina 61, Barnaul, 656099 Russia*

* *e-mail: rotary@barrt.ru*

[2] *All-Russia Institute of Aviation Materials (VIAM), ul. Radio 17, Moscow, 107005 Russia*

e-mail: admin@viam.ru

1028-3358/03/4806-0306$24.00 © 2003 MAIK "Nauka/Interperiodica"

when the glassy binder transforms to the high-elasticity state. Data of the dynamic mechanical analysis were processed by the method proposed in [5]. The vitrification temperature of the binder, which was determined by the minimum of the temperature derivative G', decreases by 36°C in the moistened state but is recovered after moisture desorption. The dynamic shear modulus after moistening at room temperature decreases by 31% from its initial value but is recovered after desorption. Reversibility of the plasticizing action of moisture is also corroborated by the temperature dependence of the mechanical-loss tangent: the peak corresponding to the binder vitrification temperature (to the α-transition [5]) in the $\tan\delta$ curve is shifted to lower temperatures after moisture sorption and recovers its position after moisture desorption (Fig. 2).

It is noteworthy that moistening is responsible for a two-stage relaxation transition in the temperature dependence of the dynamic shear modulus (Fig. 1) and transforms one peak in the temperature dependence of the mechanical-loss tangent into two pronounced maxima (Fig. 2). For the moistened epoxy matrix, one maximum of $\tan\delta$ is situated near 77°C and is associated with the mobility of kinetic segments interacting with water molecules. The second maximum is located near 115°C and corresponds to regions where water is desorbed during measurements for the dynamic mechanical analysis.

The two-stage variation in the temperature dependence of the G' parameter can be attributed to the same kinetic effect. Similar effects were observed in experiments with samples cut at different angles.

Thus, the results presented above prove that moisture absorbed by a glass-reinforced plastic plasticizes a binder. However, this effect is reversible in the glass-reinforced plastic based on adhesive prepregs. Similar results were obtained in [1, 2].

Figure 3 shows the temperature dependence of the dynamic shear modulus for original samples cut at various angles. This figure clearly shows that the behavior of the parameter G' is anisotropic. The virtually complete coincidence of the curves that correspond to cutting angles 0° and 90° with respect to the principal reinforcement direction can be attributed to the symmetry of the packing of reinforcing glass fibers.

To quantitatively describe the anisotropy of the dynamic shear modulus in a sample cut at the angle φ with respect to the principal reinforcement direction, we use the parameter $\xi = \frac{G'_{\max}}{G'_{\varphi}}$ proposed in [6]. Here, $G'_{\max}$ is the dynamic shear modulus in the sample cut at an angle such that G' is maximal. For the reinforcement pattern used in the glass-reinforced plastic under investigation, $G'_{\max} = G'_{45}$.

The temperature dependence of the anisotropy parameter ξ (Fig. 4), which is obtained by the dynamic mechanical analysis, shows that ξ in the glassy state of the binder (before its softening) is almost independent of temperature. In addition, the anisotropy of the moistened material is much larger than the anisotropy of both the original and repeatedly dried samples. In the region of the α transition (transition of the binder from the glassy state to the high-elasticity state), the anisotropy of the dynamic shear modulus also increases sharply. For all investigated cutting angles, maxima in the temperature dependences of the anisotropy of the dynamic shear modulus shift to lower temperatures when the material is moistened. When the sample is repeatedly dried, maxima recover their positions. This fact again illustrates the effect of the reversible plasticization of the epoxy binder under the action of moisture. Here, the two-stage character of softening of the binder under

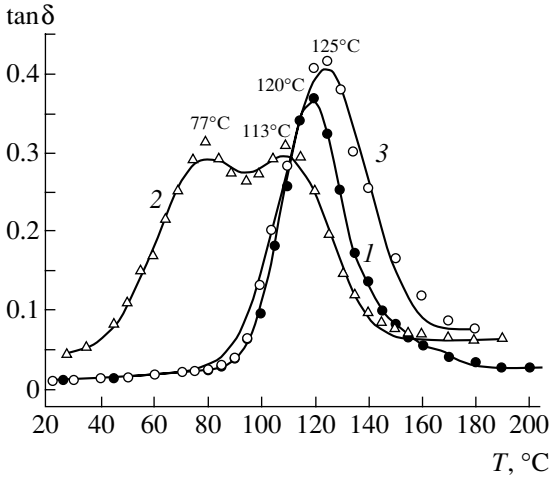

Fig. 2. Temperature dependence of the mechanical-loss tangent for samples of the glass-reinforced plastic with 0° cutting angle (*1*) in the original state, (*2*) for a moisture content of 2.5%, and (*3*) after repeated drying. Temperatures at the minima are shown near the lines.

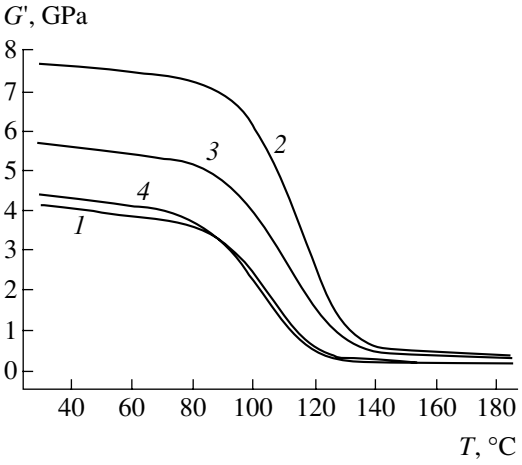

Fig. 3. Dynamic shear modulus versus temperature for the original samples of the glass-reinforced plastic, which were cut at angles (*1*) 0°, (*2*) 45°, (*3*) 60°, and (*4*) 90°.

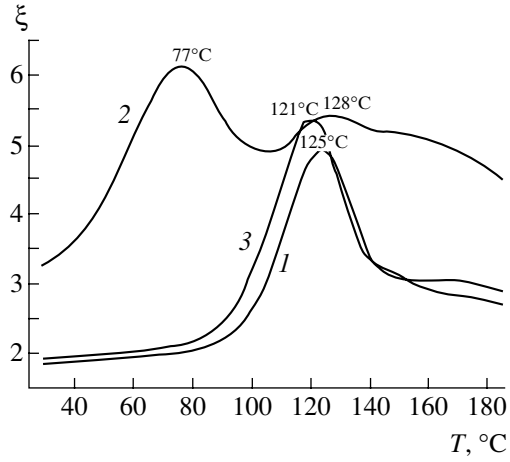

Fig. 4. Temperature dependence of the anisotropy parameter ξ for samples of the glass-reinforced plastic with 0° cutting angle (*1*) in the original state, (*2*) for a moisture content of 2.5%, and (*3*) after repeated drying. Temperatures at the minima are shown near the lines.

humidification is also pronounced. The second, less distinct, high-temperature peak is associated with the mobility of epoxy-binder macromolecules in sample regions, where water is desorbed during measurements with the torsion pendulum and heating of the sample at a rate of 1 K/min.

A common feature of the measurements conducted for four sorts of similar glass-reinforced plastics based on adhesive prepregs is that the parameter ξ is independent of temperature or depends on it only slightly in the region of the high-elasticity state of the binder. For example, Fig. 4 shows that the anisotropy of the dynamic shear modulus is approximately identical for both original and repeatedly dried samples in the temperature range 140–180°C. However, in the region of the high-elasticity state of the binder, the curves corresponding to the moistened samples lie higher, because moisture is not completely desorbed from samples during experiments even at temperatures 170–180°C. The moistened samples with the glassy binder contain much more moisture than the same samples after the binder's transition to the high-elasticity state. Nevertheless, the residual moisture noticeably affects anisotropy at higher temperatures, because the plasticizing action of moisture on the epoxy binder is much stronger in the high-elasticity state.

In the region of α transition, the temperature dependences of the anisotropy parameter ξ are similar for different samples (all curves have maxima) and fluctuate strongly (peak heights vary in a wide range from sample to sample). These fluctuations are probably caused by high sensitivity of the experimental procedure. Possible temperature gradients in the sample during experiments of the dynamic mechanical analysis with varying temperature affect the temperature dependence of the anisotropy of the dynamic shear modulus in the region of the α transition. The determination of the cause of these fluctuations requires additional measurements with new series of glass-reinforced plastics and analysis of their results.

Nevertheless, in the α-transition region of the binder, the characteristic temperatures in the temperature curves of the parameter ξ correlate well with the corresponding temperatures obtained by well-known methods [5, 6], where curves of the dynamic mechanical analysis are processed by spectrometric methods. The correlation dependence of the characteristic temperatures (extrema and inflection points corresponding to the α-transition region), which are determined by using the temperature curves of the parameter ξ and the temperature derivatives of the dynamic shear modulus G', is linear with the correlation coefficient $R^2 = 0.91$. Therefore, the maxima and inflection points in the temperature dependence of the anisotropy parameter ξ can be used as additional independent criteria when determining the vitrification temperature and boundaries of the α transition in anisotropic laminated polymer composites.

REFERENCES

1. O. V. Startsev, A. A. Kuznetsov, A. S. Krotov, *et al.*, Fiz. Mezomekh. **5** (2), 109 (2002).
2. A. A. Kuznetsov, in *Physics, Radiophysics: New Generation in Science* (Altai Univ., Barnaul, 2001), Vol. 2, pp. 57–61.
3. I. I. Perepechko, *Acoustic Methods for Investigating Polymers* (Khimiya, Moscow, 1973).
4. D. V. Filistovich, A. Ya. Suranov, and O. V. Startsev, in *Proceedings of 2nd International Conference on Experimental Methods in Physics of Heterogeneous Media* (Altai Univ., Barnaul, 2001), Vol. 1, p. 214.
5. O. V. Startsev, E. D. Sortyyakov, V. V. Isoupov, *et al.*, in *Experimental Methods in Physics of Heterogeneous Media* (Altai Univ., Barnaul, 1997), Vol. 1, p. 32.
6. O. V. Startsev and A. A. Kovalenko, Mekh. Kompoz. Mater. **35** (3), 201 (1999).

Translated by Yu. Verevochkin

Doklady Physics, Vol. 48, No. 6, 2003, pp. 309–313. Translated from Doklady Akademii Nauk, Vol. 390, No. 4, 2003, pp. 478–483.

MECHANICS

Experimental Investigation of Intermittency Modes in a Spherical Couette Flow

S. Ya. Gertsenshteĭn, D. Yu. Zhilenko, and O. É. Krivonosova

Presented by Academician G.G. Chernyĭ January 16, 2003

Received January 17, 2003

Experimental investigations of various scenarios of the transition from laminar to stochastic flow modes are extensively used to study turbulence. Scenarios whose development is accompanied by the formation of intermittency can be separated among typical scenarios of the transition to stochasticity. Intermittency means that the regular time behavior of a system is interrupted by intervals of the irregular behavior for the same values of controlling parameters [1]. As one of the controlling parameters increases, the average duration of the regular behavior of the system decreases, and the behavior of the system becomes completely chaotic at a certain value of this controlling parameter.

Intermittency can exist both in time (time alternation of periodic and aperiodic sections, when a detector is fixed in space) and in space (coexistence of laminar and turbulent sections in the flow structure) [2]. Both spatial and time intermittencies for boundary layers have been studied experimentally for a long time [2]. The possibility of the transition to chaos through time intermittency in confined hydrodynamic flows was experimentally corroborated for convection (see, e.g., [3]). For confined shear flows such as the Couette flow, spatial intermittency is determined from the structure of the surface layer of the flow [4]. Time or spatial intermittencies in the spherical Couette flow have not yet been observed.

Experimental investigations of the processes of space–time intermittency are very important particularly for three-dimensional flows, because comparison between regular and irregular parts of a time signal can apparently provide the basis for testing the methods of averaging used in calculations of turbulent flows.

In this work, we present the experimental results for intermittency modes in a spherical Couette flow, which is the shear flow arising in a viscid incompressible fluid between two spherical boundaries when the spheres rotate about a common axis. The flow in a spherical layer is determined by three characteristic parameters: relative thickness $\delta = \frac{r_2 - r_1}{r_1}$ of the spherical layer, where r_2 and r_1 are the radii of the outer and inner spheres, respectively, and two numbers $\mathrm{Re}_i = \frac{\Omega_i r_i^2}{\nu}$, where $i = 1$ and 2 for the inner and outer spheres, respectively; Ω_i is the angular velocity of the corresponding sphere; and ν is the kinematic viscosity of the fluid in the layer. Experiments were carried out in a wide spherical layer with relative thickness $\delta = 1.006$ while varying the two controlling parameters, Re_1 and Re_2, in the range $-950 < \mathrm{Re}_2 < -850$; negative Re_2 values correspond to the opposite direction of the rotation of the spherical boundaries.

The processes of the transition to stochasticity for the flow in a wide spherical layer were previously studied experimentally both for the rotation of only the inner sphere ($\mathrm{Re}_2 = 0$) [5, 6] and for the opposing rotation of the spherical boundaries ($-950 < \mathrm{Re}_2 < -700$) [7, 8]. In the latter case, it was shown that, for Re_2 fixed in the above range and for a quasistatic variation of Re_1, the transition to stochasticity occurs from the single-frequency periodic mode of the flow. The spatial structure of this periodic flow, which is called the mode of localized vortices, is symmetric about the equatorial plane and presents vortices that are located equidistantly in azimuth on both sides of the equator and are similar to open Taylor rings. The vortices are inclined to the equatorial plane and propagate in the direction of the outer-sphere rotation.

As excess over the critical value increases, a hard transition to chaos occurs with the breaking of the equatorial symmetry of the spatial flow structure. At the same time, as will be shown below, the scenarios of transition to stochasticity that were obtained in [7, 8] are not uniquely possible in the controlling-parameter range under consideration, because they can depend on the prehistory of the flow. The aim of this work is to analyze the possibility of obtaining intermittency modes in the spherical Couette flow and to determine the basic features of these flow modes.

Institute of Mechanics, Moscow State University, Michurinskiĭ pr. 1, Moscow, 117192 Russia

1028-3358/03/4806-0309$24.00

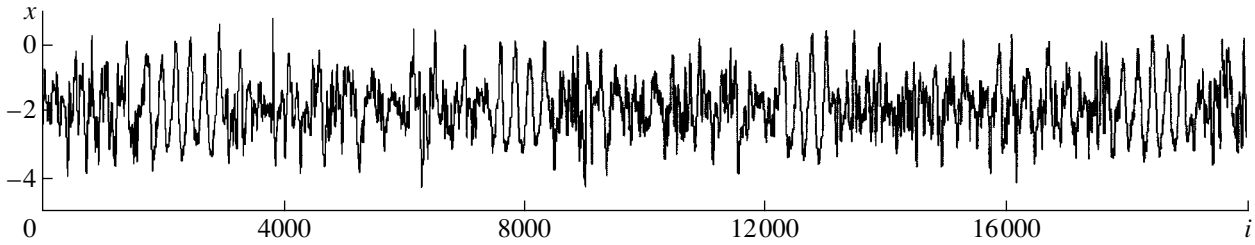

Fig. 1. Signal of velocity pulsations for $Re_1 = 429.6$ and $Re_2 = -900$, $\Delta i = 1000$ corresponds to 60 s.

Experiments were performed on a setup ensuring a spherical gap with the use of transparent concentric spheres 300 and 150 mm in diameter [9]. A transparent solution of silicon oils with a viscosity of about 50×10^{-6} m^2/s at 20°C was used as the working fluid. For the visualization of the flow, a small amount of an aluminum powder (less than 0.002 vol %) was added to the silicon oil, which held the optical transparence of the spherical layer. The pulsations of the flow velocity were measured by a laser Doppler anemometer (with the use of a 55L10 DISA photomultiplier and 1090 TSI signal processor). An analog signal from the exit of the signal processor was obtained with the cutoff of the constant component and removal of the low-amplitude high-frequency component whose frequency exceeds 3 Hz.

Measurements were carried out at a point spaced by 120 mm from the rotation axis of the spheres. The measured projection of the velocity lies in the plane that is parallel to the equatorial plane and spaced from it by 75 mm. The results of measurements are discrete samples of an analog signal, which have a length of 2^{15}–2^{16} points and are obtained with an interval of 0.06 s. All measurements were carried out under the stationary conditions for constant (with a relative deviation of 0.05% or less) rotation velocities of the spheres and constant temperatures in the layer. The transition from the zero initial conditions to each of the modes under consideration was made as follows. The required velocity of the outer sphere was established for the fixed inner sphere ($Re_1 = 0$), and then the rotation velocity of the inner sphere was varied at a constant Re_2 value.

To avoid the effect of the acceleration of the inner sphere, the method of so-called quasistatic variation of its rotation velocity was previously used [7, 8]. In this case, near the region of the transition from one flow mode to another, the rotation velocity of the inner sphere is changed by a small value with acceleration $\frac{\Delta Re_1}{Re_1} < 0.1\%$ per second. Then, the rotation velocity holds constant during 15 min or longer. In this scheme, the change in the inner-sphere acceleration (when this quantity is below the threshold value) does not affect the results, which was pointed out in previous experiments on studying transitions to chaos in a cylindrical Couette flow [4].

The method of the acceleration of the inner sphere in that work is different than the method described above. Once the mode of localized vortices is established, the rotation velocity of the inner sphere varies continuously to the given values, with the acceleration lying in the range $0.3 < \frac{\Delta Re_1}{Re_1} < 0.5\%$ per second. The method of experimentally determining the time of transient processes accompanying the change in Re_1 with a nonzero acceleration was developed. To this end, the signal of velocity pulsations was continuously recorded when Re_1 is varied: first, at the Re_1 value corresponding to the mode of the flow of localized vortices, second, in the process of variation from Re_1 to $Re_1 + \Delta Re_1$ ($\Delta Re_1 < 5$), and finally, at $Re_1 + \Delta Re_1$. The Fourier transform for the time-record section corresponding to the $Re_1 + \Delta Re_1$ flow mode can exhibit the presence of two close frequencies (corresponding to Re_1 and $Re_1 + \Delta Re_1$, respectively). Owing to the shift of the constant-length time section from the termination of the process of varying Re_1, only the second frequency remains in the spectrum, and the value of this shift corresponds to the duration of the transient process. The application of this method indicated that the transient process is 12 min or less.

The results of measurements indicate that the equatorial symmetry of the spatial structure of the flow under the rapid change in Ω_1 is broken at the same Re_1 values as those previously obtained in [7, 8]. However, the qualitative shape of the velocity signal can be fundamentally different: regular sections can be observed in the signal, while the signal became completely irregular in previous experiments reported in [7, 8]. The signal of pulsations from the analog exit of a TSI laser Doppler anemometer is shown in Fig. 1, where intermittency—the time alternation of periodic and aperiodic sections for the same boundary conditions of the flow—is pronounced. In this case, different sections of the time record correspond to different spatial structures. Namely, time-periodic sections correspond to the azimuth-periodic spatial structure that presents localized vortices observed previously before the transition to chaos for the quasistatic change in the Re_1 number [7, 8], while time-aperiodic sections correspond to irregular spatial structures.

We emphasize that the spatial structure of the flow with intermittency in both periodic and aperiodic sections of the signal depends on the direction of the variation of Re_1.

As Re_1 decreases in the aperiodic section, the flow structure involves short-term intervals of formation and decay of vortices localized near the inner sphere; the flow is most irregular near the inner sphere. As Re_1 increases, small-scale structures expand over the entire width of the spherical layer.

For any direction of Re_1 variation in periodic sections of the signal, the mode of localized vortices is symmetric about the plane parallel to the equator. However, this symmetry plane is slightly shifted above and below the equator with a decrease and increase in Re_1, respectively. This asymmetry can be attributed to the effect of the suspension of the inner sphere. The shift of the symmetry plane of spatial structures from the equatorial plane for a rapid change in the rotation velocity of the inner spherical boundary at $Re_2 = 0$ was previously observed in a layer of relative thickness $\delta = 0.154$ [10].

Experiments indicated that, to obtain reproducible characteristics of intermittency, it is necessary to ensure a certain sequence of changes in the controlling parameters: first, the mode of localized vortices must be established by quasistatically varying the controlling parameters (as was done in [7, 8]); then, it is necessary to rapidly vary Re_1 to the Re_{1h} value corresponding to the transition to chaos for a quasi-static variation of Re_1 and hold the parameters of the flow constant for 40 min or longer. After the appearance of intermittency, one can quasistatically vary Re_1 to the necessary value and conduct measurements. All the data below were obtained by this method of varying Re_1.

In this work, intermittency modes were observed in the Re_2 range from –870 to –950, and the most complete data were obtained for $Re_2 = -900$. Figure 2 shows the various characteristics of intermittency for this Re_2 value.

Time intermittency is characterized by the average duration $\langle l \rangle$ of the laminar phase and by the time-signal type [1, 3]. The average duration of the laminar phase is the ratio of the total length of laminar sections to the total length of the record. Figure 2a shows $\langle l \rangle$ as a function of Re_1 and direction of its variation. Line *1* in Fig. 2 corresponds to the boundary of intermittency appearance, which coincides with the boundary of the transition to the completely irregular mode of the flow for a quasistatic increase in Re_1. With the increase in Re_1, the total duration of periodic sections decreases, and the flow becomes completely stochastic for $Re_1 > 432$ (line *2* is the boundary of the intermittency existence region with an increase in Re_1). As Re_1 decreases, intermittency is observed to the left of line *1* until the lower boundary of the hysteresis region of the mode of localized vortices, which was obtained in [8] for a quasistatic variation of Re_1 (line *3*) and thus coincides with the lower boundary of the intermittency hysteresis.

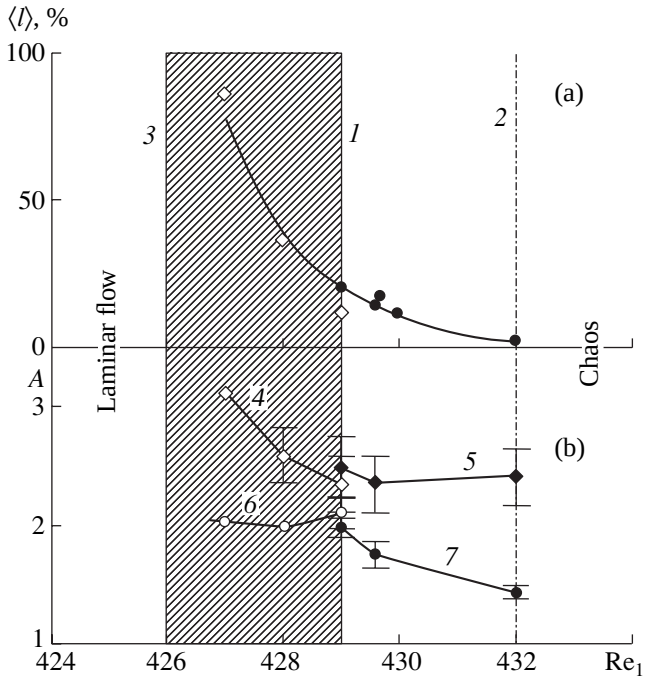

Fig. 2. Intermittency parameters for $Re_2 = -900$: (a) average duration of the laminar mode and (b) relative amplitude of velocity pulsations. Open and closed symbols correspond to an increase and decrease in Re_1, respectively. The region of the intermittency-mode hysteresis is shaded.

The signal from the laser Doppler anemometer that was observed in the experiment (Fig. 1) enables one to easily distinguish between time-periodic and time-aperiodic sections of the flow. For the time intermittency considered in this work, all spectra of aperiodic sections for all values and directions of Re_1 variation involve 3 to 15 discrete peaks above the noise level in the range from 0.001 to 0.2 Hz. All peaks can be represented in the form of a linear combination of two independent frequencies (f_1 and f_2 in Fig. 3) within the accuracy of data processing. These frequencies differ from the frequency f_p characteristic for periodic sections. Thus, irregular sections of the intermittency mode are quasiperiodic in a certain sense. The independent frequencies f_1 and f_2 are virtually independent of Re_1. As excess above the critical value increases, the number of peaks at combination frequencies in the spectrum increases, and amplitudes of these peaks also increase.

The noise levels for periodic and aperiodic sections of the signal differ from each other by more than two orders of magnitude (Fig. 3). We emphasize that all the above qualitative characteristics of the spectra of irregular sections of the flow completely correspond to the properties of the spectrum of the chaotic mode obtained previously in [7] for a quasistatic variation of Re_1. The spectrum of periodic sections includes one frequency with higher harmonics (the peak at frequency f_{mod} corresponds to the amplitude modulation of the instruments), and the ratio of the amplitudes of peaks at the

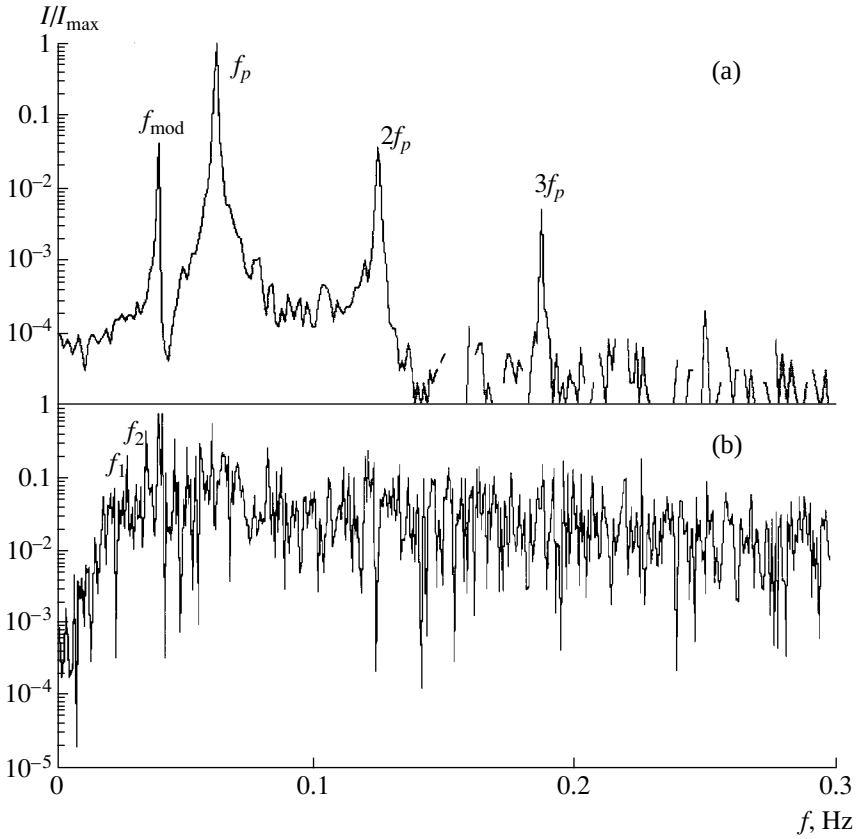

Fig. 3. Spectra of (a) periodic (Re_1 = 426, Re_2 = –900, and Re_1 decreases) and (b) aperiodic (Re_1 = 432, Re_2 = –900, and Re_1 increases) sections of the time record of the intermittency mode.

fundamental frequency f_p and second harmonic $2f_p$ is constant.

The relations between periodic and irregular parts of the signal, which were determined experimentally, provide the assumption that the observed transition to stochasticity can be attributed to intermittency between the regular periodic and irregular quasiperiodic modes of the flow. Similar transitions to stochasticity, which were also accompanied by hysteresis, were observed previously in radio physics systems [11].

Figure 2 shows the relative amplitude of velocity pulsations as a function of Re_1 for various signal sections and different directions of varying Re_1. The relative amplitude is determined as

$$A = \frac{\bar{x}}{\sigma}, \quad \bar{x} = \frac{1}{N}\sum_{i=1}^{N} x_i,$$

$$\sigma^2 = \frac{1}{N-1}\sum_{i=1}^{N} (x_i - \bar{x})^2,$$

where x_i is the instantaneous value of the measured velocity projection and N is the sample length.

It is seen that the increase in the relative amplitude in the transition to chaos, which is well known from the results of numerical calculations (see, e.g., [12]), exists in the entire range of existing intermittency modes (lines *4* and *5* in Fig. 2, which were calculated for irregular sections of the signal, lie above lines *6* and *7*, calculated for periodic sections of the signal). The behaviors of the relative amplitude with varying Re_1 are different for the chaotic and periodic sections of the signal. As Re_1 decreases, the relative amplitude of periodic sections (line *6*) is virtually constant, while the relative amplitude for chaotic sections (line *4*) increases by 30% or more. As Re_1 increases, the relative amplitude of chaotic sections (line *5*) is constant, and the relative amplitude of laminar sections (line *7*) decreases. The difference between the relative amplitudes for periodic and aperiodic sections is maximal at the boundaries of the region of intermittency existence (lines *2* and *3*) and is minimal at the boundary of the transition to chaos for a quasistatic increase in Re_1 (line *1*).

The discrepancy between the amplitudes and compositions of the spectra of velocity pulsations for periodic and aperiodic sections testifies to the presence of transient processes when a periodic section of the flow changes to an irregular one and vice versa. It is difficult to identify these transient processes directly in the record of the signal (Fig. 1). Since the most pronounced differences between laminar and chaotic modes are

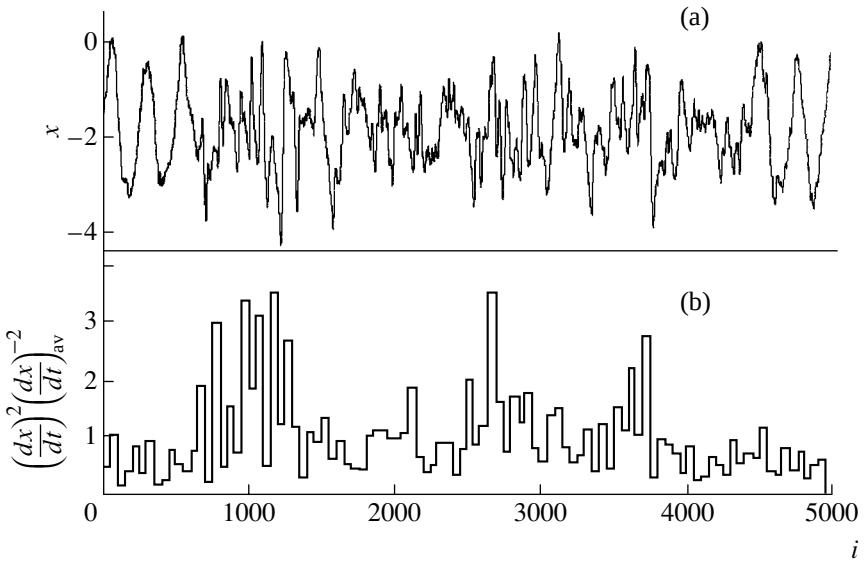

Fig. 4. Dissipation of the kinetic energy as a characteristic of transient processes from regular to irregular sections of the intermittency mode.

associated with different levels of dissipation of the kinetic energy of the flow, these transient processes can be revealed in the time dependence of local dissipation.

Local dissipation in turbulent flows has not yet been directly measured. To indirectly determine this quantity in experiment, Meneveau and Sreenivasan [13] suggested using the velocity derivative squared $\left(\frac{\partial x_i}{\partial t}\right)^2$ normalized to its average value. Figure 4a shows the part of the signal record from the laser Doppler anemometer with two transitions: from a periodic to irregular section and vice versa. Figure 4b shows the time dependence of the normalized velocity derivative squared (finite-difference approximation of the time derivative with further averaging over 50 points is used).

It is seen that the onset of the chaotic section is accompanied not only by an increase in the maximum amplitude of local dissipation but also by further oscillation variations in amplitude. It is notable that the composition of the spectrum of the local dissipation amplitude in all regular sections of the time record coincides with the spectrum of the original signal. The same behavior is observed for some irregular sections of the time record, which can provide the selection of coherent structures in chaotic flows.

Thus, a rapid variation of Re_1 is shown to be responsible for a new scenario of the transition to chaos, and this scenario is characterized by the presence of intermittency between regular periodic and irregular aperiodic modes. This scenario is accompanied by hysteresis whose boundaries coincide with the boundaries of the hysteresis of the chaotic mode obtained in [8] for a quasistatic variation of Re_1. We emphasize that all the above characteristics of intermittency belong to only one way of varying Re_1 that is considered in this work.

REFERENCES

1. Y. Pomeau and P. Manneville, Commun. Math. Phys. **74** (2), 189 (1980).
2. A. V. Boĭko, G. R. Grek, A. V. Dovgal', and V. V. Kozlov, *Occurrence of Turbulence in Pariental Flows* (Nauka, Novosibirsk, 1999).
3. M. Dubois, M. A. Rubio, and P. Berge, Phys. Rev. Lett. **51** (16), 1446 (1983).
4. C. D. Anderec, S. S. Liu, and H. L. Swinney, J. Fluid Mech. **164**, 155 (1986).
5. Yu. N. Belyaev and I. M. Yavorskaya, Izv. Akad. Nauk SSSR, Mekh. Zhidk. Gaza, No. 1, 10 (1991).
6. Yu. N. Belyaev, Prikl. Mekh. Tekh. Fiz., No. 1, 64 (1995).
7. S. Ya. Gertsenshteĭn, D. Yu. Zhilenko, and O. É. Krivonosova, Dokl. Akad. Nauk **375**, 770 (2000) [Dokl. Phys. **45**, 697 (2000)].
8. S. Ya. Gertsenshteĭn, D. Yu. Zhilenko, and O. É. Krivonosova, Izv. Akad. Nauk, Mekh. Zhidk. Gaza, No. 2, 56 (2001).
9. Yu. N. Belyaev, A. A. Monakhov, and I. M. Yavorskaya, Izv. Akad. Nauk SSSR, Mekh. Zhidk. Gaza, No. 2, 9 (1978).
10. K. Buhler, Acta Mech. **81**, 3 (1990).
11. V. S. Anishchenko, *Complex Oscillations in Simple Systems: The Mechanism of Occurrence, Structure and Characteristics of Dynamic Chaos in Radiophysic Systems* (Nauka, Moscow, 1990).
12. N. V. Nikitin, Izv. Akad. Nauk, Mekh. Zhidk. Gaza, No. 6, 14 (1994).
13. C. Meneveau and K. Sreenivasan, J. Fluid Mech. **224**, 429 (1991).

Translated by R. Tyapaev

Doklady Physics, Vol. 48, No. 6, 2003, pp. 314–318. Translated from Doklady Akademii Nauk, Vol. 390, No. 5, 2003, pp. 622–626.

MECHANICS

"Smallness" and Asymptotic Smallness of Dimensional Parameters in Problems of Mechanics

L. D. Akulenko* and D. V. Georgievskiĭ**

Presented by Academician V.V. Kozlov January 28, 2003

Received January 28, 2003

In many problems of nonlinear mechanics, the equations of motion (or state) cannot be reduced to a completely dimensionless form by using only the parameters of a system [1–4]. In these cases, it is impossible to introduce small numerical parameters characterizing the relative smallness of the terms taken into account in equations. The introduction of such parameters is usually of primary interest in physics and mechanics, when the effect of various perturbing factors is investigated. The equations of perturbed motion (or state) will involve so-called dimensional parameters, whose specific (in particular, zero) values correspond to the known generating solution. The application of the standard perturbation method leads to an apparent difficulty associated with the proper choice of units of measure for the above parameters. However, since terms that are compared when expanding solutions and operators have the same units of measure, dimensional parameters can be properly used to determine and include perturbing factors with the required relative or absolute errors. In particular, in comparatively scarce cases, where numerical parameters are introduced, actual difficulties appear due to both the irregular behavior of other (not small) parameters and the absence of the physical meaning of the generating problem.

In this study, we describe a perturbation procedure for solving a class of nonlinear problems in mechanics. The procedure is based on introducing an artificial small parameter (intermediate asymptotic behavior [3, 4]) to construct a solution with the required accuracy.

1. We consider a nonlinear initial–boundary value problem in mechanics. It can be written in the operator form

$$A[z] + \omega B[z] = 0, \qquad (1)$$

where $z = z(\mathbf{x}, t)$ is an unknown function that can be vector or tensor; $\mathbf{x} \in D$ is the vector coordinate; t is the time, $0 \le t \le T < \infty$; A and B are sufficiently smooth nonlinear operators, which specify the equations in a domain and the boundary and initial conditions; and ω is a dimensional parameter that, for brevity, does not enter into the expressions for A and B [5, 6].

Let the characteristic geometric physicomechanical parameters of the system, on which the A and B operators depend, be unable to form a combination Ω with the unit of measure of ω. In other words, a basis composed of any characteristic quantities excluding ω is incomplete; i.e., it is impossible to represent ω in dimensionless form and to introduce a so-called small numerical parameter $\varepsilon = \dfrac{\omega}{\Omega} \ll 1$.

Let problem (1) for $\omega = 0$ have a known solution z_0:

$$A[z_0(\mathbf{x}, t)] = 0, \quad z_0 \not\equiv 0. \qquad (2)$$

Then, there appears the problem of the asymptotic representation of the solution $z(\mathbf{x}, t, \omega)$ of problem (1) near $z_0(\mathbf{x}, t)$ for $\omega \longrightarrow 0$. As is known, the smaller the asymptotic parameter, the closer the finite sum of the corresponding asymptotic series (e.g., in the Poincaré sense) to the sum of the entire series. However, in this case, the parameter ω is dimensional, and its smallness is meaningless.

Nevertheless, we introduce a certain artificial dimensionless parameter τ, which has not yet related to the original mechanical system, and perform an asymptotic expansion in terms of this parameter:

$$z = z(\mathbf{x}, t, \omega) = z_0(\mathbf{x}, t) + \sum_{n=1}^{\infty} \tau^n z_n(\mathbf{x}, t, \omega, \tau) \equiv z_0 + Z. \qquad (3)$$

According to the formulation of problem (1), which does not involve τ in an explicit form, both the functions z and Z are independent of this parameter. Substituting representation (3) into Eq. (1) and assuming that

* *Institute for Problems in Mechanics, Russian Academy of Sciences, pr. Vernadskogo 101-1, Moscow, 119526 Russia*

** *Moscow State University, Vorob'evy gory, Moscow, 119899 Russia*
e-mail: georgiev@mech.math.msu.su

1028-3358/03/4806-0314$24.00

the A and B operators are sufficiently smooth, we arrive at the relation

$$\sum_{n=1}^{\infty} A_n[z_0]Z^n + \omega B[z_0] + \omega\sum_{n=1}^{\infty} B_n[z_0]Z^n = 0, \quad (4)$$

where the A_n and B_n coefficients are expressed in terms of the Freshet derivatives of the A and B operators [5, 6]. To meet operator equation (4), the following chain of equalities—a sequence of coupled equations for the unknowns z_n—is proposed:

$$A'[z_0]z_1 + \frac{\omega}{\tau}B[z_0] = 0,$$

$$A'[z_0]z_2 + \frac{1}{2}A''[z_0]z_1^2 + \frac{\omega}{\tau}B'[z_0]z_1 = 0, \quad (5)$$

$$A'[z_0]z_n + \Delta A_n + \frac{\omega}{\tau}\Delta B_n = 0, \quad n \geq 1.$$

The operator expressions ΔA_n and ΔB_n are defined in terms of the functions $z_0, z_1, \ldots, z_{n-1}$ and have the corresponding structure in powers of these coefficients, which are assumed to be found recurrently from the linear inhomogeneous equations at the preceding steps.

Next, we assume that the linear operator $A'[z_0]$ in Eqs. (5) has the unique continuous inverse operator $(A')^{-1}$; i.e., the equation $A'[z_0]y = 0$ has the unique solution $y(\mathbf{x}, t) \equiv 0$ (the operator A is nonsingular). Then, the unknown quantities z_n ($n \geq 1$) are uniquely determined from the sequence of Eqs. (5):

$$z_1 = -\frac{\omega}{\tau}(A')^{-1}[z_0]B[z_0] \equiv \frac{\omega}{\tau}Y_1[z_0],$$

$$z_2 = \left(\frac{\omega}{\tau}\right)^2 Y_2[z_0],$$

$$Y_2 = -(A')^{-1}[z_0]\left(\frac{1}{2}A''[z_0]Y_1^2 + B'[z_0]Y_1\right), \ldots, \quad (6)$$

$$z_n = \left(\frac{\omega}{\tau}\right)^n Y_n[z_0].$$

The conditions of relative smallness and decrease in each subsequent term $\tau^n z_n$ in series (3) can be provided by, for example, a sufficient smallness of the numerical parameter $\tau > 0$ and by decreasing the dimensional parameter ω so that the coefficients z_n are nonincreasing. The substitution of Eqs. (6) into Eq. (3) gives the expression

$$z(\mathbf{x}, t, \omega) = z_0(\mathbf{x}, t) + \sum_{n=1}^{\infty} \omega^n y_n(\mathbf{x}, t), \quad (7)$$
$$y_n \equiv Y_n[z_0],$$

which is a power expansion in terms of ω. The convergence of series (7) or the corresponding procedure of successive approximations for $|\omega| \leq \omega_0$ is substantiated by using the theorems on an implicit function and a contraction operator. This is a separate mathematical problem [5, 6].

2. Thus, the above procedure of constructing an approximate solution provides a meaning to the notion of "small dimensional parameter" ω. In essence, the "smallness" of ω means that each term in the series is much smaller than the preceding terms, in particular, $\omega^n\|y_n\| \gg \omega^{n+1}\|y_{n+1}\|$, i.e., $\omega\|y_{n+1}\| \ll \|y_n\|$. Only the first approximation is usually constructed in applications. In this case,

$$\omega\left\|(A')^{-1}[z_0]B[z_0]\right\| \ll \|z_0(\mathbf{x}, t)\|, \quad z_0 \neq 0. \quad (8)$$

This procedure can be applied even when $z_0 \equiv 0$. In this case, the terms y_1 and ωy_2 and so on are compared. In addition, the procedure can be used in the absence of the parameter ω. In this case, it is necessary to satisfy the strong inequalities $\|y_n\| \gg \|y_{n+1}\|$. The parameter ω can also appear in a more complicated way, for example, $B = B[z, \omega]$ ($\|B\| \longrightarrow 0$, $\|\omega\| \longrightarrow 0$). Moreover, it can be a functional or an operator [7].

We note that the mathematical analysis of perturbed operator equations is independent of the units of measure [5, 6].

Thus, the artificial introduction of the dimensionless asymptotic parameter τ (intermediate asymptotic behavior [3, 4]) made it possible to expand the function $z(\mathbf{x}, t, \omega)$ into an asymptotic series in terms of a dimensional quantity ω that cannot be represented in the dimensionless form in this problem. The resulting solution given by Eq. (7) is independent of τ. Therefore, the procedure described above is auxiliary. Thus, the notions smallness and asymptotic smallness are not identical in application to the dimensional parameter ω.

The introduction of a fictitious dimensionless parameter will be exemplified below in Sections 3 and 4.

3. We consider a Cauchy problem for a scalar variable z, $A = \dfrac{d^N}{dt^N}$, $B = z^2 - 1$ ($N = 1, 2, \ldots$), and with zero initial conditions. Let t be dimensional time such that $\omega > 0$ is measured in the $[t]^{-N}$ unit and the variable z is dimensionless. Since the problem involves no characteristic parameters, it is possible to use the procedure

described in Sections 1 and 2 and to find the unknown solution in the asymptotic-expansion form

$$z_{2j} \equiv 0, \quad z_{2j+1} = \left(\frac{\omega}{\tau}\right)^{2j+1} y_{2j+1}(t^N, N),$$

$$j = 0, 1, 2, \ldots,$$

$$y_1 = \frac{t^N}{N!}, \quad y_3 = -\frac{(2N)!t^{3N}}{(N!)^2(3N)!}, \tag{9}$$

$$y_5 = 2\frac{(2N)!(4N)!t^{5N}}{(N!)^3(3N)!(5N)!}, \ldots,$$

$$z(t, \omega, N) = \omega y_1 + \omega^3 y_3 + \omega^5 y_5 + \ldots.$$

In particular, series (9) for $N = 1$ can be summed in the closed form: $z(t, \omega) = \tanh \omega t$; for $N = 2$, it is an expansion of an elliptic function.

Let us consider a model problem of the one-dimensional motion of a body with mass m in a stratified medium with quadratic resistance under the action of a constant force F:

$$m\ddot{z} = F - k\left(\frac{z}{h}\right)|\dot{z}|\dot{z}, \quad z(0) = z^0, \quad \dot{z}(0) = v^0. \tag{10}$$

Here, $k > 0$ is the variable coefficient and $h > 0$ is the stratification parameter. Cauchy problem (10) is solved in quadratures, but the analysis of the solution is difficult.

For definiteness, we take the case where $v^0 = 0, F \geq 0$, and $k = k_0 \exp\left(\pm\frac{z}{h}\right)$ (exponential stratification). After the division of both sides of Eq. (10) by $m > 0$, the problem is written in the form of Eq. (1):

$$\ddot{z} + \lambda|\dot{z}|\dot{z}\exp\left(\pm\frac{z}{h}\right) - g = 0, \quad z(0) = z^0, \quad \dot{z}(0) = 0, \tag{11}$$

where $\lambda = \frac{k_0}{m}$ and $g = \frac{F}{m}$. Depending on the aim of investigation, one can consider various limiting cases for the dimensional parameters λ, h, g, and z^0.

Let $g = \omega$ be an asymptotically small quantity [the operator B in Eq. (1) is the multiplication by –1]. The remaining parameters λ, h, and z^0 of problem (11) cannot form a characteristic time unit. The unknown z can be represented in dimensionless form by these three parameters, but this is unnecessary. The desired approximate solution is uniquely constructed by the procedure described in Sections 1 and 2 in the form

$$z(t, g) = z_0 + gy_1 + g^2 y_2 + g^3 y_3 + \ldots,$$

$$z_0 \equiv z^0, \quad y_1 = \frac{1}{2}t^2,$$

$$y_2 = -\frac{\eta}{12}t^4, \quad y_3 = \frac{\eta}{180}\left(4\eta \mp \frac{3}{h}\right)t^6, \ldots, \tag{12}$$

$$\eta = \lambda \exp\left(\pm\frac{z^0}{h}\right).$$

The mechanical meaning of any term in expansion (12) is quite obvious. These terms, sequentially in powers of the dimensional parameter g, present the effect of the applied force on the motion of the body in the stratified medium.

Now, we consider problem (11) in the other extreme case

$$\frac{1}{h} = \omega \longrightarrow 0, \quad \lambda = \mu\omega \longrightarrow 0, \quad z(0) = 0, \quad \dot{z}(0) = 0. \tag{13}$$

Here, $\mu \sim 1$ is a certain number and ω is a quantity inverse to length. Conditions (13) correspond to a weakly stratified medium and a low resistance coefficient. The only characteristic parameter of the problem is acceleration g; the time and length scales are absent. The desired approximate solution of the problem specified by Eqs. (11) and (13) is constructed similarly to solution (12):

$$z(t, h) = z_0 + \frac{y_1}{h} + \frac{y_2}{h^2} + \ldots, \quad z_0 = \frac{1}{2}gt^2,$$

$$y_1 = -\frac{1}{12}\mu(gt^2)^2, \quad y_2 = \frac{\mu}{180}(4\eta \mp 3)(gt^2)^3, \ldots. \tag{14}$$

An expansion [e.g., given by formulas (7), (9), (12), and (14)] of the solution in terms of the parameter ω is unique regardless of intermediate normalizations.

4. As the generating problem specified by Eq. (2), we consider the problem of the stationary flow of a viscous incompressible fluid in a plane confusor (the Jeffery–Hamel problem) [1, 2]. This problem involves four characteristic parameters: the opening angle of a confusor 2β, the inflow–outflow intensity Q, the fluid density ρ, and its dynamic viscosity μ. In what follows, the variables characterizing the flow are marked by the superscript "$\circ$." These are the velocity field $\mathbf{v}^\circ$, the field of the deformation-rate tensor $\underset{\sim}{v}^\circ$, the stress-deviator field $\underset{\sim}{s}^\circ$, and the pressure field p°. The maximum shear stress and the maximum sliding velocity, which are the quadratic invariants of the tensors $\underset{\sim}{s}^\circ$ and $\underset{\sim}{v}^\circ$, are denoted by T° and U°, respectively.

Based on the modified numerical–analytic method of accelerated convergence [7], we investigate single- and multimode confusor flows in a wide range of the parameters β and $\mathrm{Re} = \dfrac{\rho Q}{\mu}$ [7–9]. The renewed interest in the Jeffery–Hamel problem is stimulated by both increased capabilities of computers and development of software, as well as by practical demands for solving a wider class of problems on the flow of a viscoplastic medium with the low yield point in a plane confusor. For such flows, the Jeffery–Hamel solution is the reference, or zero-order, approximation [4, 9].

The process of deforming an incompressible viscoplastic material with the shear stress point $\omega = \tau_s$ in a confusor is no longer self-similar and radial. For such a material, the determining relationships have the form [4]

$$\underset{\sim}{s} = 2\left(\frac{\tau_s}{U} + \frac{\rho Q}{\mathrm{Re}}\right)\underset{\sim}{v}. \tag{15}$$

Analysis of the units of measure indicates that the four quantities β, Q, ρ, and μ in the two-dimensional case cannot form a combination with the unit of measure of τ_s. On the basis of the procedure described in Sections 1 and 2, one can investigate the confusor flow of a viscoplastic medium with the asymptotically low yield point τ_s by setting $\omega = \tau_s$.

Representing the solution in the form of asymptotic series (3) in terms of the parameter τ,

$$\mathbf{v} = \mathbf{v}^\circ + \sum_{n=1}^{\infty}\tau^n\mathbf{v}^{(n)}, \quad \underset{\sim}{v} = \underset{\sim}{v}^\circ + \sum_{n=1}^{\infty}\tau^n\underset{\sim}{v}^{(n)},$$

$$p = p^\circ + \sum_{n=1}^{\infty}\tau^n p^{(n)}, \tag{16}$$

$$\underset{\sim}{s} = \underset{\sim}{s}^\circ + \sum_{n=1}^{\infty}\tau^n\underset{\sim}{s}^{(n)}, \quad U = U^\circ + \sum_{n=1}^{\infty}\tau^n U^{(n)},$$

we immediately arrive at the expansion [4, 9]

$$U^{(1)} = \frac{2}{U^\circ}\underset{\sim}{v}^\circ\colon\ \underset{\sim}{v}^{(1)}, \quad \frac{1}{U} = \frac{1}{U^\circ}\left(1 - \frac{\tau U^{(1)}}{U^\circ}\right) + O(\tau^2). \tag{17}$$

Now, using expansion (17), we linearize the determining vector relationships (15):

$$\underset{\sim}{s}^\circ + \tau\underset{\sim}{s}^{(1)} + O(\tau^2) = 2\left[\frac{\tau_s}{U^\circ}\left(1 - \frac{\tau U^{(1)}}{U^\circ}\right) + \frac{\rho Q}{\mathrm{Re}}\right](\underset{\sim}{v}^\circ + \tau\underset{\sim}{v}^{(1)}) + O(\tau^2). \tag{18}$$

In accordance with Eqs. (3)–(5), we set

$$\underset{\sim}{s}^\circ = 2\frac{\rho Q}{\mathrm{Re}}\underset{\sim}{v}^\circ, \quad \underset{\sim}{s}^{(1)} = 2\left(\frac{\tau_s}{\tau U^\circ}\underset{\sim}{v}^\circ + \frac{\rho Q}{\mathrm{Re}}\underset{\sim}{v}^{(1)}\right). \tag{19}$$

After the substitution of stress deviator (19) into the two linearized equations of motion, the last two equations along with the incompressibility condition form a closed system of three equations with respect to the pressure $p^{(1)}$ and two components $v_r^{(1)}$ and $v_\theta^{(1)}$ of the vector $\mathbf{v}^{(1)}$ [4, 9]. We seek the solution of this system in the form

$$v_r^{(1)} = -\frac{\tau_s}{\tau\rho Q}\frac{rW'(\theta)}{2}, \quad v_\theta^{(1)} = \frac{\tau_s}{\tau\rho Q}rW(\theta); \tag{20}$$

$$v_{rr}^{(1)} = -v_{\theta\theta}^{(1)} = -\frac{\tau_s}{\tau\rho Q}\frac{W'(\theta)}{2}, \quad v_{r\theta}^{(1)} = -\frac{\tau_s}{\tau\rho Q}\frac{W''(\theta)}{4}. \tag{21}$$

It was established [4] that, in the first approximation in τ, the original boundary-value problem can be reduced to a fourth order equation for a dimensionless function $W(\theta)$

$$\left[-\frac{W'''}{\mathrm{Re}} - \frac{4W'}{\mathrm{Re}} + 2V'W + 4\left(\frac{v_{r\theta}^\circ}{U^\circ}\right)' + 8\frac{v_{rr}^\circ}{U^\circ}\right]' = 0 \tag{22}$$

with the homogeneous boundary conditions

$$W(\pm\beta) = 0, \quad W'(\pm\beta) = 0. \tag{23}$$

In Eq. (22), $V(\theta) = -\dfrac{rv_r^\circ}{Q}$ is the function completely characterizing the Jeffery–Hamel flow.

The problem specified by Eqs. (22) and (23), where the parameter τ is already absent, was investigated numerically and analytically in detail in [8, 9]. We emphasize that the presence of the small asymptotic parameter τ in the denominators in Eqs. (19)–(21) does not mean an apparent singularity of the solution. Actually, substituting expressions (21) into the function $\underset{\sim}{s}^{(1)}$ given by Eq. (19) and, next, Eqs. (19) and (21) into Eqs. (16), we find that the parameter τ is absent in final formulas (16), not only in the denominators, but also in any approximation order n. These formulas represent formal asymptotic expansion (7) of the parameters $\mathbf{v}$, $\underset{\sim}{v}$, p, $\underset{\sim}{s}$, and U in the problem of the viscoplastic flow in terms of the dimensional yield point τ_s.

ACKNOWLEDGMENTS

This work was supported by the Russian Foundation for Basic Research (project nos. 02-01-00252 and 02-01-00780).

REFERENCES

1. N. E. Kochin, I. A. Kibel', and N. V. Roze, *Theoretical Hydromechanics* (Fizmatgiz, Moscow, 1963), Part 2.
2. L. G. Loĭtsyanskiĭ, *Fluid and Gas Mechanics* (Nauka, Moscow, 1987).
3. G. I. Barenblatt, *Similarity, Self-Similarity, and Intermediate Asymptotics* (Gidrometeoizdat, Leningrad, 1982; Consultants Bureau, New York, 1979).
4. D. V. Georgievskiĭ, *Stability of Deformation Processes in Viscoplastic Bodies* (URSS, Moscow, 1998).
5. M. A. Krasnosel'skiĭ, G. M. Vaĭnikko, P. P. Zabreĭko, *et al.*, *Approximate Solution of Operator Equations* (Nauka, Moscow, 1969).
6. A. N. Kolmogorov and S. V. Fomin, *Elements of the Theory of Function and Functional Analyses* (Nauka, Moscow, 1981; Graylock Press, Rochester, N.Y., 1957, Vol. 1 and Graylock Press, Albany, N.Y., 1961, Vol. 2 (transl. of the 1st Russ. ed.).
7. L. D. Akulenko, S. A. Kumakshev, and S. V. Nesterov, Prikl. Mat. Mekh. **66** (5), 723 (2002).
8. L. D. Akulenko, D. V. Georgievskiĭ, and S. A. Kumakshev, Dokl. Akad. Nauk **383**, 46 (2002) [Dokl. Phys. **47**, 219 (2002)].
9. D. M. Klimov, S. V. Nesterov, L. D. Akulenko, *et al.*, Dokl. Akad. Nauk **375**, 37 (2000) [Dokl. Phys. **45**, 601 (2000)].

Translated by Yu. Vishnyakov

Doklady Physics, Vol. 48, No. 6, 2003, pp. 319–322. Translated from Doklady Akademii Nauk, Vol. 390, No. 6, 2003, pp. 769–772.

MECHANICS

An Electrocapillary Eddy Model of Ball Lightning

V. L. Natyaganov

Presented by Academician E.I. Shemyakin November 24, 2002

Received December 5, 2002

In his outstanding study entitled "Table about Air Phenomena Caused by an Electric Force," Mikhail Lomonosov thoroughly analyzed all types of gas discharges known at that time [1]. The surprising fact is that this analysis almost entirely corresponded to the modern classification of these discharges (excluding the arc discharge discovered by Petrov in 1802). In addition, Lomonosov found "…the most general regularities in the process of generation of atmospheric electricity…" [2]. He also announced the discovery (with the help of a Rikhman electrometer) of the Earth's electric field existing even in the case of a clear cloudless sky. Lomonosov was one of the first scientists to suggest a hypothesis on the electric nature of ball lightning, tornados, and aurora borealis. These phenomena were considered by him as the most intricate ones associated with the atmospheric electricity. Only several lines in "Explanation…" were devoted to ball lightning, without directly mentioning its name. It is worth citing these lines here: "Both legends of ancient history and recent news of eyewitnesses testify to the fact that a fire drops onto the ground from thunderstorm clouds. This fire exhibits relatively slow motion compared to usual lightning and, thereby, should be distinguished from it as having a specific nature…."

Up to now, a set of descriptions presented by eyewitnesses that have observed ball lightning were collected in well-known monographs of numerous authors, from Arago to Stakhanov (see, e.g., [3–5]). More than 20 models based on hundreds of various hypotheses were proposed. Many attempts aimed at reproducing ball lightning in laboratory conditions were performed. Despite these facts, this paradoxical natural phenomenon still remains an enigma. In [5], statistical analysis of data related to ball lightning is carried out and a critical review of models, which complements the abovementioned studies [3, 4], is given.

To summarize briefly, ball lightning is an autonomous physical body of approximately spherical shape and with the most probable diameter $2R$ = 10–15 cm (the mean diameter is $2R = 28 \pm 4$ cm). The ball lightning emits visible light and can move in a complicated manner in the environment. In the mature stage, ball lightning exhibits the following basic attributes and contradictory properties.

(1) In the majority of cases, ball lightning emits light without heat. (According to Stakhanov, this is the first paradox.)

(2) The substance of ball lightning probably has the density of air and possesses a surface tension, which is intrinsic to liquids. (Following Stakhanov, this is the second paradox.)

(3) The unpredicted character of ball-lightning motion (up and down, leeward and windward) can be called the third paradox.

(4) Numerous data testify to the fact that ball lightning can have an electric charge. However, the nature of ball lightning (i.e., whether it has a volume charge or a surface charge) is not clear at this point.

(5) It is assumed that the average energy density of ball lightning does not exceed 10 J cm^{-3}. The nature of this energy, as well as the question of whether it is stored initially in ball lightning or comes from the outside, remains open.

In [6, 7], a hypothesis was proposed that ball lightning represents a certain electric-hydrodynamic capacitor of spherical shape with mobile and oppositely charged plates. In its electric structure, this capacitor is similar to a well-conducting Levich droplet [8] residing in an electrolyte solution. In this case, the ball-lightning substance represents a specific phase of atmospheric air subjected to the action of an intense electric field, the role of an external electrolyte being played by ionized air. The theoretical possibility for the existence of strong double electric layers in a gas-flame medium was suggested even by Langmuir in 1929. This possibility was experimentally confirmed in the 80th-anniversary studies of [8], devoted to computer simulation of plasma-physics problems [9] on the basis of the Vlasov equations. However, in this case, the Reynolds numbers inside and outside a ball lightning must not be small, as in the problem of the electrocapillary drift (motion) of a Levich droplet with a thin double electric layer carrying the surface charge.

Moscow State University,
Vorob'evy gory, Moscow, 119899 Russia
e-mail: tenzor@mail.lib.msu.su

1028-3358/03/4806-0319$24.00

We call the electrocapillary eddy structure a gas-flame structure similar to a Levich droplet [8] with a triple electromagnetic layer at the interphase boundary [6, 7]. In this case, we arrive at a rather important statement that can be formulated in the form of the following theorem.

Theorem. *Let ball lightning have an electrocapillary eddy structure and let the densities of the substance outside and inside the ball lightning be equal to each other. If, in this case, the linear Stokes equations in the modified system of equations* (1) *of* [7] *are replaced by the nonlinear Navier–Stokes equations*

$$\begin{aligned} r > 1: \Delta\mathbf{u} &= \Delta p + \mathrm{Re}(\mathbf{u}\cdot\nabla)\mathbf{u}, \\ r < 1: \Delta\mathbf{u}' &= \nabla p' + \mathrm{Re}'(\mathbf{u}'\cdot\nabla)\mathbf{u}' \end{aligned} \quad (1)$$

and if the equality of the jump of normal stresses (*at* $r = 1$) *to the excess pressure is taken into account, this system has an exact solution obtained in* [6, 7] *for the electric potential* φ *and the velocity field* (*the potential flow outside ball lightning and Hill vortex inside it*). *The velocity field is written out in terms of the stream function* Ψ:

$$\begin{aligned} r > 1: \varphi &= \left(-r + \frac{\beta}{r^2}\right)\cos\theta, \quad \Psi = \frac{1}{2}u_e\left(r^2 - \frac{1}{r}\right)\sin^2\theta, \\ r < 1: \varphi' &= -\frac{2qv_0}{\sigma_*}r\cos\theta, \quad \Psi' = \frac{3}{4}u_e r^2(r^2-1)\sin^2\theta. \end{aligned} \quad (2)$$

Corollary. *In the case of such a replacement, the allowance for the term* $(\mathbf{u}\cdot\nabla)\mathbf{u}$ *in the equations of motion results in only redistribution of pressure outside and inside ball lightning without violation of both its spherical shape and flow kinematics.*

The Levich formula in [8] also remains valid for the ball-lightning velocity in the case $\mathrm{Re} \gg 1$:

$$\begin{aligned} U_e = \frac{2}{3}v_0 &= \frac{q}{2 + 3\eta_* + q^2\left(1 + \frac{2}{\sigma_*}\right)} \\ &\longrightarrow \frac{aqE_0}{2\eta + 3\eta' + \frac{q^2}{\sigma}\left(1 + \frac{2}{\sigma_*}\right)}. \end{aligned} \quad (3)$$

This velocity (expressed in dimensional variables) is proportional to the radius a of the ball lightning, to the density q of the surface charge in its double electric layer, and to the intensity E_0 of the local electric field. The electrocapillary drift of ball lightning in the direction of the atmospheric electric field is similar to the thermocapillary drift of a droplet or a bubble, which is explained by the Marangoni effect [10, 11].

It should be emphasized that the validity of the formulated theorem is stipulated by specific features of the solutions obtained for the velocity field inside and outside the ball lightning. This is caused by the fact that both the potential flow and Hill vortex are related to the important class of dynamically reversible flows introduced in [12] by analogy with thermodynamically reversible processes. For this class of flows, nonlinear terms of the $(\mathbf{u}\cdot\nabla)\mathbf{u}$ type have a gradient nature. At the same time, for the potential flow outside the ball lightning, the additional pressure is determined by the Bernoulli integral, whereas the validity of the relation

$$(\mathbf{u}'\cdot\nabla)\mathbf{u}' = \frac{9}{16}u_e^2\nabla[r^2 + (3r^2 - 2r^4)\cos 2\theta], \quad (4)$$

can be proven for the Hill vortex. In the case of equal densities, expression (4) results in equal additions to the pressures outside and inside the ball lightning and does not contradict the conservation of its spherical shape.

Based on the hypothesis of the electrocapillary eddy structure of ball lightning and on the above-formulated theorem, we can explain not only the basic characteristic attributes of ball lightning in the quasisteady stage of its history, which correspond to items (1)–(5), but the wider list of properties presented in [5].

(i) The emission of visible light is one of the most well-known properties of ball lightning, which usually makes possible its observation. As follows from solution (2), in the case of electrocapillary motion of ball lightning, there exists a direct electric current inside it,

$$\mathbf{j}' = -\sigma_*\nabla\varphi' = 2qv_0\mathbf{k},$$

which provides the electroluminescence of the ball-lightning substance. The nature of this electroluminescence is glow discharge or corona discharge [2] that emits visible light without heat.

(ii) The existence of the surface tension γ and its dependence on the electric-potential jump outside and inside the ball lightning, in fact, enter as necessary conditions into the formulation of the above theorem. The equality of the densities $\rho' = \rho$ for both the substance of the ball lightning and the ambient air provides the conservation of the spherical shape even at large velocities of the electrocapillary drift and Reynolds numbers $\mathrm{Re} \gg 1$. The additional stability is provided by the triple electromagnetic layer with mutually orthogonal electric and magnetic fields [6, 7]. In the case of $\rho' \neq \rho$, solution (2) can be considered as the first approximation to the solution of the problem in the general case provided that the Weber number is smaller than 2.

(iii) In the majority of cases, the cause of the electrocapillary drift of ball lightning is the natural atmospheric electric field, previously discovered by Lomonosov [1]. In the case of fine weather, this field attains 12–140 V m^{-1}, whereas under thunderstorm clouds, the electric field is able not only to reverse its direction [2] but also to increase by 2–4 orders of magnitude [5]. In regions of elevated electric field, ball lightning moves at the velocity of the electrocapillary motion, which is described by formula (3), almost independently of the wind direction. In the case of $\rho' \neq \rho$ and at low values of E_0, in addition to the electrocapillary motion and the

wind, it is necessary to allow for the balance of the force of gravity, the buoyancy force, and the force of viscous resistance, which can be made sequentially at $\mathrm{Re} \ll 1$.

For example, as $E_0 \longrightarrow 0$, and in the absence of a wind, ball lightning falls out (emerges) in the ambient air at the velocity

$$V_0 = \frac{2}{3}\frac{\rho a^2}{\eta}\frac{\eta + \eta' + \frac{q^2}{3\sigma}}{2\eta + 3\eta' + \frac{q^2}{\sigma}}(\rho' - \rho). \qquad (5)$$

This result follows from the generalization of the classical Hadamard–Rybchinsky problem for a droplet with the surface charge of a double electric layer [8]. The complementary analysis of the solution to the problem of the magnetohydrodynamic flow around a droplet [13] having a double electric layer was also performed for the case of ball lightning. It was shown that allowance for the external geomagnetic field with the induction $\mathbf{B}_0$, which is directed at an angle α with respect to the force of gravity, leads to three effects: (*a*) a term proportional to the Hartmann number $\mathrm{Ha} = B_0 a\sqrt{\frac{\sigma}{\eta}} \ll 1$ appears in formula (5); (*b*) a force proportional to $\mathrm{Ha}\sin 2\alpha$ acts in the lateral direction in the plane of the vectors $\mathbf{B}_0$ and $\mathbf{V}_0$; and (*c*) in the plane orthogonal to this direction, an induced electrocapillaty drift of the ball lightning arises, which has a velocity given by formula (3) (in this case, it is necessary to replace $\mathbf{E}_0$ by the vector product $[\mathbf{V}_0 \times \mathbf{B}_0]$). Therefore, even at $\mathbf{E}_0 \longrightarrow 0$ in the absence of wind, ball lightning falls out in a complicated manner.

The electrocapillary eddy model of ball lightning makes it possible to explain such strange behavior as the tendency to approach chimneys, which was noted long ago by Arago [2], and phenomena of levitation and guiding [4, 5]. The levitation arises in the case of $\rho' \neq \rho$ and in the presence of a vertical electric field, when the ball lightning hovers in the air. Either wind or the horizontal component of the field can carry away ball lightning residing in such a quasi-zero-gravity state. A similar situation arises when ball lightning is guided along telephone-line conductors or electric-power lines. In these cases, ball lightning gets into an electromagnetic well like the bobsled route.

(iv) The basic point of the hypothesis under discussion on the structure of ball lightning is the existence of a double electric layer ($q \neq 0$). We here emphasize the fact that specific electrokinetic features of the double electric layer allow us to consider the atmospheric electric field as a source of electrocapillary drift of the ball lightning. The existence of ball lightning in itself is possible until the ion concentration in ambient air is sufficiently high for maintaining the quasiequilibrium state on the external plate of the double electric layer. Every motion of the ball-lightning surface (independently of a cause) results in a transformation of the electrostatic double electric layer into an electrodynamic one [6, 7]. This layer not only hampers the diffusion of the vorticity into the environment and thereby promotes conserving the momentum and kinetic energy of the ball lightning as an eddy cluster but also plays an important role in the energy exchange with the environment.

(v) It follows from the electrocapillary eddy model that the atmospheric electric field is not only the source of the mechanical momentum of ball lightning as an entire system but also the energy source. This is confirmed by the immediate calculation of the divergence of the Pointing vector $\mathbf{\Pi} = [\mathbf{E} \times \mathbf{H}]$, which corresponds to the energy flux density of the electromagnetic field [14]. Here, $\mathbf{H}$ is the magnetic self-field of electric currents, which was first obtained in [6, 7].

Inside the ball lightning, $\mathrm{div}\mathbf{\Pi}' = \mathrm{const} < 0$; i.e., the substance of the ball lightning is fed by the electromagnetic energy from the external space. Outside the ball lightning, $\mathrm{div}\mathbf{\Pi}$ has a more complicated character. We can show that $\mathrm{div}\mathbf{\Pi} < 0$ as $r \longrightarrow 1$ and in the case when $-\frac{1}{2} < \beta = qV_0 - \frac{1}{2} \leq \frac{\sqrt{3}-1}{2}$. This implies that ball lightning, together with the double electric layer, is fed by the electromagnetic-field energy across its entire surface independently of the value of the angle θ. However, with the increase in β, in the case when $\frac{\sqrt{3}-1}{2} < \beta < 1$, a zone begins to grow from the ball-lightning equator $\left(\theta = \frac{\pi}{2}\right)$ in which $\mathrm{div}\mathbf{\Pi} > 0$. In this zone, the ball lightning (more precisely, the triple electromagnetic layer) returns energy to the environment. Outside this zone (as $\beta \longrightarrow 1$ $\tan^2\theta < 3$), the energy always comes from the outside into the ball lightning (and to the triple electromagnetic layer).

The initial electrostatic energy of ball lightning as a spherical capacitor (having diameter $2R \sim 20$ cm with the thickness of the double electric layer of about 0.1–1 cm and the voltage difference between the plates up to 30 kV cm^{-1}) does not exceed several units of Joule, i.e., is reasonably low. Events of catastrophic consequences of ball-lightning contacts with other objects can be explained by the appearance of intense (up to 10 A) electric-current pulses. Explosion of ball lightning in the case of thunderstorm weather serves as a trigger mechanism [5] causing the scattering of electric charges induced on these objects.

ACKNOWLEDGMENTS

This work was supported by the Russian Foundation for Basic Research, project no. 01-01-00010.

REFERENCES

1. M. V. Lomonosov, *Tale about Air Phenomena Caused by an Electric Force* (Akad. Nauk SSSR, Moscow, 1952), Vol. 3, pp. 15–99.
2. Ya. I. Frenkel', *Theory of Atmospheric Electricity Phenomena* (GITTL, Moscow, 1949).
3. R. A. Leonov, *Ball Lightning Mystery* (Nauka, Moscow, 1965).
4. S. Singer, *Nature of Ball Lightning* (Plenum, New York, 1971; Mir, Moscow, 1973).
5. I. P. Stakhanov, *About Physical Nature of Ball Lightning* (Nauchnyĭ Mir, Moscow, 1996).
6. V. L. Natyaganov, in *Mathematics, Computer, Education* (Progress-Traditsiya, Moscow, 2001), No. 8.4.2, pp. 366–370.
7. V. L. Natyaganov, Dokl. Akad. Nauk **381**, 50 (2001) [Dokl. Phys. **46**, 800 (2001)].
8. V. G. Levich, *Physicochemical Hydrodynamics* (Fizmatgiz, Moscow, 1959).
9. Yu. S. Sigov, *Calculation Experiment: Bridge between Past and Future of Plasma Physics. Selected Papers* (Fizmatlit, Moscow, 2001).
10. G. Birkhoff, *Hydrodynamics* (Princeton Univ., Princeton, 1960; Inostrannaya Literatura, Moscow, 1963).
11. A. M. Kutepov, A. D. Polyanin, *et al.*, *Chemical Hydrodynamics* (Byuro-Kvantum, Moscow, 1996).
12. K. Yajnik, J. Basic Eng. **89** (1), 237 (1967).
13. A. M. Golovin and V. L. Natyaganov, Izv. Akad. Nauk SSSR, Mekh. Zhidk. Gaza, No. 6, 19 (1978).
14. I. E. Tamm, *Principles of Electricity Theory* (Nauka, Moscow, 1966).

Translated by G. Merzon

Doklady Physics, Vol. 48, No. 6, 2003, p. 323.

ERRATA

Erratum: "Hydrodynamic Mechanism of Bleaching a Strongly Absorbing Liquid by a Laser Pulse" [*Doklady Physics* 48 (2), 90 (2003); *Doklady Akademii Nauk* 388, 5 (2003)]

A. N. Kucherov

In my paper "Hydrodynamic Mechanism of Bleaching a Strongly Absorbing Liquid by a Laser Pulse," formula (2) should be read as

$$T_{\text{trans}} = \int_0^\infty \int_0^\infty f\left(\frac{t}{\tau}\right) \exp\left[-\frac{\alpha\rho(r,t)\Delta z}{\rho_0} - \left(\frac{r}{r_0}\right)^2\right] \frac{2r\,dr}{r_0^2} \frac{dt}{\tau}. \quad (2)$$

Translated by G. Merzon

1028-3358/03/4806-0323$24.00 © 2003 MAIK "Nauka/Interperiodica"